Electrokinetic trapping of single molecules, and Euler buckling and nonlinear kinking of DNA

A dissertation presented

by

Alexander Preston Fields

to

The Committee on Higher Degrees in Biophysics

in partial fulfillment of the requirements

for the degree of

Doctor of Philosophy

in the subject of

Biophysics

Harvard University

Cambridge, Massachusetts

May 2013

Dissertation Advisor: Professor Adam E. Cohen   Alexander Preston Fields

Electrokinetic trapping of single molecules, and Euler buckling and nonlinear kinking of DNA

Abstract

I present two applications of fluorescence spectroscopy in biophysics. The first is an instrument, the anti-Brownian electrokinetic (ABEL) trap, which is capable of trapping individual small molecules in aqueous solution at room temperature. The second is an investigation of the bending mechanics of double-stranded DNA using a novel DNA structure called a "molecular vise". Both projects take advantage of the sensitivity and specificity of fluorescence spectroscopy, and both benefit from the interplay of experimental work with theoretical and computational modeling.

The ABEL trap uses fluorescence microscopy to track a freely diffusing particle, and applies real-time electrokinetic feedback forces to oppose observed motion. Small molecules are difficult to trap because they diffuse quickly and because their fluorescence emission is typically weak. I describe the experimental and algorithmic approaches that enabled small-molecule fluorophores to be trapped at room temperature. I additionally derive and discuss the theory of the molecules' behavior in the trap; this mathematical work informed the design of the trapping algorithm and additionally enabled trapped molecules to be distinguished on the basis of their diffusion coefficient and electrokinetic mobility.

Molecular vises are DNA hairpins that use the free energy of hybridization to exert a compressive force on a sub-persistence length segment of double-stranded

DNA. In response to the applied force, this "target strand" may either remain straight or bend, depending on its flexibility and length. Experimentally, the conformation can be monitored via Förster resonance energy transfer (FRET) between appended fluorophores. The experimental results quantitatively matched the predictions of the classic wormlike chain (WLC) model of DNA elasticity at low-to-moderate salt concentrations. Higher ionic strength induced an apparent softening of the DNA which was best accounted for by a high-curvature "kinked" state. The molecular vise is exquisitely sensitive to the sequence-dependent linear and nonlinear elastic properties of dsDNA and provides a platform for studying the effects of chemical modifications and small-molecule or protein binding on these properties.

Table of Contents

Table of Figures

Citations to Previously Published Work

Chapter 1 is adapted from [1]:

Fields AP, Cohen AE (2010) Anti-Brownian traps for studies on single molecules. *Meth Enzymol* 475:149-174.

Chapter 2 is adapted from [2]:

Fields AP, Cohen AE (2012) Optimal tracking of a Brownian particle. *Opt Express* 20:22585-22601.

Chapter 3 is adapted from [3]:

Fields AP, Cohen AE (2011) Electrokinetic trapping at the one nanometer limit. *Proc Natl Acad Sci USA* 108:8937-8942.

Chapter 4 is adapted from [4]:

Cohen AE, Fields AP (2011) The cat that caught the canary: what to do with single-molecule trapping. *ACS Nano* 5:5296-5299.

Chapter 6 is adapted from a manuscript currently in submission:

Fields AP, Meyer EA, Cohen AE (2013) Euler buckling and nonlinear kinking of double-stranded DNA. *In submission*.

Acknowledgments

I have been privileged to receive support and guidance from numerous individuals throughout my time at Harvard. I'm grateful to my advisor, Adam Cohen, for sharing so much of his time and energy. I have benefitted immeasurably from Adam's unwavering dedication, inspirational mentorship, and fearless creativity. Through daily interactions, Adam taught me many of my most valuable lessons from graduate school: how to brainstorm and evaluate ideas, how to prioritize among competing objectives, how to overcome the obstacles inherent to scientific research, and how to recognize and pursue a promising result, to name a few. Participating in the inception and growth of a new research lab has been a profound and educational experience, and I thank Adam for granting me that opportunity.

The Cohen lab has been a pleasant and collaborative environment thanks to the many smart and helpful colleagues who have populated it. I was fortunate to work closely with three talented postdocs, Halil Bayraktar, Joel Kralj, and Sabrina Leslie, on projects not included in this dissertation. Elisabeth Meyer, a Harvard College undergraduate, was a dedicated assistant who contributed greatly to the work described in Chapter 6. Fellow graduate student Min Ju Shon has been an excellent source of advice and experimental assistance. I would also like to thank my other lab mates, past and present, for the many conversations and experiences we shared over the years: Yiqiao Tang, Jennifer Hou, Nan Yang, Prashant Jain, Daniel Hochbaum, Hohjai Lee, Dougal Maclaurin, Veena Venkatachalam, Lucy Rosenbaum, Tony Shen, Jeehae

Park, Daan Brinks, Kit Werley, Dian Yang, and Peng Zou. I also thank rotation students Kevin Axelrod and James Kath for their contributions.

I thank Professors Sunney Xie, Sharad Ramanathan, and Andrew Murray for their time and helpful comments as members of my dissertation advisory committee. I also thank Professor John Bechhoefer of Simon Fraser University for many stimulating discussions during his time at Harvard.

The Harvard biophysics program is a friendly and supportive place due in large part to the tireless efforts of its chair, Professor Jim Hogle, and its administrator, Michele Jakoulov. The retreats and other activities they organized were among the highlights of my time in graduate school.

Life at Harvard is more than just research, and I am thankful to the many friends who enriched my time here. I am particularly indebted to a few of them. Brendan Lehnert and Ben Stanzl have provided me with friendship and camaraderie for over a decade. Fellow biophysicist Graham Dempsey has been a close companion, colleague, and confidant since we began graduate school together, and I've greatly enjoyed the countless experiences we've shared. Andy Leifer has been another great friend in the program and a continuing source of insight, perspective, and laughter.

I am grateful for the support of my parents, Alice Preston and Ken Fields, and my sister, Betsy. My family encouraged and assisted my academic pursuits from an early age, and I love them dearly.

To Nadia, you are my inspiration and I love you.

Part I

Electrokinetic trapping

1
Introduction

Until recently, Brownian motion was seen as an immutable feature of small particles in room-temperature liquids. Molecules, viruses, organelles, and small cells jiggle incessantly due to countless collisions with thermally agitated molecules of solvent. Einstein showed in 1905 that this motion is intimately linked to the tendency of every system to relax toward thermal equilibrium [5].

In recent years, we and others have realized that Brownian motion is not as inescapable as one might think. By tracking the motion of a small particle and applying correction forces to the particle or to the measurement apparatus, one can largely suppress the Brownian motion of particles as small as individual organic fluorophores, in aqueous solution at room temperature (see Chapter 3 and [3, 6]). This new ability to stabilize single molecules has led to a host of studies on topics ranging from the conformational dynamics of DNA [7, 8] to the optical properties of metal nanoparticles [9].

1.1   Theoretical overview

1.1.1   Single-molecule spectroscopy yields important dynamical information but is hampered by Brownian motion

Single-molecule spectroscopy allows one to observe the inner workings of complex molecules, in a way that is not possible from bulk, ensemble-averaged

measurements. Such studies provide information on the dynamics of nucleic acids [10, 11] and proteins [12, 13], both *in vitro* and *in vivo* [14, 15]. The chief difficulty in many single-molecule experiments is that the molecules do not hold still. For small particles this jiggling is so intense that, unless countermeasures are taken, the molecule is seen for only a fleeting moment. One can increase the diffusion-limited observation time by collecting photons from a larger volume, but such a strategy lowers the signal-to-background ratio.

Typical countermeasures against Brownian motion include immobilization on a surface [16], in the pores of a gel [17, 18], inside of a tethered lipid vesicle [19, 20], in a liquid droplet [21], or in enclosed nanofabricated wells [22]. In many cases, there remains a persistent doubt whether the immobilized molecule behaves the same as its comrades in free solution. Additionally, physical restriction of motion prevents the measurement of dynamic properties such as the diffusion coefficient of the trapped molecule. Finally, some designs restrict the volume of solution accessible to the immobilized molecule, so that the pool of available substrates or other interaction partners may be quickly exhausted.

Freely diffusing molecules can be studied via fluctuation spectroscopies such as fluorescence correlation spectroscopy (FCS) [23] or single-molecule burst analysis [24], but these techniques have typical observation times of 1 ms per molecule or less. Short observation times lead to two problems: few photons are collected from each molecule, so measurements of spectroscopic parameters are imprecise, and processes that last longer than the observation time are not resolved. Many biological processes occur on

the timescale of seconds to hours. As a concrete example of the problem facing single-molecule researchers, nobody has found a way to observe directly the catalytic cycle of the chaperonin GroEL, which takes 7–15 seconds, without disturbing this cycle [25].

Laser tweezers have led to a revolution in the fields of nanomanipulation and biophysics by allowing researchers to exert controlled forces on proteins bound to DNA or cytoskeletal elements [26]. Although less widespread, magnetic tweezers [27] and AC dielectrophoresis [28] have also been used to trap and manipulate micron-scale objects. Unfortunately, the forces generated by all of these techniques are too weak to trap objects smaller than ~100 nm in solution at room temperature, except under exceptional circumstances of resonant enhancement [29].

Optical trapping, dielectrophoresis, and magnetic tweezers exert very weak forces for two reasons. First, the force is proportional to the object's polarizability (electric or magnetic), which is proportional to the volume. So to trap a 10 nm object requires a million times as much input power as to trap a 1 micron object. Second, the force arises through a second-order interaction with the applied electric or magnetic field. That is, the field must first polarize the object, and then interact a second time to generate a force between the induced dipole and a gradient in the field. Electrophoretic forces, on the other hand, are much stronger than optical forces. Electrophoresis depends on charge rather than polarizability, and is first order in the field strength, rather than second order. This is why electrophoresis is commonly used to separate biomolecules, and optical forces are not. Electrophoresis is not typically used to trap biomolecules because an electrophoretic potential contains no minima away from the

4

boundaries (although for particles whose momentum is significant, an AC electric field can dynamically trap a charged particle [30]).

Feedback control is widely used to stabilize the motion of stochastic systems, where the stochasticity may arise from quantum, thermal, or manufacturing fluctuations. In particular, feedback may be used to cancel the Brownian motion of a single nanoscale object in solution, over some finite bandwidth. In contrast to passive trapping schemes, feedback trapping potentials need not have any local minima.

The performance of feedback traps scales more favorably for small particles than does that of laser tweezers. To trap objects smaller than 100 nm in diameter, laser tweezers require many watts of infrared light. This intense light runs the risk of cooking an object rather than trapping it. Feedback traps, in contrast, can hold objects as small as 15 nm in diameter with < 1 mW of laser power, used solely for imaging the position of the object.

1.1.2 Basics of Brownian motion

Here we review the basic features of Brownian motion in a force field. A more detailed discussion can be found in [31] and in Chapter 2. If a Brownian particle is released at rest at the origin at $t = 0$ and is free to diffuse in one dimension, the probability of finding the particle at position x at time t is

$$P(x,t) = \frac{e^{-\frac{|x-vt|^2}{4Dt}}}{\sqrt{4\pi Dt}} \tag{1.1}$$

where D is the diffusion coefficient of the particle and v is its average drift velocity due to external forces. In two dimensions the motion along the two axes is statistically

independent, so that the probability can be factored as $P(x, y, t) = P(x, t)P(y, t)$, and similarly in three dimensions. Equation (1.1) describes a Gaussian distribution with average position $\langle x \rangle = vt$, and with variance $\langle x^2 \rangle - \langle x \rangle^2 = 2Dt$. It is often more convenient to work just with the mean and variance, rather than the full probability distribution of Equation (1.1).

The diffusion coefficient of a small particle is given by the Stokes-Einstein relation

$$D = \frac{k_B T}{6 \pi \eta a} \tag{1.2}$$

where k_B is Boltzmann's constant, T is the absolute temperature, η is the viscosity of the medium, and a is the hydrodynamic radius of the particle. The viscosity of pure water at room temperature is ~1 cP, or 10^{-3} kg/m s in SI units. Equation (1.2) implies that smaller particles diffuse faster. A decrease in the size of a particle can be partially compensated by an increase in the viscosity of the medium, but many biomolecules cease to function if the medium differs too much from the cellular milieu.

1.1.3 Basics of tracking and feedback

Anti-Brownian traps use microscopy to track the position of a molecule, and apply feedback forces to keep the molecule close to a target location (Figure 1-1). Here we review the general principles of any Anti-Brownian trap. In Section 1.2 we discuss specific implementations.
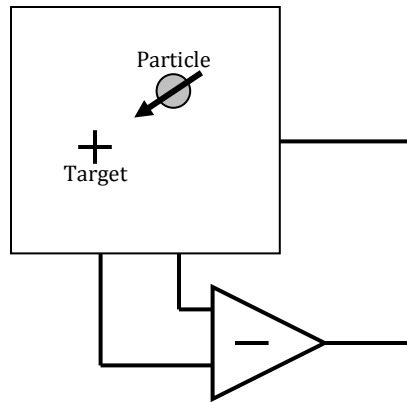
Figure 1-1 General scheme of any anti-Brownian motion trap.

How tightly can an Anti-Brownian trap confine a particle? Several factors combine to limit the degree of confinement. These include: latency of the feedback loop, photophysics of the fluorophore, accuracy of the tracking, and strength of the restoring force.

Between iterations of the feedback, a molecule may wander a distance away from the target location. The displacement along each axis has RMS value $\delta x = \sqrt{2D\tau}$, where D is the diffusion coefficient of the particle and τ is the latency of the feedback. If this distance is comparable to the dimension of the observation volume, a large thermal fluctuation may knock the particle completely out of the trap. Thus one wants to minimize the latency of the feedback, and this requirement becomes more stringent for smaller particles. Our current ABEL trap has feedback latency as small as 10 μs.

Even with perfect feedback hardware, the feedback latency is limited by the finite rate at which photons reach the detector. Between photon detection events there is no information on the location of the particle, and thus no feedback. A fluorophore emitting photons that are detected at rate γ has a minimum average latency of γ^{-1}. The

average value of γ may be as high as 50,000/s, but many fluorophores have a tendency to blink. If a molecule is labeled with a single fluorophore, then the molecule may diffuse a considerable distance during an "off" event, and may even be lost from the trap. Thus, for single-fluorophore experiments it is important to use fluorophores with short triplet state lifetimes. Finally, most fluorophores photobleach, allowing the darkened particle to exit the trap.

The feedback must be accurate as well as fast. A single photon carries incomplete information about the location of a particle. Diffraction causes the photons coming from a single stationary molecule to appear to come from a blob whose shape is given by the point spread function of the microscope. Furthermore, background photons may originate from anywhere within the observation volume, leading to additional spurious information on the location of the molecule. Careful optical design and sample preparation may minimize the number of background photons, but the tracking uncertainty due to diffraction is much harder to eliminate.

One may decrease the uncertainty due to diffraction by averaging over many photons. If each photon is selected from a distribution of width w, then by averaging N photons one may localize a particle with accuracy $w/\sqrt{N}$. This fact is widely used to localize single fluorophores with sub-diffraction accuracy. If photons are detected at rate γ, then $\delta x = w/\sqrt{\gamma t}$ for a stationary particle.

For the case of freely diffusing particles, one cannot average indefinitely because the particle is a moving target. The increase in uncertainty due to diffusion eventually outweighs the decrease in uncertainty due to signal-averaging. The optimal integration

time occurs when the uncertainties due to diffraction ($w/\sqrt{\gamma t}$) and diffusion ($\sqrt{2D\tau}$) are equal (Figure 1-2). This balance yields

$$t_{opt} = \frac{w}{\sqrt{2D\gamma}}.$$ (1.3)

Equation (1.3) is an important result for any particle-tracking system, not just an Anti-Brownian trap. For instance, Equation (1.3) gives an optimal frame-rate for video tracking of particles diffusing in solution or in a cell. Equation (1.3) can also be derived in a more rigorous manner using Bayesian statistics (see Chapter 2).
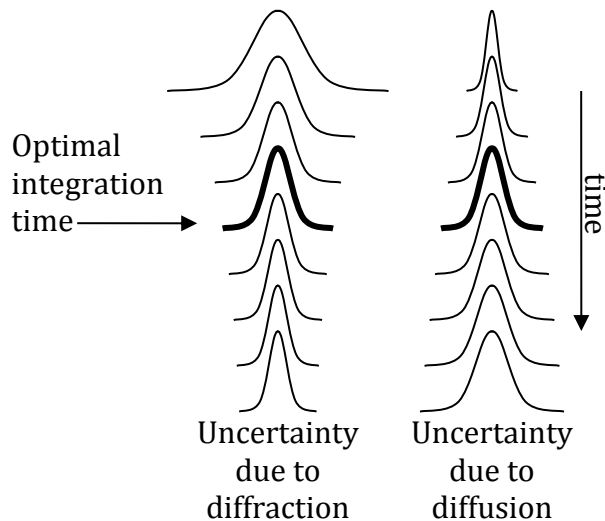
Figure 1-2 Balance of diffusion and diffraction in localization accuracy.

Any feedback system has a maximum velocity with which it can move the particle or the imaging system. This v_{max} may also limit the confinement of the molecule. The RMS velocity of a molecule diffusing a distance d is $v = 2D/d$, so the minimum trap confinement along each axis is $\delta x \geq 2D/v_{max}$. For electrokinetic feedback, v_{max} is relatively independent of the size or nature of the particle, and in microfluidic geometries is $v_{max} \sim 10$ mm/s [35]. Table 1:1 shows that for most objects

one might like to trap, the velocity required to confine the object to an area 500 nm in diameter is much less than 10 mm/s.

Table 1:1 Feedback parameters for commonly encountered substances.

Object	D (μm^2/s)	Bandwidth (Hz)	Velocity (μm/s)
1 μm sphere	0.44	3.5	1.8
200 nm sphere	2.2	18	8.8
20 nm sphere	21.8	174	88
2 nm sphere	218	1740	870
Rhodamine 6G	280	2240	1120
Water [32]	2850	23000	11000
Macromolecules			
Ribosome 4S (*E. coli*) [33]	37	300	150
γ-Globulin [33]	37	300	150
BSA [23]	49	400	200
Hemoglobin [33]	69	550	275
Myoglobin [33]	100	800	400
Lysozyme [34]	111	890	445
Ribonuclease [33]	131	1050	525

Notes: Tyn and Gusek [33] provide an expanded table with diffusion coefficients for 89 macro-molecules and viruses. D is the diffusion coefficient. The feedback bandwidth required for successful trapping within $\delta x = 500$ nm is calculated from $1/t_r = 2D/\delta x^2$. To counter the Brownian motion, the trap must impose a velocity with RMS value $v = 2D/\delta x$.

1.2   Overview of Anti-Brownian trapping systems

Anti-Brownian traps are capable of trapping objects smaller than can be trapped by any other means under comparable conditions. They provide a way to study individual molecules in their native environment, bypassing the perils of surface attachment chemistry. The record of feedback forces also provides information along a dimension not usually accessible to single molecule experiments. By analyzing the feedback forces one can extract time-dependent information about the diffusion coefficient and electrokinetic mobility of the trapped object (see Chapter 2).

Feedback traps consist of two sub-systems: a tracking component and a feedback component. In each case there are multiple options available, with different relative merits. We describe strategies used in our group and others to accomplish these goals. Some of these designs are also reviewed in [36]. Table 1:2 summarizes the combinations of tracking and feedback systems described thus far in the literature, and lists the maximum diffusion constant of the particles trapped in each.

Table 1:2 Anti-Brownian systems in the literature, and their performance specifications.

Tracking Scheme		Feedback Scheme		
	Bandwidth (kHz)	**Laser Translation**	**Stage Translation**	**Electro-kinetic**
Camera	< 0.3	2.4 (3D) [37][a]	< 0.2 (3D) [38][b]	20 (2D) [39, 40]
Multiple photodiodes	fast		0.85 (3D) [41] 6 (3D) [42]	
Scanning Galvo	< 20	0.6 (3D) [43]	6.2 (2D) [44]	
Scanning AOD	< 50		20 (3D) [45]	30 (2D) [46]
Scanning EOD	< 1000			118 (2D) [6] 325 (2D) [3]
Multiple laser foci	< 75,000			In progress [47]

Notes: All tracking systems except for photodiodes operate on a discrete clock, with maximum bandwidth given. Photodiodes operate quasi-continuously and rarely limit the feedback bandwidth. The numbers in the right half of the table indicate the maximum diffusion coefficient that has been trapped (in $\mu m^2/s$), and the number in parentheses is the number of dimensions of the trapping.
[a] This study achieved frame rates up to 3.2 kHz by restricting the imaging to a sub-region of the camera frame.
[b] No diffusion constant is listed in this reference. The particles trapped have 1.1 μm diameter, giving an estimate of 0.2 $\mu m^2/s$ in pure water, but the viscosity of the organic solvent used is unknown.

1.2.1 Tracking systems

Fast tracking of molecules in solution requires an optical readout with high signal-to-background ratio. Here, we consider some ways to track the position of molecules, and list some of their advantages and disadvantages.

11

1.2.1.1 Camera

Perhaps the most obvious way to determine the position of an object is to take a picture of it. The optimal camera for low-light tracking is a frame-transfer electron-multiplying (EM) charge-coupled device (CCD). Frame-transfer mode enables the camera to function at very high frame rate, shortening the latency between emission of a photon and application of corresponding feedback, but also decreasing the number of photons per frame. High EM gain amplifies the signal due to photons above the electronic noise in the camera, improving the signal-to-noise ratio. However, the EM gain amplifies the signal from all photons equally—it does not distinguish between signal photons, originating from the molecule, and background photons originating elsewhere in the optical system. Camera-based imaging is compatible with wide field, total internal reflection (TIR), or scanned illumination, and was used in the original ABEL trap [39, 48]. A fast image-fitting algorithm is necessary to convert each picture into a position estimate, without contributing excessively to the feedback latency. Details on one such algorithm are included in [49]. Cameras can achieve 3D tracking by imaging multiple focal planes [37].

The primary drawback of camera tracking is its low speed. Even in frame transfer mode, EMCCD cameras typically cannot achieve a frame rate above ~1 kHz. Even assuming instantaneous image fitting, feedback latency is at least one millisecond. Such a system has been used to trap particles with diameters of 20 nm in aqueous solution, but smaller objects require higher viscosity or faster detection. Faster frame rates can be achieved by restricting the image to a smaller region of the full area, up to values of

3.2 kHz [37], and new, sensitive scientific complementary metal oxide semiconductor (CMOS) cameras allow even faster frame rates, meaning that feedback latency will be dominated by image processing time.

One advantage of cameras is the generation of direct images of trapped particles, which can be useful when multiple objects are being observed or when the trapped object has significant internal structure [7, 8]. For example, [38] captured 3D image stacks at a frame time of 6 seconds to track diffusion of multiple colloidal particles over a period of several hours, using a spinning-disk confocal microscope. A large imaging area is also useful for applications requiring the trapped particle to be steered across a stationary region or device [50, 51, 52]. Some of these advantages can be maintained without sacrificing feedback latency through hybrid schemes in which a camera collects images while a separate, faster optical system is used to track the object [53].

1.2.1.2 Multi-photodiode

Quadrant photodiodes retain some of the positional information provided by a camera but offer significantly improved bandwidth (often several megahertz). Such a detector can be substituted for a CCD camera in a wide-field imaging setup, and has been used for tracking [9]. Unfortunately, commercially available quadrant photodiodes lack sensitivity and so are poorly suited to detection of dim objects. The optical detector with the best response properties for fast tracking of dim objects is the single-photon-sensitive avalanche photodiode (APD). When operating in Geiger mode, an APD generates a voltage pulse every time a photon is detected and provides unmatched

sensitivity and time resolution. Photomultiplier tubes (PMTs) are also capable of low-light detection, but have lower quantum efficiency.

Several designs use multiple PMTs or APDs to track position. In 1971, Howard Berg used six PMTs to track a swimming bacterium [54]. He coupled the input of each PMT to a fiber, and back-imaged the fiber inputs to the corners of an octahedron at the sample. The group of Haw Yang employs two prism mirrors reflecting light onto four APDs, two each for the x- and y-axes [55]. 3D tracking is achieved using a defocused confocal pinhole so that the light intensity on a fifth APD is modulated in response to axial motion of the tracked particle. Unfortunately, this design is susceptible to low-frequency drifts in illumination intensity and to fluctuations in the brightness of the trapped particle, which would be interpreted as changes in axial position. The Werner group stays closest to Berg's original design, back-imaging the photoreceptive areas of four APDs to the corners of a tetrahedron at the sample plane [41, 56]. Such a design loses signal due to the splitting of the light prior to the confocal spatial filtering and due to the dead area between the confocal pinholes (i.e., the cladding of the optical fibers). In each of these designs, the position estimate is constructed using either analog electronics or a field-programmable gate array (FPGA) to scale and subtract the appropriate signals. The FPGA-based algorithm we describe in Section 1.3.3 could be adapted to fit a detection scheme of this style.

1.2.1.3 Scanning

An alternative way to detect position is to use a scanned laser beam and a single APD, as first proposed by Jörg Enderlein [57]. A confocal spot is rapidly rotated in a

circle, with the radius of the circle approximately equal to the radius of the spot. If the molecule is in the center of the circle, the molecule emits a steady flux of fluorescent photons. If the molecule moves off-center, there is a modulation in the fluorescence intensity at the laser rotation frequency. The phase of this modulation, relative to the phase of the laser rotation, indicates the direction in which the molecule has moved. Enderlein's original proposal only tracks two-dimensional diffusion, as he intended it for slowly diffusing molecules confined to two dimensions by cellular membranes ($D < 10^{-2}$ μm^2/s).

Scanning of excitation light through the sample can be achieved using galvanometer scanners (galvos), acousto-optic beam deflectors (AODs), or electro-optic beam deflectors (EODs). The most important characteristic of these scanners for the purpose of fast tracking is their modulation bandwidth as this sets the maximum bandwidth of the feedback. Typical maximum scan rates are 20 kHz, 50 kHz, and 250 kHz for galvos, AODs, and EODs, respectively. The limited bandwidth of the galvos makes them less suitable than AODs or EODs. EODs offer improved stability [58] and lower wavelength dependence than AODs, but require high-voltage drive electronics. Either AODs or EODs offer sufficient scan speeds for fast tracking.

A simple way to calculate the phase of the fluorescence intensity modulation (and thus the position estimate) is to use a commercially available vector lock-in amplifier, with the photon signal as the input and the scanning signal as reference. The x and y output channels provide a direct readout of the position of the particle, provided the internal phase offset is calibrated correctly. Equation (1.3) specifies the optimal

integration time for the lock-in, based on the diffusion constant and average count rate of the particle. Lock-in amplifiers often come with a minimum latency, which may inhibit trapping of smaller particles. Analog hardware circuits, such as the one described in [46], can shorten this delay, but are difficult to tune. The tracking scheme we outline in Section 1.3.3 for implementation on an FPGA allows near-optimal estimation while retaining flexibility.

The first implementation of scanning-based tracking is due to the group of Enrico Gratton, who used galvos to scan in 2D and a z-nanopositioner to move the objective between two focal planes for 3D tracking [43, 59]. Around the same time, Andrew Berglund and Hideo Mabuchi designed a 2D scanning trap, also using galvo scanners [44, 60]. The Mabuchi group has since made numerous improvements to their trap [61, 62]; their most recently published designs employ three AODs to vary laser light intensity sinusoidally between two focal planes in addition to the rotation within each plane, enabling fully three-dimensional sensitivity [45], and include orthogonal illumination and detection optics to probe the tracked particle [63, 64]. A hardware ABEL trap that tracks position by scanning a laser using an AOD has also been constructed [46, 65].

1.2.1.4 Multi-focus

A clever alternative to direct scanning of a laser beam is to split pulsed excitation light into multiple beams that illuminate discrete points at the sample [47]. By adjusting the distances traveled by each beam prior to hitting the sample, the illumination of each point can be separated in time. When a photon is detected, it is assigned with high probability to the position currently illuminated. The arrival-time information is

obtained using multi-channel gated detection. The resulting series of photon position measurements can then be used to estimate particle position using the scheme described in Section 1.3.3. Laser pulse frequencies are typically very high (~75 MHz), meaning that the system bandwidth is more likely to be limited by electronics and photon intensity than by the scanning itself. One concern with such a high scan rate is cross-talk due to the delay of the fluorescence excited state lifetime; this problem could be alleviated by using a pulse picker to lower the pulse frequency. Another concern is that tuning a multi-focused illumination system (e.g., to change the number or position of scanned points) is more difficult than it is for the scanning systems described above.

1.2.2 Feedback systems

In addition to an optical system capable of tracking the motion of a particle in solution, a usable trap requires a feedback system to adjust the position of the particle relative to the tracking optics. Several strategies have been proposed and implemented.

1.2.2.1 Laser tracking

In Enderlein's original proposal for scanning laser tracking, the molecule is allowed to diffuse freely, and the center of the laser focus is adjusted to follow the molecule [57]. Gratton and coworkers implemented this strategy for x-y repositioning, and translated the objective directly using a nanopositioner along the z-axis [43]. The problem with moving the laser to follow the position of a tracked particle is that both the scanning optics and the detection optics have limited range, and the spot will eventually fall off the edge of one of them. The Gratton group's design was aided in this regard by their use of galvos for scanning and a PMT for detection; AODs and EODs have

17

much smaller maximum scan angles than galvos, and APDs have smaller photoreceptive areas than PMTs. A similar system was constructed by Juette and Bewersdorf [37].

1.2.2.2 Stage feedback

Howard Berg's original tracking microscope translated the sample to keep bacteria within the field-of-view [54]. This mechanism neatly avoids the issue of limited detector field-of-view. Beginning with the Mabuchi lab, several groups have adapted stage feedback to single-particle tracking [9, 38, 56, 60]. Most mechanical translation stages are too slow to track very fast objects, and the finite travel of the stage limits the amount of time an object can be tracked. Additionally, tracking systems are easily confused by fixed pieces of dirt on a coverslip. As the system follows a particle diffusing over a surface, it is likely to encounter other particles stuck to the surface. Quite frequently the tracking system locks onto one of these fixed objects and loses the moving object of interest.

1.2.2.3 Electrokinetic feedback

Anti-Brownian Electrokinetic traps (ABEL traps) use electric fields to impose a drift on a particle that counteracts the Brownian motion. Two distinct electrokinetic effects are at play in an ABEL trap, called *electrophoresis* and *electroosmosis*. Electrophoretic forces arise from direct action of an applied electric field on the charge of a particle. Naturally these forces apply only to charged particles.

To our surprise, we found that even nominally neutral particles move in an ABEL trap. The origin of this motion is the electroosmotic effect. When water is confined in a thin channel, the walls of the channel typically develop a charge due to preferential

18

adsorption or desorption of ions of one charge. This fixed charge is screened by mobile charges of opposite sign within a nanometers-thick "Debye layer". An applied electric field exerts a force on these dissolved ions, and these ions exert a force on the water, leading to a net flow. This electroosmotic flow generates a hydrodynamic force which carries neutral particles at the same velocity as the flow. By tailoring the surface charge of the channel, it is possible to augment or eliminate this electroosmotic flow. Thus, an ABEL trap can confine charged or neutral particles.

The applied electric field for trapping is only a weak perturbation to the molecule. Within a channel < 10 μm thick, a field of several hundred V/cm is sufficient to generate a large enough electroosmotic flow to cancel Brownian motion of most molecules. In contrast, an electric field > 25,000 V/cm would be needed to impart a potential difference of order $k_B T$ to charges in a molecule of size < 10 nm.

The electrokinetic feedback applied in an ABEL trap overcomes many of the limitations of stage translation. Electrokinetic forces can move a particle far more quickly than can a piezo stage [39]. The tracking system is not thrown off by stuck dirt if there is none present at the start of the experiment, because the trapping is performed at a fixed position in the sample cell. An ABEL trap also allows one to position a trapped object relative to other fixed objects on the surface. On the other hand, it would be difficult or impossible to employ electrokinetic feedback to track particles inside cells or in other heterogeneous environments, while stage feedback performs this task with ease.

In addition to our own ABEL traps and ongoing efforts in the Moerner lab [3, 6, 39, 46, 49, 65, 66, 67, 68, 69, 70, 71], Ben Shapiro's group has employed video tracking and an array of microelectrodes to steer multiple particles (e.g., yeast cells 4 μm in diameter) in solution [48, 72]. The Shapiro lab has also constructed ABEL trap-like devices for precise positioning of quantum dots [50, 51, 52]. The group of Lloyd Davis has described designs for both one- and three-dimensional ABEL traps, and has described a novel sample holder for the former geometry [47, 73].

1.3 The ABEL trap

Here we show in detail how the elements discussed above can be combined in a high-performance ABEL trap for trapping single molecules. The system described here has been constructed in our lab and, to our knowledge, traps smaller particles in solution than any comparable system.

The heart of our ABEL trap is a microfluidic cell which confines molecules to a thin pancake-shaped trapping region < 1 μm thick and ~10 μm wide. Feedback electric fields are applied to four electrodes, which are connected to the corners of the trapping region. The microfluidic cell is mounted in a fluorescence microscope, and an automated tracking and feedback system applies voltages to the electrodes to suppress the Brownian motion of a single particle.

In the early incarnations of our trap, we used a video camera and real-time image processing on a personal computer to follow the Brownian motion [40, 49, 66, 67]. Representative results obtained with this trap are shown in Figure 1-3. This

feedback system had a minimum latency of 4.5 ms, determined largely by the frame-rate of the camera. We subsequently switched to a hardware feedback scheme, in which the particle was illuminated with a rapidly rotating laser spot and the position of the particle was inferred from the timing of detected fluorescence photons. The signal-processing was performed entirely in analog electronics. This lock-in scheme had a minimum latency of 25 μs, but could not implement the ideal trapping algorithm due to limitations of analog signal-processing. We also switched from a polydimethylsiloxane (PDMS) trapping chamber first to one made of glass and later to one made of fused silica, decreasing the fluorescence background by a factor of 40 in the process. The result of all these improvements was the ability to trap biomolecules as small as 15 nm diameter in aqueous solution [46].
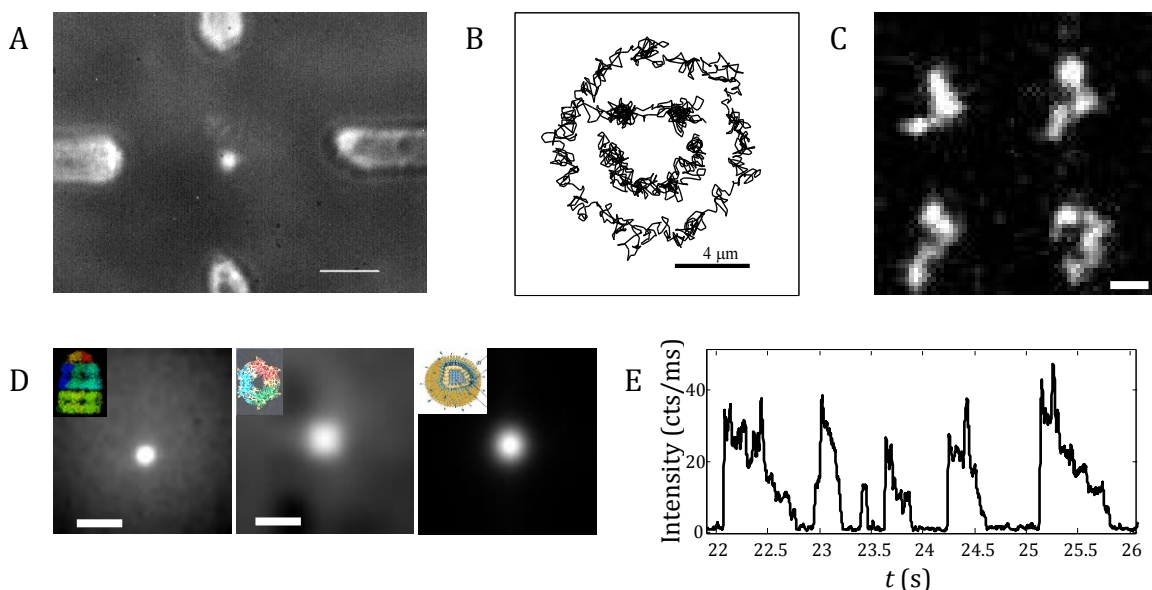
Figure 1-3 Trapping with the ABEL trap. (A) Single 200 nm diameter fluorescent polystyrene nanosphere. Scale bar, 5 μm. (B) Trajectory of a single 200 nm diameter nanosphere manipulated to draw out a smiley face over the course of 1 min. (C) Four images of a single fluorescently labeled molecule of l-DNA held in the ABEL trap. Nearly 60,000 such images were acquired and analyzed to probe the internal molecular dynamics. Scale bar, 1 μm. (D) Images of a trapped molecule of GroEL, B-phycoerythrin, and a CdSe quantum dot. Scale bar, 2 μm. (E) Time-trace of the fluorescence intensity as a series of multiply labeled molecules of the chaperonin MmCpn entered the trap, photobleached, and were lost. This strategy has been used to count the number of fluorescently labeled ATP bound by the chaperonin.

1.3.1 Photon-by-photon feedback

Figure 1-4 shows a schematic of the electrical and optical components of our current ABEL trap. One can think of the tracking system as a high speed confocal microscope, with a frame-rate of up to 100 kHz. These ultrafast scans are analyzed in real time by custom digital hardware, which locates the molecule within the scan pattern. The hardware calculates and applies feedback voltages based on every detected photon, with a latency of < 10 μs.
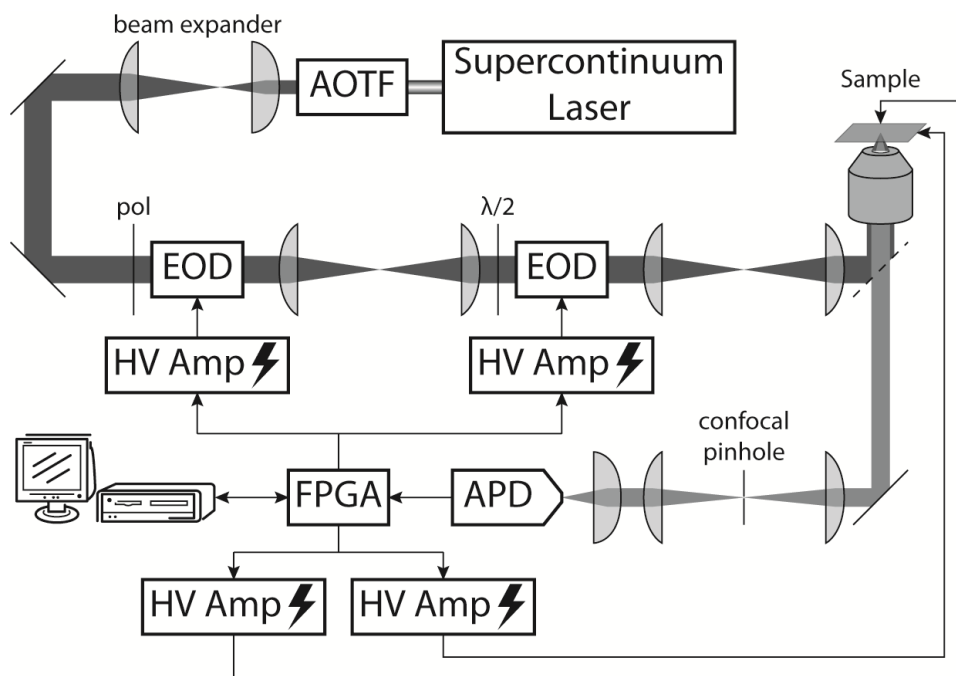
Figure 1-4 Optical layout of the ABEL trap. A 6 W supercontinuum laser emits light across the visible spectrum, up to eight spectral lines of which are selected by an acousto-optic tunable filter (AOTF). The beam is expanded, passed through a linear polarizer (pol), and scanned by two electro-optic beam deflectors (EOD). A half-wave Fresnel rhomb (λ/2) rotates the polarization by 90° between the EODs. Relay lenses are used to map the EOD deflections to pure 2D translations at the sample plane. The beam is reflected off a dichroic mirror (dashed line) and focused on the sample. Emitted photons are collected by the objective and filtered through the dichroic mirror and an emission filter (dotted line). The emission is re-imaged through a confocal pinhole and focused onto an avalanche photodiode (APD). Detected photons are reported to a field-programmable gate array (FPGA), which calculates appropriate feedback voltages to send to two high-voltage amplifiers (HV Amp) to apply to the sample. The FPGA also sets the deflection applied by the EODs via two additional high-voltage amplifiers.

The key innovations over previous designs are (1) improved photon-by-photon feedback, with higher speed, lower noise, and greater flexibility than previous systems; (2) adoption of electro-optic beam deflectors (EODs) that allow higher speed laser scanning (up to 100 kHz), at multiple wavelengths simultaneously; and (3) a broadband supercontinuum light source that allows us to study any fluorophore that can be excited in the visible part of the spectrum.

23

1.3.2 Illumination System

Now we discuss in more detail the layout of Figure 1-4. The light source is a 6 W supercontinuum laser (Fianium SC-450-6) that emits across the visible and near infrared spectrum. Up to eight spectral lines are selected by an acousto-optic tunable filter (AOTF, Crystal Technologies AODS 20160). This choice of illumination is crucial because it allows us to illuminate the sample with any wavelength or combination of wavelengths without re-aligning the optics. It is complicated to align multiple beams from different sources onto a trapped particle, and the present approach obviates that challenge.

Two EODs (ConOptics, Danbury CT) steer the position of the beam. These EODs allow much faster beam deflection compared to the AODs used in previous experiments (1 MHz vs. 50 kHz). Furthermore the EODs work throughout the visible spectrum while AODs require realignment for each wavelength.

The optical system is designed to bring the illumination to a sharp focus and to convert the EOD deflections into pure translations of the beam in the plane of the sample (without any coupling between the EOD deflection and the *direction* of the beam at the sample). This design is achieved through a series of relay lenses that image the *x*-axis EOD onto the *y*-axis EOD, and then image both EODs onto the back-aperture of the objective. The EODs are polarization sensitive, so a polarizer is placed before the first EOD and a half-wave Fresnel rhomb rotates the plane of polarization by $90°$ between the EODs. The excitation optics provide a laser beam that is precisely engineered spatially, spectrally, and temporally.
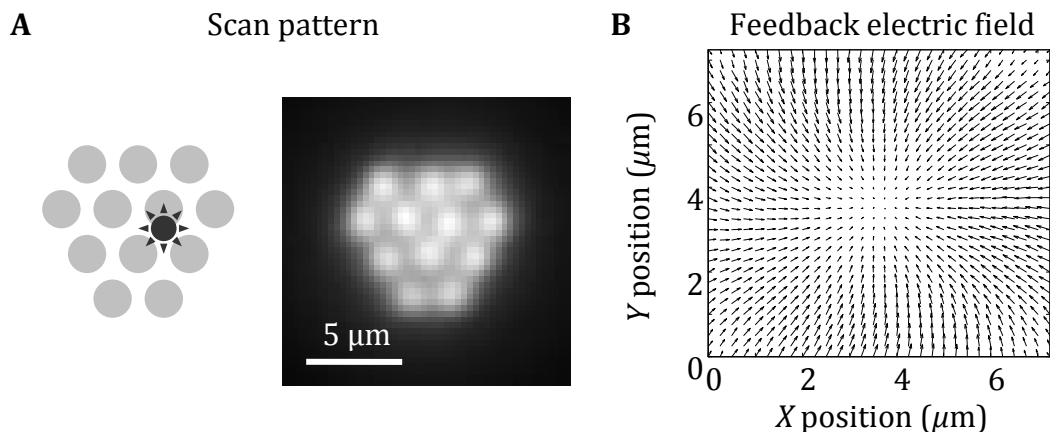
Figure 1-5 Confocal scan pattern. (A) Scan pattern for tracking single-molecule diffusion. (B) Calibration of tracking system obtained by scanning a fixed fluorescent bead through the tracking region and recording the pair of feedback voltages as a function of position.

An objective lens (Olympus; 60x, PlanAPO, N.A. 1.45) illuminates the trapping region from below, and captures fluorescence from a molecule in the trap. This fluorescence is separated from back-scattered excitation light by a dichroic mirror and a high quality emission filter. The light is then passed through a pinhole and imaged onto an APD (Perkin Elmer SPCM-AQRH-14). Figure 1-5 illustrates a 12-pixel confocal scan pattern. Typical confocal microscopes scan the beam in a square lattice, for reasons of simplicity of design and analysis. However, a square lattice is not the optimal pattern for tracking a small particle. A hexagonal lattice maximizes the uniformity of the time-average illumination, while also maximizing the sensitivity of the tracking system to small displacements of the particle.

The spacing of the pixels in Figure 1-5 A has been increased above the optimal value, to illustrate the discrete pixels in the scan pattern. The gray spots indicate the positions targeted by the laser beam. To test the accuracy of the tracking system, we placed a small fluorescent bead (represented as a star in Figure 1-5 A) on a piezoelectric

scanning stage and moved the particle in a raster pattern through the illuminated region. We recorded the feedback fields that would have been applied to the particle had it been free in solution. Figure 1-5 B shows these feedback fields, indicating that the tracking system is able to accurately generate a feedback field directed radially toward the origin.

1.3.3   Tracking and Feedback System

The most important feature of the ABEL trap is a hardware-based tracking system implemented in an FPGA (National Instruments PCI-7831R). The FPGA uses the precise arrival time of every detected photon to form an estimate of the location of the particle. This estimate is processed, photon-by-photon, to generate feedback voltages.

Figure 1-6 shows a schematic of our tracking and feedback algorithm for a single axis (e.g., the x-axis). An identical algorithm operates in the orthogonal direction. A register stores coordinates of the laser beam for the scan pattern (top row). These coordinates are sampled at a rate of 1 MHz and fed to one of the EODs via a high voltage amplifier. A second register records pulses from the APD (middle row). The occurrence of an APD pulse indicates that the molecule and the laser beam are likely to be in the same place. The FPGA records the position of the laser beam at the time of the APD pulse and stores this value in a third register. The positions of the photons detected in one scan cycle are averaged to form a raw measurement of the position of the particle.
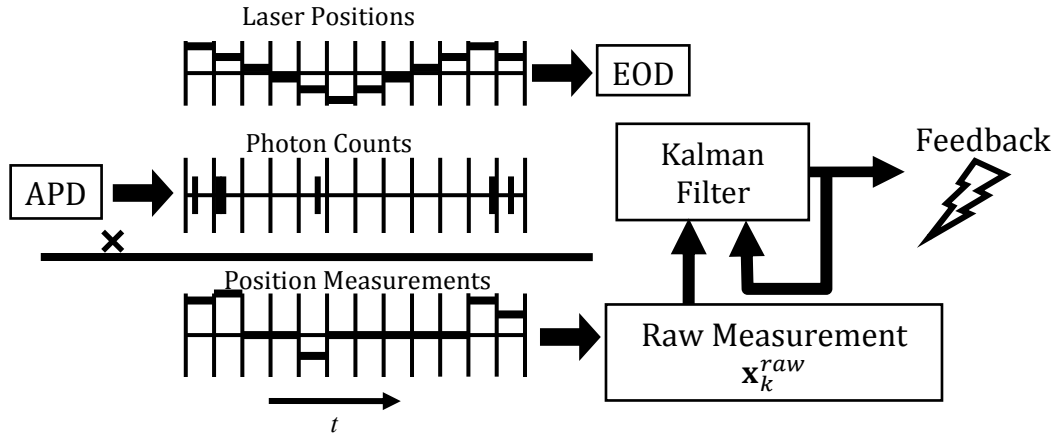
Figure 1-6 Tracking algorithm. The hardware controls the position of the laser (top) and records the arrival time of each photon (middle). On the basis of this information, the FPGA constructs a raw measurement of the particle position, which is fed into a recursive Kalman Filter that outputs the feedback voltage. APD, avalanche photodiode; EOD, electro-optic beam deflector.

1.3.4   Kalman filter signal processing

The raw position estimates from each scan of the laser are sent through a Kalman filter [74] implemented in the FPGA hardware. The Kalman filter is a means to keep track of both the particle position, $\mathbf{x}$, and the uncertainty with which this position is known, $\sqrt{p}$. At each time-step, the Kalman filter performs two tasks:

1. It predicts the location of the particle at time-step k, conditional on all the measurements up to time $k-1$. This prediction involves moving the estimate of the particle position in accord with the applied feedback voltages, and increasing the uncertainty in the particle's position in accord with its diffusive motion:

$$\hat{\mathbf{x}}_{k|k-1} = \hat{\mathbf{x}}_{k-1|k-1} + \mathbf{E}_{k-1}\mu\Delta t$$
$$\hat{p}_{k|k-1} = \hat{p}_{k-1|k-1} + 2D\Delta t$$

(1.4)

The subscripts $k|k-1$ indicate the prediction at time k, conditional on the information up to and including time $k-1$.

27

2. It adjusts the prediction from step (1) based on the raw measurement, $\mathbf{x}_k^{raw}$, obtained from the photons detected during step k. In the limit of fast scanning, the particle undergoes very little diffusive motion during a single laser scan. Then the uncertainty in the position of the particle is $w/\sqrt{n_k}$, where w is the width of the laser focus spot and n_k is the number of photons detected in scan k. The predicted position and the new data are combined with weighting factors determined by their relative uncertainty:

$$\hat{\mathbf{x}}_{k|k} = \frac{w^2 \hat{\mathbf{x}}_{k|k-1} + n_k \hat{p}_{k|k-1} \mathbf{x}_k^{raw}}{w^2 + n_k \hat{p}_{k|k-1}}$$

$$\hat{p}_{k|k} = \frac{w^2 \hat{p}_{k|k-1}}{w^2 + n_k \hat{p}_{k|k-1}}$$

(1.5)

Equations (1.4)–(1.5) are simple enough to be implemented at high speed in the FPGA.

One concern with the tracking scheme outlined here is its requirement for prior knowledge of parameter values. The prediction step [Equation (1.4)] requires knowledge of the diffusion constant (D) and electrical mobility (μ) of the trapped object, and the update step [Equation (1.5)] requires knowledge of the beam width (w) and the position of the beam at each point in the scan. The latter two parameters can be measured off-line by using a piezo stage to move an immobilized bead through the laser foci. The diffusion constant can be measured using FCS [23]. The electrical mobility can be measured using multi-spot FCS in the presence of an applied electrical field [75]. In our experience, the ability to trap is relatively insensitive to these parameter choices, so reasonable guesses can often substitute for precise values.

A key benefit of working with an FPGA is that the FPGA is connected to a computer so the user can set parameters in real-time. The user interacts with the feedback circuit as though it were software, but the circuit runs with the performance of custom hardware. This real-time tunability is essential to finding the optimal parameters for trapping a small molecule. The previous version of the ABEL trap, with feedback implemented in analog hardware [46], was limited in the feedback algorithms it could use due to the difficulty of performing some kinds of analog computations.

Two high-voltage amplifiers (Model 7602, Krohn-Hite), generate the scan voltages for the EODs, and two more identical amplifiers generate the feedback voltages for the trap. The necessary feedback voltage strength is highly dependent on the electrical mobility of the sample and on the geometry of the sample holder, but typically peak voltages less than 100 V are sufficient.

1.3.5 Microfluidics

The sample holder for the ABEL trap must be thin enough to confine molecules to within the focal depth of the objective (~ 1 µm) and must convey strong electric fields to the trap center. The sample holder we use (Figure 1-7) consists of a shallow (~ 600 nm) central trapping region flanked by four deeper (~ 15 µm) channels etched within a 2.5 mm square piece of fused silica. To enclose the channels, we irreversibly bond the etched device to the center of a 1" square fused silica cover slip using sodium silicate [76]. Fused silica is preferred due to its lower autofluorescence relative to glass or PDMS. The electrical resistance is much larger within the shallow trapping region than

29

anywhere else, greatly increasing the electrical field strength experienced by trapped molecules.

We use a cast piece of PDMS to contain excess fluid around the sides of the fused silica device and to hold the feedback electrodes in place. Fluid leakage around the corners of the device allows pressure equilibration without significant voltage loss. Damp tissue paper placed in an enclosed space containing the device alleviates sample evaporation. We use platinum electrodes to minimize electrochemical products.
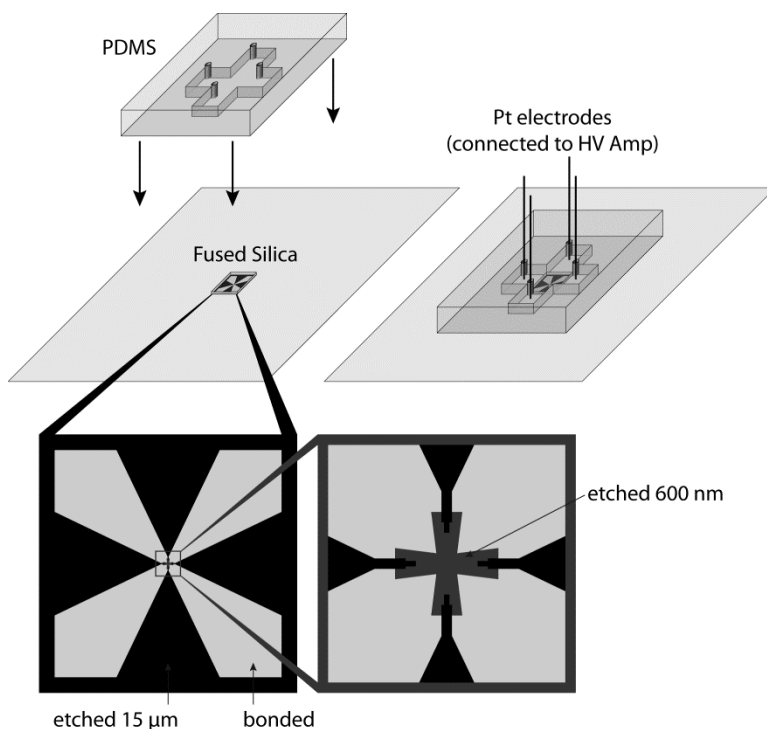
Figure 1-7 Sample holder for the ABEL trap. The fused silica sample cell contains a central trapping region 600 nm deep and deeper channels 15 μm deep as indicated. The etched 2.5 mm square piece of fused silica is bonded to a 1″ square fused silica coverslip. A cast piece of PDMS (top) is reversibly bonded to the coverslip to contain fluid and to hold the platinum electrodes in place. PDMS, polydimethylsiloxane.

1.4 Applications

Anti-Brownian traps have been used in a wide range of experiments and applications. The initial demonstrations were mostly focused on physics applications. For instance, the Mabuchi lab observed the fluorescence emission from semiconductor quantum dots, and found that the photon statistics showed anti-bunching [45]. This experiment was a conclusive proof that only a single quantum emitter was held in the trap. The Yang group at Berkeley used the feedback signal to reconstruct the diffusive trajectory of a single particle held in the trap. From the diffusion coefficient they determined the size of single particles [42]. They also added a spectroscopic readout with which they observed, for the first time, orientation-dependent scattering from metal nanoparticles [9]. In collaboration with W. E. Moerner, we generalized the feedback concept to include arbitrary position-dependent force fields [66], and thereby studied the motion of nanoparticles in double-well and power law shaped potentials. John Bechhoefer and coworkers continue to work in this area, and have derived the theoretical ramifications of simulating a physical potential with a feedback-mediated analogue [77, 78]. Other physics applications come from the Shapiro lab, which used electrokinetic control to position quantum dots precisely [50]. Combining the technique with an aqueous photoresist enabled the researchers to immobilize each quantum dot after guiding it to a precise destination [51]. In another application, the group measured the local density of optical states of a silver nanowire by positioning a quantum dot at varying distances from it [52].

Due to the complexity of most biophysical experiments, these were not feasible until anti-Brownian traps became robust enough to operate reliably. Recently, much progress has been made on the biophysical front. The Shapiro lab demonstrated the ability to manipulate yeast cells using video tracking and electrokinetic feedback, and was even able to steer multiple particles simultaneously [79]. Our early demonstration of trapping single virus particles, lipid vesicles, and proteins suggested a great many applications waiting to be explored [40]. We trapped single molecules of fluorescently labeled λ-DNA and recorded nearly 60,000 images of high-speed video of the internal conformational dynamics inside the trap [7, 8]. These videos allowed us, for the first time, to measure the spectrum of internal conformational modes of a single relaxed polymer molecule. McHale and Mabuchi followed up on those studies by applying their anti-Brownian tracking microscope to study additional details of the conformational dynamics of λ-DNA [63, 64].

The Moerner lab has been using their ABEL traps to study individual chaperonin molecules or complexes [65, 69]. By incubating the chaperonins with fluorescently labeled ATP, they can count, molecule-by-molecule, the number of bound ATP. Another study analyzed the complicated photophysics of individual trapped molecules of allophycocyanin, a naturally fluorescent light-harvesting protein, by analyzing their emission intensity and lifetime following photon absorption [68]. The Moerner lab also trapped individual nitrite reductase enzymes [70]. The dynamics of energy transfer from an appended fluorophore to copper ions within the trapped protein enabled them to measure the detailed kinetics of the enzymatic cycle. Similar approaches enabled the

32

Moerner lab to measure the interconversion of individual β_2-adrenergic receptors among its conformational states [71]. Finally, efforts to trap and observe ATP synthase complexes undergoing catalytic subunit rotation are in progress in the Börsch laboratory [80, 81, 82].

The Gratton lab has used a laser scanning approach coupled with two-photon microscopy to follow the motion of single fluorescently labeled loci on interphase chromatin [83]. These experiments found previously unobserved "hops" of the fluorescent spot. The group has since gone on to track proteins as they move through the nuclear pore complex of live cells [84]. The authors directly observed individual tagged nucleoporin molecules rapidly exchanging between two distinct locations within the pore. They could further distinguish between cargoes actively transported by the porins, and those that passively diffused through the pore, on the basis of the timescale of the motion. Another study tracked the export of Ebola virus protein multimers from human cells, finding that the export was driven by actin [85]. The Werner lab has also focused on tracking molecules in or on cells, including observations of quantum dot-labeled immunoglobulin proteins traveling along the plasma membrane and undergoing endocytosis [86]. The diversity of recent anti-Brownian studies suggests that many applications remain to be explored.

2

Optimal tracking of a Brownian particle

Optical tracking of a fluorescent particle in solution faces fundamental constraints due to Brownian motion, diffraction, and photon shot noise. Background photons and imperfect tracking apparatus further degrade tracking precision. Here we use a model of particle motion to combine information from multiple time-points to improve the localization precision. We derive successive approximations that enable real-time particle tracking with well controlled tradeoffs between precision and computational cost. We present the theory in the context of feedback electrokinetic trapping, though the results apply to optical tracking of any particle subject to diffusion and drift. We use numerical simulations and experimental data to validate the algorithms' performance.

2.1 Introduction

The motion of a molecule in solution encodes information about its size, interactions, and surroundings. Single-particle tracking experiments [87] have yielded information about the dynamics of molecules in the plasma membrane [88, 89], the walking mechanisms of motor proteins [90], and intracellular transport of nucleic acids [91] and protein complexes [86]. Anti-Brownian traps combine optical tracking with active feedback, applied via stage motion or electrokinetic drift, to confine a single particle within an observation volume for an extended time [1]. These devices have

34

yielded new insights into the dynamics of biomolecules [8, 65, 68] and nanoparticles [92] but face the additional challenge that the tracking must be performed in close to real time.

In choosing an imaging strategy, one typically faces a tradeoff between photon shot noise and Brownian motion. During a brief exposure a particle remains relatively localized in space, but the precision of the measurement is degraded by photon shot noise. Diffractive blurring causes each photon to carry imperfect information about the location of the particle, and background photons can contribute spurious information. During a long exposure, the photon statistics are improved but the precision of the measurement is degraded by Brownian motion. Specialized hardware can reach exposure times shorter than the mean interval between photons, so that each "image" consists of at most a few photons [57], while video cameras can achieve arbitrarily long exposure times.

Given a series of noisy position measurements, the fundamental challenge of particle tracking is to link these data into a trajectory. Naively, one might simply concatenate successive measurements. However, recent measurements often contain useful information about the present location, and thus one can combine data taken at different times to compute a more likely trajectory than is obtained by simple concatenation. Here we derive a hierarchy of algorithms for calculating likely trajectories. These algorithms allow tradeoffs between accuracy and computational efficiency.

For post-processing of tracking data we present an Assumed Density Filter (ADF) algorithm that achieves near-optimal performance in particle tracking by applying an assumed model of particle motion. This algorithm is useful to obtain maximum likelihood estimates of molecular transport coefficients (electrokinetic mobility and diffusion coefficient). Anti-Brownian traps require real-time information on particle location. We develop a Kalman filter algorithm which is a simplified and computationally efficient form of the ADF. The Kalman filter presumes knowledge, or an estimate, of the transport coefficients, and seeks to estimate the position of the particle. These theoretical results proved crucial to our efforts to trap individual fluorophores and other molecules in solution and to estimate the transport coefficients of trapped molecules [3].

Our ADF algorithm is a discrete-time recursive Bayesian estimator [93, 94]. This approach uses a stochastic model of particle motion to combine a series of noisy measurements into a maximum likelihood estimate of the present position. We model the motion as Brownian diffusion plus electrokinetic drift, and we explicitly include Poisson-distributed photon shot noise and background photons. A related model [44, 61, 95] previously treated the noise and background as Gaussian-distributed white noise. The key innovations in the present work are to use a nonlinear filter, the ADF, to enhance tracking accuracy, and to account for the discreteness of photon arrivals in both the Kalman filter and the ADF. We present our model in the context of the anti-Brownian electrokinetic trap (ABEL trap) [39], but the treatment can be adapted to other uses (e.g. for other feedback modalities or in the absence of feedback).

36
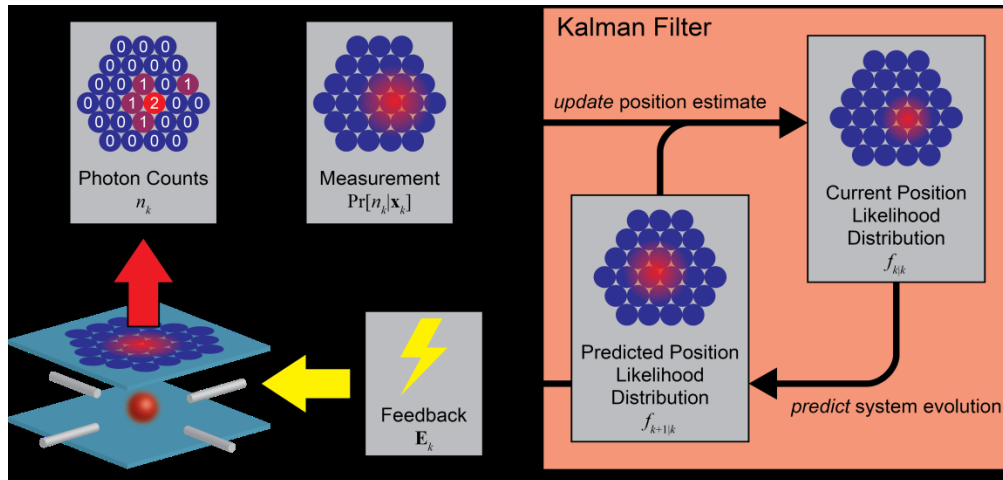
Figure 2-1 Tracking and feedback in an anti-Brownian electrokinetic trap. A fluorescent particle diffuses in a quasi-two-dimensional sample chamber at the center of four platinum electrodes. A focused laser is scanned through a set of discrete spots in the sample plane, triggering the particle to emit fluorescence when the laser overlaps with the particle. Detected photons are tallied and assigned to laser spots according to their detection time. A Kalman filter combines this data with a prediction for the location of the particle based on previous data to generate an updated position estimate. The position estimate is used to calculate feedback voltages which are applied to counteract the particle's motion.

The ABEL trap uses fluorescence microscopy to track a particle diffusing in two dimensions, and applies electrokinetic forces to oppose the observed motion. Out-of-plane motion is blocked by the walls of the sample chamber. The earliest ABEL trap [39] imaged particles in the trap on a camera and was consequently limited by frame readout time. Recent incarnations [3, 6] scan a focused laser beam among a set of discrete spots in the sample plane, simultaneously tallying photon arrivals on a single-point detector, and determine particle location from the position of the laser at the instant each photon is detected. Our implementation scans the laser among 27 spots in a hexagonal lattice, with a dwell time of 3.1 μs at each spot (Figure 2-1). The challenge is to construct a likelihood distribution for the particle's position given the history of detected photons. We advise caution in applying the mathematics described here when

the underlying motion is not Brownian (e.g. active transport); such cases would be better treated by constructing a variety of models and selecting the one best fit by the data.

2.2 General treatment

We consider the case of a single fluorescent particle diffusing in free solution, where the particle diameter is much less than the optical wavelength. This particle might have complex internal structure, but the structure is not optically resolvable, so we treat the particle as a point-like emitter and refer to it generically as a "fluorophore". Although our instrument tracks particles in two dimensions, the mathematical description is similar for one- or three-dimensional geometries.

Assuming laser intensity below saturation, the rate γ at which photons are detected is well approximated as a Gaussian function of the displacement of the fluorophore from the center of the laser spot, plus a constant background rate [96, 97]. Mathematically,

$$\gamma(x) = s \exp\left(-\frac{1}{2}(\mathbf{x} - \mathbf{c})^T \mathbf{W}^{-1}(\mathbf{x} - \mathbf{c})\right) + b, \tag{2.1}$$

where s is the maximum "signal" photon rate (in photons per second) from the fluorophore, b is the "background" photon rate (also in photons per second), $\mathbf{x}$ is the particle position (written as a column vector), $\mathbf{c}$ is the laser spot center, $\mathbf{W}$ is the spatial covariance of the spot, ^{T} denotes transposition, and $^{-1}$ denotes matrix inversion. The probability of detecting n photons during a time bin of length Δt during which the laser is stationary is the Poisson distribution

$$\Pr[n|\mathbf{x}] = \frac{(\gamma(x)\Delta t)^n e^{-\gamma(x)\Delta t}}{n!}. \tag{2.2}$$

Throughout the experiment, the fluorophore diffuses with diffusion coefficient D. In the case of the ABEL trap, a series of electric fields $\mathbf{E}_k$ are applied to the trap, imparting motion to the fluorophore in proportion to its electrokinetic mobility μ. The probability distribution of the molecule's motion $\Delta\mathbf{x}$ during time step k is

$$g_k(\Delta\mathbf{x}) = \frac{\exp\left(-\dfrac{|\Delta\mathbf{x} - \mu\Delta t\mathbf{E}_k|^2}{4D\Delta t}\right)}{4\pi D\Delta t}. \tag{2.3}$$

This equation is indifferent to the method by which the applied electric field $\mathbf{E}_k$ is selected. In the case of the ABEL trap, the field strength is modulated so as to counteract the observed diffusion,

$$\mathbf{E} = -\frac{\hat{\mathbf{x}}}{\mu\Delta t}, \tag{2.4}$$

where $\hat{\mathbf{x}}$ is the most recent estimate of the molecule's position, but Equation (2.3) and the following derivation remain valid if $\mathbf{E}$ is held constant or modulated independently of the molecular motion.

The transport coefficients μ and D reflect the charge, size, and interactions of the particle, so extracting these (possibly time-dependent) parameters is a goal of particle tracking and feedback trapping. The molecular brightness s, which is sensitive to the electrochemical environment of the fluorophore, may also be of interest.

Let $\{n_j, j \leq k\}$ denote the complete history of photon counts in discrete time bins up to and including bin k, where each bin corresponds to a new laser position. We seek to construct the likelihood distribution $\Pr[\mathbf{x}_k|\{n_j, j \leq k\}]$ for the position of the

fluorophore during the kth bin. The position likelihood distribution $f_{a|b} \equiv \Pr[\mathbf{x}_a | \{n_j, j \leq b\}]$ is estimated recursively from:

$$f_{k|k} = L_k^{-1} \Pr[n_k | \mathbf{x}_k] f_{k|k-1} \tag{2.5}$$

$$f_{k|k-1} = \int g_{k-1}(\mathbf{x}_k - \mathbf{x}_{k-1}) f_{k-1|k-1} d\mathbf{x}_{k-1} \tag{2.6}$$

where the integral is over the entire two-dimensional plane and $L_k \equiv \Pr[n_k | \{n_j, j \leq k-1\}]$. Equations (2.5) and (2.6) are known as "update" and "prediction" equations, respectively, and together constitute a "recursive Bayesian estimator" of the fluorophore position. To be applicable, these equations require that the molecule's unperturbed motion be truly Brownian (e.g., no significant momentum), that the effect of the electric field $\mathbf{E}$ be independent of the molecule's position $\mathbf{x}$, and that the motion of the fluorophore during each bin be negligible.

2.3 Gaussian assumed-density filter (ADF)

In principle, Equations (2.1)–(2.6) enable exact calculation of the likelihood distribution of particle position given a set of photon counts and corresponding laser positions. In practice, it is unfeasible to perform this calculation in real-time at the speed required to track fast-moving fluorophores – indeed, in our experience the full calculation is too slow even for post-processing (see Section 2.6). The difficulty stems from the complicated shape of the measurement distribution [Equation (2.2)], which renders the estimate distribution analytically intractable if no approximations are made. On the other hand, treating the full probability distributions numerically is impractical

because of the slowness of two-dimensional numerical convolution [Equation (2.6)], which needs to be computed every time the laser moves to a new spot (every 3.1 μs in our implementation). Propagating the distribution on a 128×128 grid, for instance, requires >10^5 multiplication operations for each convolution. It is therefore necessary to make approximations. Myriad schemes have been devised to handle nonlinear measurements (several of which are described in [98]). The Gaussian assumed-density filter (ADF) [99, 100] is well suited to particle tracking in the presence of shot noise, Brownian motion, and background fluorescence. An ADF is a type of recursive Bayesian estimator in which the complicated shape of the likelihood densities $f_{a|b}$ are approximated by simpler, mathematically tractable distributions.

Let us assume that the likelihood functions $f_{a|b}$ are normally distributed with mean $\hat{\mathbf{x}}_{a|b}$ and covariance $\hat{\boldsymbol{\Sigma}}_{a|b}$; that is,

$$f_{a|b} \approx \mathrm{N}\left(\hat{\mathbf{x}}_{a|b}, \hat{\boldsymbol{\Sigma}}_{a|b}\right)$$

$$\equiv \left(2\pi \left|\hat{\boldsymbol{\Sigma}}_{a|b}\right|^{1/2}\right)^{-1} \exp\left(-\tfrac{1}{2}(\mathbf{x} - \hat{\mathbf{x}}_{a|b})^T \hat{\boldsymbol{\Sigma}}_{a|b}^{-1}(\mathbf{x} - \hat{\mathbf{x}}_{a|b})\right). \tag{2.7}$$

This shape of distribution vastly simplifies the prediction step [Equation (2.6)], because the convolution of two normal distributions is another normal distribution. Therefore, we can immediately reduce Equation (2.6) to

$$\hat{\mathbf{x}}_{k|k-1} = \hat{\mathbf{x}}_{k-1|k-1} + \mu \Delta t \mathbf{E}_{k-1}$$

$$\hat{\boldsymbol{\Sigma}}_{k|k-1} = \hat{\boldsymbol{\Sigma}}_{k-1|k-1} + 2D \Delta t \mathbf{I}. \tag{2.8}$$

On the other hand, the update step [Equation (2.5)] does not preserve the Gaussian shape of the likelihood distribution. Instead, combining Equations (2.1), (2.2), (2.5), and (2.7) produces

$$f_{k|k} = L_k^{-1}(n_k!)^{-1} \left(S \exp\left(-\frac{(\mathbf{x}-\mathbf{c})^T \mathbf{W}^{-1}(\mathbf{x}-\mathbf{c})}{2}\right) + B \right)^{n_k}$$
$$\times \exp\left(-\left(S \exp\left(-\frac{(\mathbf{x}-\mathbf{c})^T \mathbf{W}^{-1}(\mathbf{x}-\mathbf{c})}{2}\right) + B\right)\right) \mathrm{N}\left(\hat{\mathbf{x}}_{k|k-1}, \widehat{\boldsymbol{\Sigma}}_{k|k-1}\right)$$

(2.9)

where $S \equiv s\Delta t$ and $B \equiv b\Delta t$. This distribution is no longer normally distributed, but we can approximate it as such by calculating its mean and covariance and dropping higher moments. An alternative strategy would be to project the posterior distribution onto a finite sum of Gaussian distributions, similar to a Gaussian sum filter [101]. In principle, this approach could increase the accuracy of the estimator, at the expense of greater computational complexity; we have not attempted such a strategy.

To calculate the mean and covariance of the distribution [Equation (2.9)], we first rearrange it as

$$f_{k|k} = L_k^{-1} \sum_{m=0}^{\infty} l_m \mathrm{N}\left(\hat{\boldsymbol{\chi}}_m, \widehat{\boldsymbol{\Psi}}_m\right)$$

(2.10)

where

$$l_m \equiv e^{-B} \sum_{i=\max(n_k-m,0)}^{n_k} \frac{(-1)^{m+i-n_k} B^i S^m}{(n_k-i)!\, i!\, (m+i-n_k)!} \frac{\left|\widehat{\mathbf{\Psi}}_m\right|^{1/2}}{\left|\widehat{\mathbf{\chi}}_m\right|^{1/2}}$$

$$\times \exp\left(-\frac{m\left(\hat{\mathbf{x}}_{k|k-1}-\mathbf{c}_k\right)^T \left(m\widehat{\mathbf{\Sigma}}_{k|k-1}+\mathbf{W}\right)^{-1}\left(\hat{\mathbf{x}}_{k|k-1}-\mathbf{c}_k\right)}{2}\right) \tag{2.11}$$

$$\widehat{\mathbf{\chi}}_m \equiv \widehat{\mathbf{\Psi}}_m\left(\widehat{\mathbf{\Sigma}}_{k|k-1}^{-1}\hat{\mathbf{x}}_{k|k-1} + m\mathbf{W}^{-1}\mathbf{c}_k\right)$$

$$\widehat{\mathbf{\Psi}}_m \equiv \left(\widehat{\mathbf{\Sigma}}_{k|k-1}^{-1} + m\mathbf{W}^{-1}\right)^{-1}.$$

Equation (2.10) rewrites Equation (2.9) as an infinite sum of normal distributions. The overall normalization factor L_k is simply

$$L_k = \sum_{m=0}^{\infty} l_m. \tag{2.12}$$

The mean and covariance are

$$\hat{\mathbf{x}}_{k|k} = \int \mathbf{x} f_{k|k} d\mathbf{x} = L_k^{-1} \sum_{m=0}^{\infty} l_m \widehat{\mathbf{\chi}}_m \tag{2.13}$$

$$\widehat{\mathbf{\Sigma}}_{k|k} = \left(\int \mathbf{x}\mathbf{x}^T f_{k|k} d\mathbf{x}\right) - \hat{\mathbf{x}}_{k|k}\hat{\mathbf{x}}_{k|k}^T$$

$$= \left(L_k^{-1} \sum_{m=0}^{\infty} l_m\left(\widehat{\mathbf{\chi}}_m\widehat{\mathbf{\chi}}_m^T + \widehat{\mathbf{\Psi}}_m\right)\right) - \hat{\mathbf{x}}_{k|k}\hat{\mathbf{x}}_{k|k}^T \tag{2.14}$$

These series are convergent by the alternating series test and so are well approximated by partial sums. We typically truncate each summation when subsequent terms contribute less than some fraction $\varepsilon \ll 1$ (typically 10^{-6}) to the total.

The normalization factor L_k is the likelihood of observing n_k photons given all previous observations and the system parameters; that is, $L_k \equiv \Pr\left[n_k \middle| \{n_j, j \le k - 1\}; D, \mu\right]$ (parameter conditioning previously suppressed for brevity), so the log-likelihood of the entire trajectory is

$$\ln(\Lambda) = \sum_k \ln(L_k). \tag{2.15}$$

Maximum likelihood parameter estimates are found by gradient ascent of this function. Simulations testing the performance of this maximum likelihood estimator are in Section 2.6, below. Application to experimental data is in Section 2.7 and in Chapter 3 [3].

2.4 Kalman filter

Equations (2.12)–(2.14) can be evaluated quickly enough for maximum likelihood parameter estimation in post-processing, but are still too complicated to be computed in real-time (i.e. during a 3.1 µs sampling bin) on current hardware. To simplify further the calculation, we map the ADF onto a Kalman filter. A Kalman filter can be thought of as a special type of assumed-density filter, in which the measurement distribution [Equation (2.2)], the prediction equation [Equation (2.3)], and the estimate distributions $f_{a|b}$ are all taken to be Gaussian.

To map the ADF onto a Kalman filter, we return to Equation (2.10) and restrict ourselves to scenarios in which the signal-to-background ratio is high ($B \ll S$) and the scan rate is fast relative to the rate of photon detection ($S \ll 1$). In this case, the dominant term in the series is the one with $m = n_k$ and $i = 0$. So, the update step [Equations (2.13) and (2.14)] becomes

$$\hat{\mathbf{x}}_{k|k} = \left(\hat{\boldsymbol{\Sigma}}_{k|k-1}^{-1} + n_k \mathbf{W}^{-1}\right)^{-1}\left(\hat{\boldsymbol{\Sigma}}_{k|k-1}^{-1}\hat{\mathbf{x}}_{k|k-1} + n_k \mathbf{W}^{-1}\mathbf{c}_k\right)$$

$$\hat{\boldsymbol{\Sigma}}_{k|k} = \left(\hat{\boldsymbol{\Sigma}}_{k|k-1}^{-1} + n_k \mathbf{W}^{-1}\right)^{-1}. \tag{2.16}$$

These equations, together with Equation (2.8) allow propagation of a Gaussian likelihood function for the particle's position using five variables (two for the position, three for the covariance), and are an instance of the well-known Kalman filter [102, 103], with associated likelihood function

$$L_k^{kal} = \frac{S^{n_k}}{n_k!} \frac{|\hat{\mathbf{\Psi}}_m|^{1/2}}{|\hat{\mathbf{\chi}}_m|^{1/2}} \exp\left(-\frac{n_k(\hat{\mathbf{x}}_{k|k-1}-\mathbf{c}_k)^T (n_k\hat{\mathbf{\Sigma}}_{k|k-1}+\mathbf{W})^{-1}(\hat{\mathbf{x}}_{k|k-1}-\mathbf{c}_k)}{2}\right) \qquad (2.17)$$

In the common case that $\mathbf{W}$ is diagonal (any beam asymmetry is along the same axes that the feedback is applied), the Kalman covariance is also diagonal and the cross-covariance term can be dropped. If the beam profile is circularly symmetric, then $\mathbf{W} = w^2\mathbf{I}$ for some w, and the variance in the x- and y-dimensions is always equal and can be denoted $\hat{p}_{a|b}$. This yields the simple expressions

$$\hat{\mathbf{x}}_{k|k} = \frac{w^2\hat{\mathbf{x}}_{k|k-1} + n_k\hat{p}_{k|k-1}\mathbf{c}_k}{w^2 + n_k\hat{p}_{k|k-1}}$$

$$\hat{p}_{k|k} = \frac{w^2\hat{p}_{k|k-1}}{w^2 + n_k\hat{p}_{k|k-1}}$$

(2.18)

The prediction step [Equation (2.8)] becomes

$$\hat{\mathbf{x}}_{k|k-1} = \hat{\mathbf{x}}_{k-1|k-1} + \mu\Delta t\mathbf{E}_{k-1}$$

$$\hat{p}_{k|k-1} = \hat{p}_{k-1|k-1} + 2D\Delta t$$

(2.19)

These four equations enable high-speed two-dimensional tracking of a particle using just three variables.

One concern with the tracking scheme outlined here is its requirement for prior knowledge of parameter values. Four parameters are required: the laser spot locations ($\mathbf{c}_k$), the laser spot covariance ($\mathbf{W}$ or w^2), the diffusion constant (D), and the

45

electrokinetic mobility (μ). The first two can be measured by scanning a point source such as a surface-immobilized fluorescent bead through the laser during a scan. The population-average diffusion constant and electrokinetic mobility can be measured independently using multi-spot fluorescence correlation spectroscopy (FCS) in the presence of an applied electric field [104]. Alternatively, guesses can be made (or trapping can be attempted using a variety of parameter values), and maximum likelihood estimates can be calculated from trapping data and used to inform later experiments. Recently, a method for adaptive real-time parameter tuning was experimentally realized [6], in which trapping parameters were iteratively adjusted to "whiten" the autocorrelation of the innovation sequence, taking advantage of the fact that parameter errors give rise to correlations in the innovation (the displacement of each newly measured position from the prior estimate).

The ADF and the Kalman filter differ only in the update step. The Kalman update equation [Equation (2.16)] is a simple linear combination of the prior estimate mean and the new measurement. The relative weighting is tuned by the relative confidences in the new measurement and in the prior estimate, but does not itself depend on the innovation. The ADF update also adjusts the prior estimate mean along the direction of each new measurement, but its relative weighting is itself a complicated nonlinear function of the innovation. This allows the ADF to better account for the true shape of the measurement distribution.

The assumption that $B \ll S$ means that the Kalman filter does not distinguish between signal and background photons, so spurious counts significantly degrade the

46

estimate. The assumption that $S \ll 1$ introduces a subtle bias, most noticeable when no

photons are observed during a bin ($n_k = 0$). Absence of photons suggests that the

particle is not in the laser spot, and so is more likely to be elsewhere. Analogously, if one

were to peer through a telescope and see darkness, one could declare that the moon

was *not* where the telescope was pointed. The ADF update step [Equation (2.13)]

accounts for this effect, while the Kalman update step [Equation (2.16)] does not.

Consequently, the Kalman estimator is slightly biased towards the most recent bin,

leading to a modulation of the estimated particle position at the frequency of the laser

scan.

2.5   Fundamental constraints

The Kalman filter is simpler and faster than the ADF, but has greater tracking

error. In Section 2.6, we present simulations quantifying the difference in performance

between the two filters; here, we derive analytical estimates of these differences.

In each update step, the ADF incorporates new information about the

fluorophore position. The information gain is quantified by the Fisher information

matrix of the updated estimate, the $(a, b)^{\text{th}}$ element of which is

$$-\langle\frac{\partial^2 \ln(L_k)}{\partial x^{(a)}\partial x^{(b)}}\rangle = -\langle\frac{\partial^2 \ln(\text{Pr}[n_k|\mathbf{x}_k])}{\partial x^{(a)}\partial x^{(b)}}\rangle - \langle\frac{\partial^2 \ln(f_{k|k-1})}{\partial x^{(a)}\partial x^{(b)}}\rangle \qquad (2.20)$$

where angle brackets indicate the expectation (integral) over the prior probability

distribution for the molecule's position ($f_{k|k-1}$). The last term is the Fisher information

of the prior distribution, which, under the Gaussian assumption of the ADF, is simply

$\widehat{\mathbf{\Sigma}}_{k|k-1}^{-1}$. Of greater interest is the first term, which is the average information gain during

each time bin. Substitution of Equations (2.1)–(2.2) into this term and dropping the time

bin subscripts k for clarity gives

$$F_{ADF}^{(a,b)} \equiv -\langle\frac{\partial^2\ln(\Pr[n|\mathbf{x}])}{\partial x^{(a)}\partial x^{(b)}}\rangle = \langle\frac{1}{\Gamma(\mathbf{x})}\frac{\partial\Gamma(\mathbf{x})}{\partial x^{(a)}}\frac{\partial\Gamma(\mathbf{x})}{\partial x^{(b)}}\rangle \tag{2.21}$$

where $\Gamma \equiv \gamma\Delta t$.

The overall average information gain for an arbitrary bin is this expression

averaged over the laser scan positions $\mathbf{c}_k$. If the trapping region is well sampled by the

scan pattern (the spots are spaced regularly, the distance between them is less than or

comparable to the width of the beam, and the overall size of the pattern is much larger

than the spread of the beam width around the particle), then the sum over the laser

scan positions is well approximated by an integral. Under these conditions, the Fisher

information matrix for a two-dimensional scan is approximately

$$\overline{\mathbf{F}_{ADF}} \approx \mathbf{W}^{-1}\left(1 + \frac{B}{S}\mathrm{Li}_2\left(-\frac{S}{B}\right)\right)\overline{\Gamma}_s \tag{2.22}$$

where over-bars indicate averaging over the bins k of the scan pattern, Li_2 is the

polylogarithm function of order 2, and $\overline{\Gamma}_s$ is the scan-averaged expected number of

signal photons per time bin. (Under the given assumptions, $\overline{\Gamma}_s \approx \frac{2\pi S|\mathbf{W}|^{1/2}}{L\Delta c^2}$, where L is

the number of spots in the scan pattern and Δc is the spacing between scan positions.)

The inverse of the Fisher information is the Cramér-Rao lower bound on the

measurement error covariance associated with a particular scan pattern and signal-to-

background ratio. In the absence of background counts, therefore, the measurement

covariance is simply the beam covariance divided by the number of detected photons,

akin to the localization precision of super-resolution techniques based on Gaussian fitting [90]. Unsurprisingly, the measurement covariance increases for $B > 0$.

Assuming that the ADF estimator is efficient (i.e., it makes optimal use of all available information), we approximate the steady-state value of the estimate covariance matrix (following the update step) according to

$$\overline{\boldsymbol{\Sigma}^{-1}} \approx \overline{\mathbf{F}_{ADF}} + (\overline{\boldsymbol{\Sigma}} + 2D\Delta t\mathbf{I})^{-1}. \tag{2.23}$$

All of the matrices commute, so we arrive at a final value for the average ADF tracking covariance of

$$\overline{\boldsymbol{\Sigma}} \approx D\Delta t \left(\left(\frac{2}{D\Delta t} \overline{\mathbf{F}_{ADF}^{-1}} + \mathbf{I} \right)^{1/2} - \mathbf{I} \right) \tag{2.24}$$

where the square root is understood to indicate the unique positive definite symmetric matrix square root.

To determine the Kalman filter tracking error, we start by combining the update and prediction equations for its variance [Equations (2.8) and (2.16)]

$$\widehat{\boldsymbol{\Sigma}}_{k|k} = \left(\left(\widehat{\boldsymbol{\Sigma}}_{k-1|k-1} + 2D\Delta t\mathbf{I} \right)^{-1} + n_k \mathbf{W}^{-1} \right)^{-1}. \tag{2.25}$$

Neglecting fluctuations due to stochastic photon arrivals, this equation achieves the steady-state value

$$\overline{\widehat{\boldsymbol{\Sigma}}_{k|k}} \approx D\Delta t \left(\left(\frac{2}{D\Delta t} \frac{\mathbf{W}}{\overline{\Gamma}} + \mathbf{I} \right)^{1/2} - \mathbf{I} \right) \tag{2.26}$$

where $\overline{\Gamma}$ is the average number of photons detected per bin. Because the derivation of the Kalman filter assumed the absence of background, this equation is only accurate for $B = 0$. In fact, Equation (2.26) reproduces the background-free value of the ADF

tracking error [Equation (2.24)], indicating that the filters' tracking performance differs appreciably only when the background is significant.

Introduction of background photons broadens the spread of the detected photons around the molecule's true position, increasing the effective beam waist and degrading the Kalman filter's performance. The magnitude of the broadening is difficult to calculate because it depends on the distribution of the particle in the trap. The ADF tracking error estimate [Equation (2.24)] is a lower bound on the Kalman tracking error in the presence of background; we use simulations (Section 2.6) to quantify performance more precisely.

In the limit of fast scanning ($\Delta t \ll \sqrt{2w^2/D\gamma}$), the background-free tracking error of the ADF and the Kalman filter [Equation (2.26)] simplifies to

$$\bar{\Sigma} \approx \sqrt{\frac{2D\mathbf{W}}{\bar{\gamma}_s}} \qquad (2.27)$$

This result can be interpreted as the product of the width of the laser spot and the mean distance the particle diffuses between photon detection events, and reproduces the tracking error formula for a continuous-time linear filtration scheme based on lock-in detection [61].

During the update step of either the ADF or Kalman filter, the prior estimate mean is multiplied by a weighting factor κ that reflects the confidence that it retains validity. In the case of the Kalman filter with no background and circular symmetry [Equation (2.18)], the weighting factor is

$$\kappa = \frac{w^2}{w^2 + n_k \hat{p}_{k|k-1}}. \tag{2.28}$$

Using the approximate average tracking error from Equation (2.26), the average weighting factor is

$$\bar{\kappa} = \frac{w^2}{w^2 + \bar{\Gamma}D\Delta t \left(\left(\frac{2}{D\Delta t}\frac{w^2}{\bar{\Gamma}} + 1 \right)^{1/2} + 1 \right)}. \tag{2.29}$$

The estimate constructed j bins ago will typically be weighted by κ^j. Recasting in terms of elapsed time $T \equiv j\Delta t$ and setting $\Delta t \to 0$ gives

$$\overline{\kappa_T} \approx \exp\left(-\frac{\sqrt{2D\bar{\gamma}}}{w}T \right). \tag{2.30}$$

Thus, the timescale during which information from each photon retains utility is

$$\tau \approx \frac{w}{\sqrt{2D\bar{\gamma}}}. \tag{2.31}$$

The denominator in Equation (2.31) represents the average velocity of the particle between photon detection events. This formula has also been derived in the continuous-time case [61].

To illustrate, Alexa 647 has a diffusion constant of 330 μm^2/s [105], and we typically have $\overline{\gamma_s} \approx 50$ kHz and $\overline{\gamma_b} \approx 9$ kHz (corresponding to $S \approx 1.5$ and $B \approx 0.03$ for our scan pattern). Our 27-point scan pattern has spot spacing of 0.65 μm, beam width $w \approx 0.4$ μm, and scan rate of 12 kHz. Equation (2.24) predicts a minimum tracking error of 315 nm. The timescale over which measurements retain utility [Equation (2.31)] is approximately 70 μs, corresponding to a scan rate of 14 kHz. Our choice of 12 kHz

approaches this limit, and trap performance shows little change when the scan rate is increased.

2.6   Simulation: trapping single fluorophores in solution

To demonstrate application to trapping single fluorophores in solution, we simulated trapping experiments at a variety of parameter values and calculated maximum likelihood parameter estimates from the simulated data. All calculations were performed in MATLAB. The default transport coefficients were $D = 100\ \mu m^2/s$, $\mu = -1000\ \mu m^2/(V\ s)$. The feedback electric field strength was capped at 3 V/μm. The expected photon count rate for a molecule in the center of the trap was set to 100 kHz, with a background count rate of 25 kHz. The laser scan matched our experimental setup, with 27 spots of width $w = 0.4\ \mu$m on a hexagonal lattice of 0.65 μm spacing, scanned with a per-spot dwell time $\Delta t = 3.1\ \mu$s. The Kalman filter tracking and feedback algorithm also matched the experimental implementation as closely as possible. All parameters were held at these values unless otherwise noted. For each parameter set, we simulated one hundred individual molecular traces, each of length 0.1 s. Molecules were considered successfully "trapped" if their maximum displacement from the trap center never exceeded 3.4 μm.

We compared the tracking accuracy of the Kalman filter, ADF, and a full recursive Bayesian estimator [Equations (2.5) and (2.6)] on each simulated molecular trajectory. The model parameters were set to match the true simulated values. The full Bayesian estimator, which was propagated on a 128×128 grid with 38 nm spacing (encompassing

52

the entire scan pattern), was indistinguishable from the ADF algorithm, except for a few

cases in which its performance was hindered by the grid spacing. All of the algorithms

were programmed in C using the MATLAB mex interface; the ADF typically ran more

than 1500 times faster than the full grid estimator, and the Kalman filter ran 9 times

faster than the ADF.
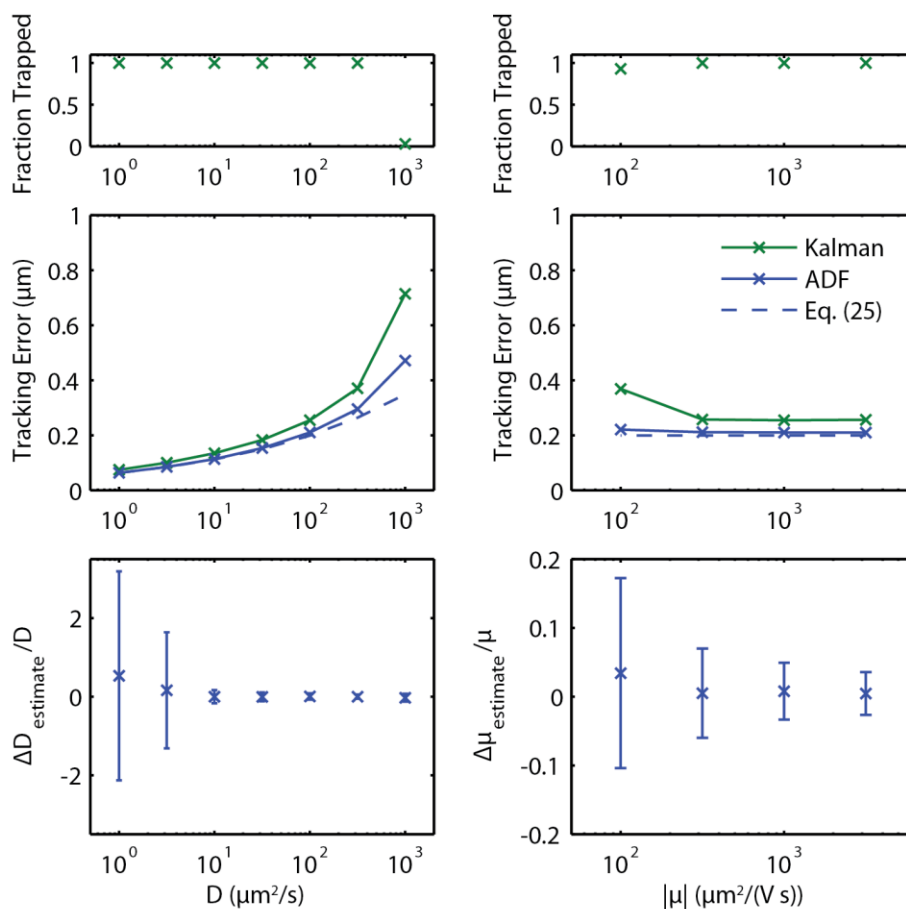
Figure 2-2 Simulated trapping and parameter fitting as a function of diffusion coefficient (left) or electrokinetic mobility (right). Top, fraction of molecules remaining within 3.4 μm of the trap center for the 100 ms simulation. Center, RMS tracking error of the Kalman filter and ADF algorithms. The dashed curve is the analytical prediction for trapping performance [Equation (2.24)]. Bottom, maximum likelihood parameter estimation using the ADF algorithm. Parameter estimation using the Kalman filter did not converge for any of these cases. Error bars are ± one standard deviation about the mean of the relative difference between the estimated and true parameter values.
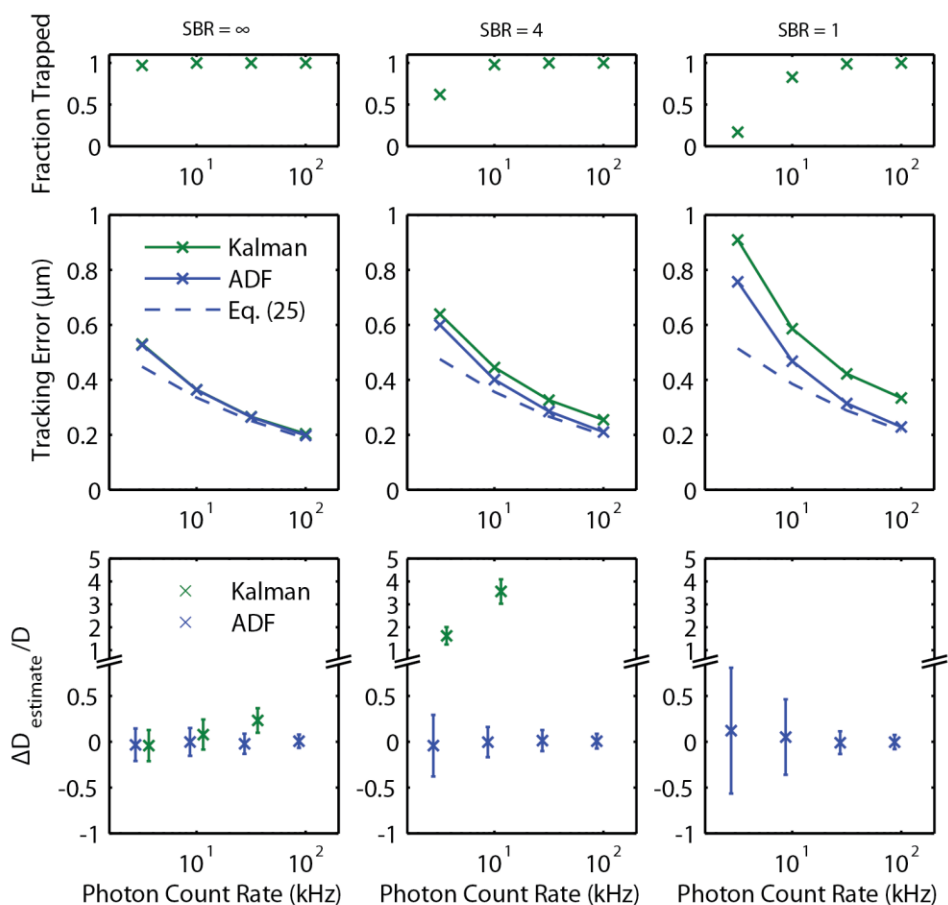
Figure 2-3 Simulated trapping and parameter fitting as a function of photon count rate (not including background photons) and signal-to-background ratio (SBR). Plots are as in Figure 2-2, except that the bottom plots all show diffusion coefficient fitting, and fits were attempted using both the ADF algorithm and the Kalman filter. The parameter fitting results for the two algorithms are offset horizontally for clarity.

Figure 2-2 summarizes the simulation results for varying diffusion coefficient or electrokinetic mobility; Figure 2-3 displays the same information as a function of fluorophore brightness and signal-to-background ratio. Stable trapping is achieved for a wide range of simulated parameters, but is hindered primarily when the diffusion coefficient is high or the photon count rate and signal-to-background ratio are low. As expected, the RMS tracking error of the Kalman filter is uniformly greater than that of

54

the ADF, but the difference is typically small unless the background count rate is significant. Equation (2.24) offers a good approximation of the ADF tracking error, with significant deviations only when molecules are not stably trapped. The derivation of Equation (2.24) assumes that the region of confinement is well sampled by the scan pattern; a significant probability of escape implies that the molecules spend significant time at the edges of the scan pattern, violating this assumption and increasing the tracking error above the analytical estimate. The Kalman filter performs well for tracking when $S > 1$ (such as when the molecule's count rate is 100 kHz), in accordance with Equation (2.26), despite the assumption $S \ll 1$ in the derivation. The primary effect of violation of the $S \ll 1$ approximation is to bias the Kalman filter towards the most recent bin (see Section 2.4), and although this bias worsens as S increases, it is more than compensated by the additional information provided by the larger number of photons.

Maximum likelihood estimates of diffusion coefficient and electrokinetic mobility are plotted in the bottom of Figure 2-2. For high values of the diffusion coefficient, the relative precision of the fit is improved by the increased magnitude of the diffusive motion. Similarly, the relative precision of the fit of the mobility is improved for higher electrokinetic mobility because the motion due to the applied feedback becomes greater relative to diffusion.

Figure 2-3 (bottom) shows maximum likelihood estimates of the diffusion coefficient as a function of the molecular photon count rate, at three values of the signal-to-background ratio (SBR, $\overline{\gamma_s}/\overline{\gamma_b}$). Unsurprisingly, the estimate improves as either

the signal rate or the SBR increase. The strong precision and accuracy of the estimator even when the SBR is 1 highlights the background rejection afforded by the ADF.

We compared our parameter estimation results using the ADF to those derived using the Kalman filter and its associated likelihood function [Equation (2.17)]. For many choices of parameters, the Kalman filter failed to find a reasonable fit (defined by maximum likelihood diffusion coefficient $\geq$ 1500 μm^2/s); the successful cases are plotted in Figure 2-3. (None of the parameter sets plotted in Figure 2-2 resulted in a successful Kalman fit.) Consistent with the derivation in Section 2.4, the Kalman filter performs well in cases where $B \ll S \ll 1$; indeed, its performance is nearly indistinguishable from that of the ADF in the case of zero background and $\overline{\gamma_s}$ < 30 kHz (S < 0.9). Because the Kalman filter treats all photons as real, it vastly overestimates molecular diffusion in the presence of background and hence is extremely sensitive to SBR. Unlike the ADF, the Kalman filter fit worsens as the signal strength increases, to the point that it fails when the photon count rate is 100 kHz ($S \approx 3$), even in the absence of background.

Violations of the assumptions $B \ll S \ll 1$ cause the Kalman filter to report that the particle is moving more than it actually is, due to the treatment of background photons as real when $B > 0$, and due to the bias towards the most recent bin when $S > 0$. When the Kalman filter is supplied with a diffusion coefficient not too far from the true value (e.g. when it is used for tracking), this extraneous motion is largely suppressed by the filter and the tracking error remains low. However, when the Kalman filter is used for parameter fitting, the model inflates the diffusion coefficient to explain

the excess motion. The ADF does not encounter this problem because it can increase

the parameters B or S to account for the detected photons.
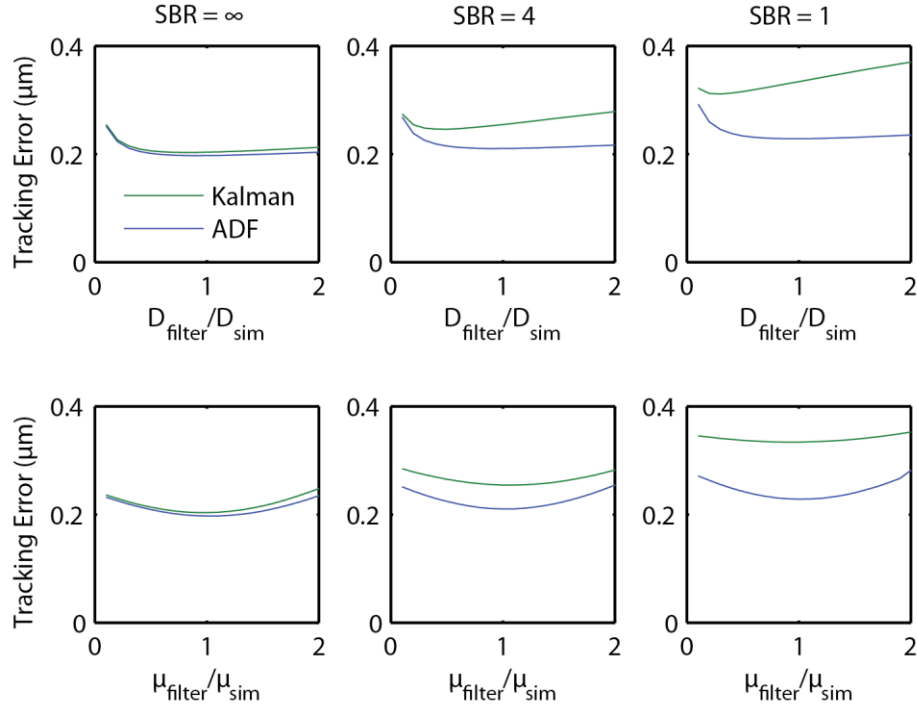
Figure 2-4 Tracking error as a function of filter parameter mismatch, for three values of signal-to-background ratio (SBR) and both algorithms. Fluorophore photon emission rate is 100 kHz for all plots. The ADF performs best with parameter values matching the true values. For nonzero background count rates, the Kalman filter performs better when its assumed diffusion coefficient is less than the true value.

Finally, we calculated the tracking error associated with both filters if the model

parameters were inaccurate (Figure 2-4), at three values of the SBR. Even fairly large

discrepancies in the diffusion coefficient and electrokinetic mobility result in only

modest increases in the tracking error. When $B > 0$, the Kalman filter's tracking error is

minimized when the model diffusion coefficient is set below its true value (or,

equivalently, when the beam width is set to a larger value); this is because the

introduction of background broadens the effective beam width, an effect that is compensated in the ADF but not in the Kalman filter.

2.7   Experiment: trapping single molecules of Alexa 647

We built an ABEL trap that used the Kalman filter derived in Section 2.4 for real-time particle tracking and feedback (see Chapter 3 and [3]). The improved tracking precision of the Kalman filter (Section 2.6) enabled the trap to hold individual molecules of Alexa 647 fluorophore for an average of 1 s per trapping event. Additionally, the ADF algorithm derived in Section 2.3 allowed us to find the maximum likelihood diffusion coefficient and electrokinetic mobility of each molecule (Figure 2-5). The diffusion coefficient averaged over $n = 137$ trapping events was $D = 348 \pm 2$ μm^2/s (s.e.m.), in reasonable agreement with the value 325 μm^2/s we obtained from a different data set [3] and the value 330 μm^2/s measured by FCS [105].

The mean electrokinetic mobility was $\mu = -5.0 \times 10^3$ μm^2/(V s). For a free particle of size much smaller than the Debye screening length, the Einstein-Smoluchowski relation predicts an electrophoretic mobility $\mu = qD/k_BT$, where q is the charge of the particle. From our measurement of D, this relation predicts $\mu = -1.4 \times 10^4$ μm^2/(V s) assuming each molecule bears a single negative charge, significantly different from our data. However, the Einstein-Smoluchowski formula does not take into account electroosmotic flow, the fluid motion induced by application of an electric field to water in a small capillary. This flow velocity depends on details of chemical state of the

channel walls, and is expected to be counter to the direction of the electrophoretic motion in our experiments.

Unexpectedly, the distribution of electrokinetic mobilities was bimodal; the clusters most likely represent distinct charge states of the dye molecule, possibly corresponding to structural isomers. These results demonstrate that the tracking and feedback strategy derived here enable trapping of single fluorescent dyes in water at room temperature. The algorithm reports molecule-by-molecule transport coefficients – information that would be difficult or impossible to measure by other means. Additional experimental results are presented in [3] and Chapter 3.
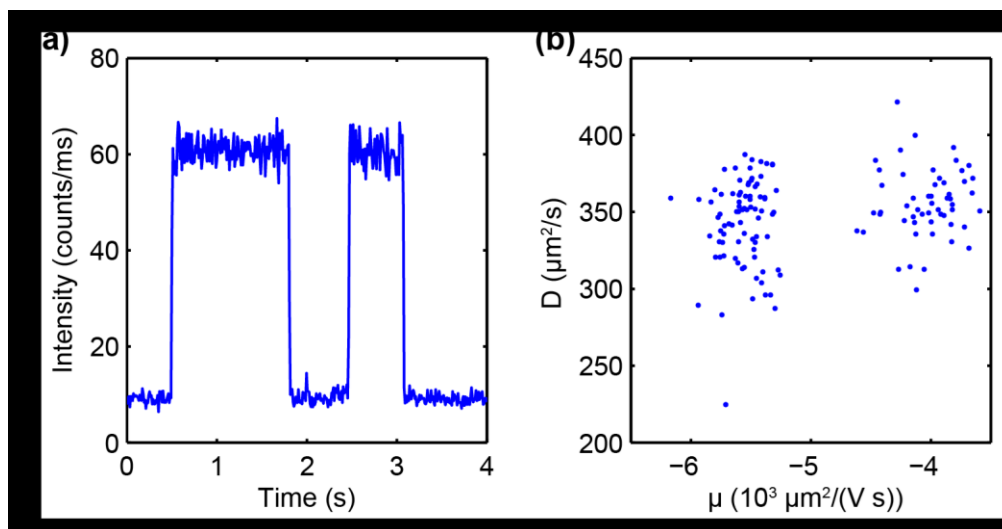
Figure 2-5 Trapping of Alexa 647 molecules in an anti-Brownian electrokinetic trap. (a) Molecular entry or exit induced large step-like changes in fluorescence intensity. Intensity trace binned to 10 ms. (b) The diffusion coefficient D and electrokinetic mobility μ of each trapped molecule was extracted using the ADF algorithm. The population-average diffusion coefficient was $348 \pm 2 \; \mu m^2/s$ (s.e.m.); the electrokinetic mobility revealed the presence of two subpopulations, most likely differing in charge.

2.8 Conclusion

The mathematical framework presented here constitutes a near-optimal approach to track a fluorescent particle undergoing Brownian diffusion plus linear drift in the face of background photons and shot noise. The successive approximations we derive enable real-time particle tracking and offline maximum likelihood estimation of transport parameters, with well-controlled estimates of the uncertainties. This work was motivated by the ABEL trap; our simulation and experimental results demonstrate the algorithms' efficacy in this context. The same treatment also applies to other anti-Brownian traps, such as those functioning by stage motion.

The recursive Bayesian framework derived here is adaptable to other measurement modalities or models of particle motion via modification of the update or prediction equations, respectively. A simple adjustment to the prediction step accounts for the case that the applied feedback is itself stochastic [3]. The case of camera tracking can be handled by treating each pixel as a "laser spot" and applying the update steps corresponding to each of the pixels in a frame simultaneously (instead of applying a prediction step in between, as in the case of scanned laser tracking). Non-Brownian motion is less simple to handle; the treatment offered here could be used as-is, with the understanding that it represents an inexact approximation of the motion as memoryless and Gaussian, or a more specific model could be constructed.

The traditional approach of treating every frame in a particle tracking experiment independently is mathematically equivalent to a model of molecular motion in which the particle is equally likely to move anywhere regardless of its previous

position, so information from recent frames is ignored during the analysis of the current frame. This approach is statistically inefficient if a model of the motion is known. The algorithms we have derived demonstrate how to apply an explicit model of particle motion to get the most from the data collected in a tracking experiment.

3
Electrokinetic trapping at the one nanometer limit

Anti-Brownian Electrokinetic traps (ABEL traps) have been used to trap and study the free-solution dynamics of large protein complexes and long chains of DNA. Small molecules in solution have thus far proved too mobile to trap by any means. Here we explore the ultimate limits on trapping single molecules. We developed a feedback-based ABEL trap in which classical thermal noise is compensated to the maximal extent allowed by quantum measurement noise. We trapped single fluorophores with a molecular weight of < 1 kDa and a hydrodynamic radius of 6.7 Å for longer than one second, in aqueous buffer at room temperature. This achievement represents an 800-fold decrease in the mass of objects trapped in solution, and opens the possibility to trap and manipulate any soluble molecule that can be fluorescently labeled. To illustrate the use of this trap, we studied the binding of unlabeled RecA to fluorescently labeled single-stranded DNA. Binding of RecA induced changes in the DNA diffusion coefficient, electrophoretic mobility, and brightness, all of which were measured simultaneously and on a molecule-by-molecule basis. This device greatly extends the size range of molecules that can be studied by room temperature feedback trapping, and opens the door to further studies of the binding of unmodified proteins to DNA in free solution.

3.1   Introduction

A longstanding challenge in single-molecule spectroscopy has been to observe a small molecule in solution for an extended time, without surface tethering or other mechanical immobilization. Stable observation becomes more difficult as the particle decreases in size, because smaller objects diffuse more quickly, in accordance with the Stokes-Einstein relation. Gold nanoparticles as small as 18 nm in diameter, corresponding to a mass of 35 MDa, have been trapped using laser tweezers [106]. Below this size laser tweezers fail because the trapping force is proportional to the volume of the trapped object. Real-time feedback provides an alternate strategy, and has been used to trap single atoms in vacuum [107]. The Anti-Brownian Electrokinetic trap (ABEL trap) uses feedback to suppress Brownian motion in solution and can confine particles as small as the 800 kDa complex of the chaperonin GroEL [39, 46, 65]. A 104 kDa protein, allophycocyanin, was recently studied in an ABEL trap in which the viscosity was increased with 50% glycerol to slow the Brownian motion [68]. Past attempts to trap small-molecule fluorophores in aqueous solution resulted in transient confinement, but not stable trapping [46]. Small-molecule fluorophores are the tiniest objects that one can conceive of trapping in aqueous solution. If a particular fluorophore can be trapped, then so too can any molecule to which it is attached.

Laser tweezers and the ABEL trap both confine small objects in solution, but the two technologies enable different kinds of measurements. The optical forces of laser tweezers enable precise (sub-nanometer) localization of the trapped object, and permit application of precisely calibrated point forces for the purpose of force spectroscopy

[108]. The ABEL feedback strategy enables trapping of smaller objects, including individual molecules, but tracking imprecision, algorithmic errors, and feedback latency permit residual Brownian motion, typically with an amplitude of several hundred nanometers. The feedback forces in the ABEL trap are applied as body forces to all molecules in the solution, so this trap is not appropriate for force spectroscopy. The ABEL trap is primarily suited to non-perturbative observation of single-molecule dynamics (see Chapter 1 and [1]).

One goal of single-molecule trapping is to study binding interactions in solution which may be perturbed by surface tethering. An obstacle to reaching this goal is that if both species are labeled, at least one must be at a concentration incommensurate with single-molecule fluorescence for dissociation constants greater than ~0.1 nM. An alternative strategy is to detect binding via the influence of an unlabeled molecule on the photophysical or transport properties of a labeled and trapped binding partner. Binding of RecA to DNA has been extensively studied in bulk [109], structurally [110], and at the single-molecule level [111, 112, 113]. Here we report the first observations of changes in transport coefficients of freely diffusing short DNA oligos upon binding of RecA.

The design of our ABEL trap is illustrated in Figure 3-1. The position of an object is tracked in real-time via fluorescence, and electrokinetic feedback is applied via two orthogonal pairs of platinum electrodes to cancel Brownian motion in the plane. Out-of-plane motion is physically restricted by the fused silica walls of the nanofabricated sample cell. When necessary, the walls are chemically passivated to minimize surface

interactions with the analyte. Fully three-dimensional electrokinetic trapping, which avoids problems of surface interactions, has been demonstrated on 0.6 μm polystyrene beads, but not yet for single molecules [114].

Our optical detection scheme uses a scanned laser and a single-photon counting detector, with spatial information derived from the location of the laser at the instant each photon is detected [46, 57]. The position of the laser is specified by a field-programmable gate array (FPGA), similar to the strategy outlined in a recent theoretical article [115]. The key innovation that improves our trap's performance is a statistically rigorous real-time tracking and feedback system, implemented on the FPGA. This system operates at the quantum limit imposed by the finite information carried by each fluorescence photon. The LabVIEW FPGA code is publicly available [116].

Each detected photon specifies the particle's location with a precision limited by the standard deviation of the Gaussian laser spot, measured to be 360 nm. Averaging over many photons improves localization precision, but neglects the motion of the particle between photon detections. A more sophisticated strategy is to construct a "running average" in which recently detected photons are weighted more heavily than those detected earlier. A Kalman filter [102, 103], schematized in the upper left of Figure 3-1, appropriately weights the information from each photon (see Sections 2.4 and 3.4.5 for details) and is simple enough to implement in the FPGA and to run at high speed. Thus the tracking system operates close to the physical limits imposed by diffusion, diffraction, and the finite rate of photon detection events.
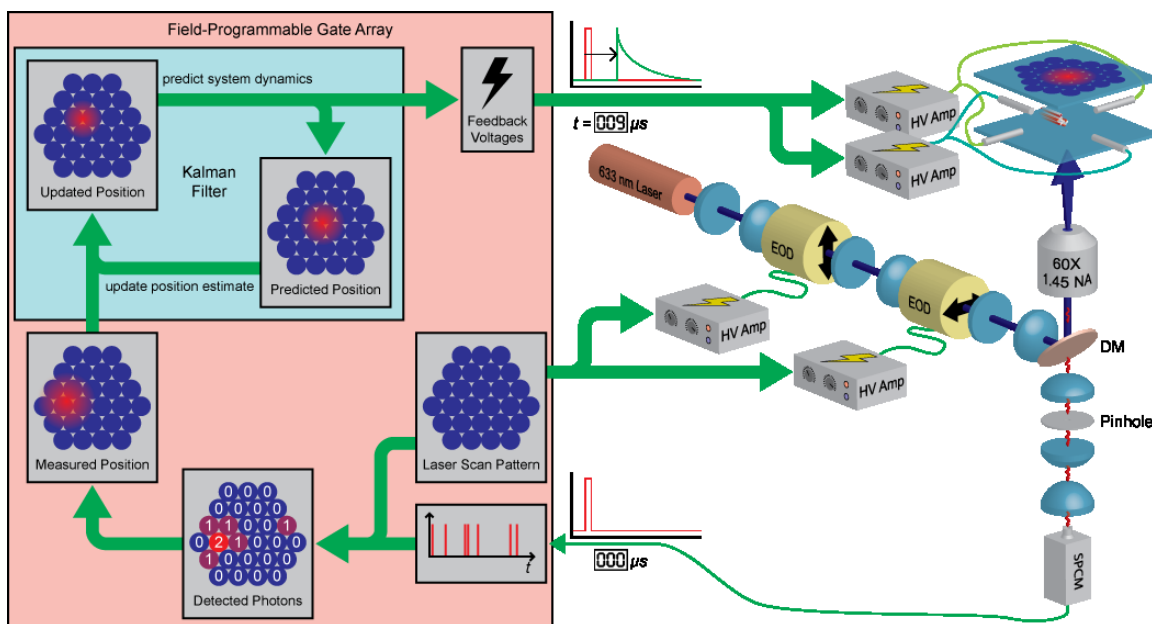
Figure 3-1 Instrumentation. Two electro-optic deflectors (EODs) scanned light from a 633 nm HeNe laser among a set of 27 discrete points with a dwell time of 3.1 μs per point. Fluorescence emitted by a fluorophore in the sample cell (top right) was separated from the illumination by a dichroic mirror (DM) and detected by an avalanche photodiode single-photon counting module (SPCM). A Kalman filter implemented on a field-programmable gate array incorporated the information from each photon detection into a running estimate of the fluorophore position, and generated appropriate feedback voltages that are amplified and applied to the sample cell via four platinum electrodes. The latency of the feedback loop (between photon detection and voltage response) was 9 μs.

3.2 Results

3.2.1 Trapping of single fluorophores

In the absence of feedback, fluorophores of Alexa 647 diffused across the laser scan pattern with an average residence time of 2 ms (Figure 3-2 A, top). When feedback was applied, fluorophores that diffused into the trap were quickly pushed to the trap center and held for an average of 800 ms prior to photoblinking, photobleaching, or escape (Figure 3-2 A, center), corresponding to the collection of an average of 37000 photons per event. Some single fluorophores were trapped for as long as 10 s, yielding as many as 450000 photons. The time-averaged illumination was uniform throughout

66

the region explored by the molecule, so residual molecular motion did not lead to brightness fluctuations. The fluorescence intensity was constant during each event and from one event to the next, and every event ended with a quantal step to background fluorescence, establishing that the trapped species contained only one fluorophore. Molecule-by-molecule analysis of diffusion coefficients (see below) yielded a narrow distribution peaked around 325 μm^2/s, which matched the value obtained in bulk [105] and confirmed that every event corresponded to a free fluorophore. Occasional short-lived positive intensity spikes during trapping events signified the approach of a second fluorophore near the trap; the Brownian motion of the fluorophores was uncorrelated, so after a few milliseconds one diffused away. Segments of dsDNA (30 bp), doubly labeled with Alexa 647 showed two clear photobleaching steps, each equal in intensity to that of a trapped single fluorophore (Figure 3-2 A, bottom), further confirming that the objects trapped in the free dye sample were single fluorophores. Figure 3-2 B shows in red a time-averaged CCD image of a series of trapped single fluorophores. Displayed in blue is the time-averaged laser scan pattern.

To determine the loss mechanisms from the trap, we studied the trapping time of single fluorophores as a function of laser power (Figure 3-2 C). A trapping event was considered to end when the fluorescence dropped to background for longer than 300 μs. The mean trapping time was non-monotonic in laser power, indicating that trapping time was limited by photon statistics and diffusional escape at low power, and by photobleaching or photoblinking at high power. The trap was typically operated

67

under conditions to maximize mean trapping time, in which case rates of diffusional

escape and photoblinking or bleaching were approximately equal.
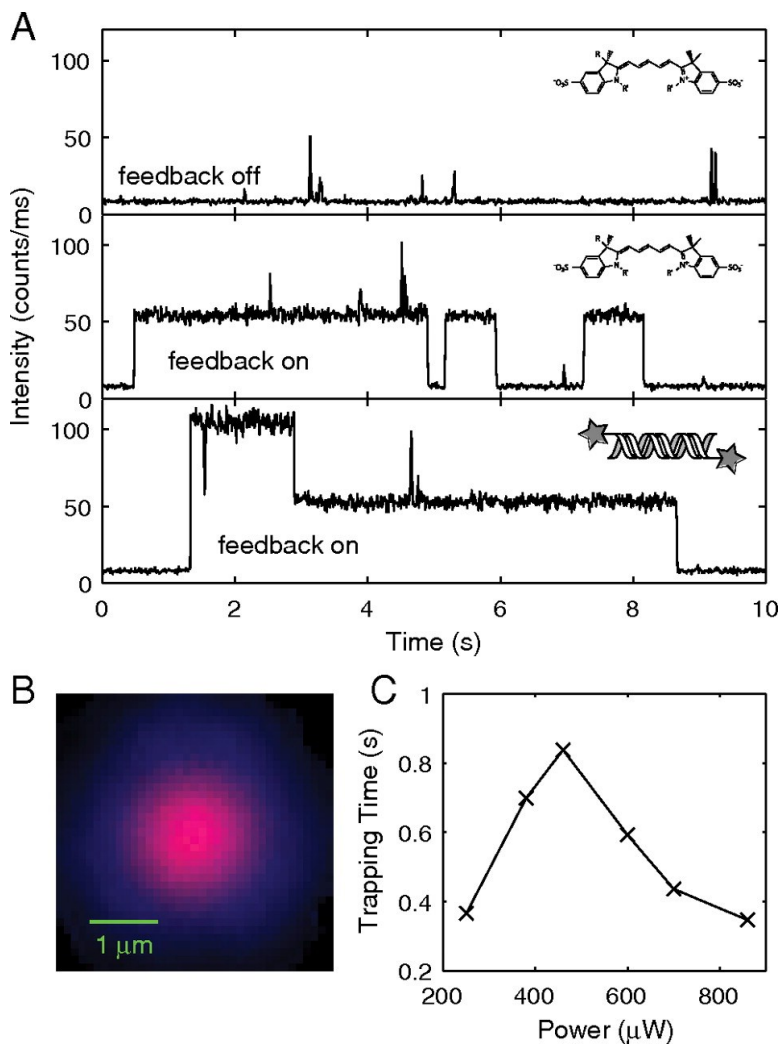
Figure 3-2 Trapped molecules. (A) In the absence of applied feedback, the fluorescence of Alexa 647 molecules (chemical structure inset) showed brief bursts averaging 2 ms in duration (top). When feedback was applied, molecular residence time was greatly enhanced (center). Trapping of 30 bp dsDNA doubly labeled with Alexa 647 showed two-step photobleaching (bottom). In the structure of Alexa 647 (Compound 9 in [117]), R refers to N-hydroxysuccinimide hexan-6-yloate and R′ refers to 3-sulfonatopropyl. (B) Time-averaged image of a series of trapped Alexa 647 molecules (red) merged in software with an image of the laser scan pattern (blue). (C) Mean trapping time as a function of laser power, showing the balance between diffusional escape and photoblinking or bleaching.

Photobleaching rates in the ABEL trap were higher than in typical surface-tethered experiments because high count rates were required to achieve stable feedback. Furthermore, we interpreted every blinking event as the end of a single-molecule trajectory. This procedure contributed to the shorter reported observation time in the ABEL trap compared to surface-tethered experiments where one typically averages over blinks. The distribution of trapping times had a long tail, possibly due to variations in rates of photobleaching and photoblinking caused by variations in the concentration of oxygen and triplet quenchers.

3.2.2 Analysis of photon-by-photon trapping data

The photon-by-photon recording of each trapping event enabled quantitative determination of the spatial trajectory, transport coefficients and photophysical properties of each molecule, with a precision far beyond that of any other single-molecule technique. We developed a maximum-likelihood Assumed Density Filter (ADF) to perform these calculations (see Sections 2.3 and 3.4.6). We applied the ADF to trajectories of single trapped molecules of Alexa 647 to determine the strength and relaxation time of the trap (Figure 3-3 A–B). The fluorophore was tightly constrained to the center of the trap, with an RMS deviation of 416 nm, well within the ~5 μm diameter of the laser scan.
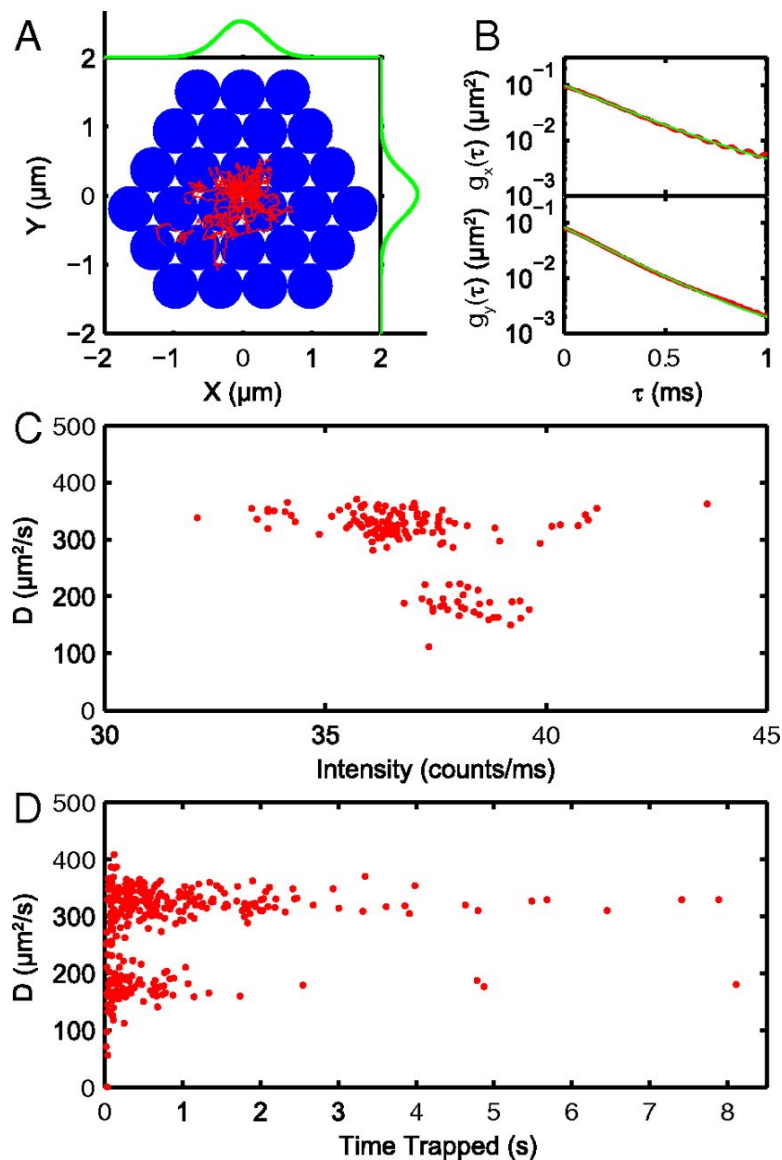
Figure 3-3 Performance of the ABEL trap. (A) First 10 ms of the reconstructed trajectory of a single trapped molecule of Alexa 647 (red), plotted over a cartoon of the 27-point scan pattern (blue). Time-averaged probability densities are plotted along each axis (green). The mean precision with which each point in the trajectory was localized is 240 nm, which is less than the width of the laser spot (360 nm) because the estimate includes information from several photons. The molecule was confined with an RMS deviation of about 416 nm, well within the ~5 μm diameter of the laser scan. From the equipartition theorem, we calculate effective spring constants of 0.022 pN/μm and 0.026 pN/μm in the x and y directions, respectively. (B) Time-autocorrelation of the position of the molecule along each axis (red), with fit to a single exponential (green). Relaxation times are $\tau_x = 290$ μs and $\tau_y = 240$ μs. (C–D) Determination of single-molecule diffusion coefficients. Molecules were trapped from a mixture of free Alexa 647 and 30 nt ssDNA singly labeled with Alexa 647. The fitted diffusion coefficient for each molecule is plotted versus the brightness of the molecule (C) or the duration for which it was trapped (D). The two diffusion peaks have mean values of 178 ± 2 μm^2/s and 325 ± 2 μm^2/s (s.e.m.), corresponding to the ssDNA and free dye species, respectively.

70

To test our ability to measure diffusion coefficients of small objects, we studied a mixture of free Alexa 647 dye and 30 nt ssDNA, singly labeled with Alexa 647. Many single molecules were sequentially trapped until photobleaching. Based on their intensity or trapping time alone, the two species in the sample were indistinguishable, but they were clearly resolved by their diffusion coefficients (Figure 3-3 C–D). From experiments in which only one species was trapped, we associate the lower diffusion coefficient with the DNA species and the greater one with free Alexa 647.

These highly precise measurements of single-molecule diffusion coefficients enable quantitative comparison with bulk measurements and theory. The diffusion coefficient obtained in the ABEL trap for Alexa 647, $D_{AF} = 325 \pm 2~\mu m^2/s$ (s.e.m.), is consistent with the value of 330 $\mu m^2/s$ measured by two-focus fluorescence correlation spectroscopy (FCS) [105]. The diffusion coefficient of the 30-mer ssDNA, $D_{30\text{-}mer} = 178 \pm 2~\mu m^2/s$, matches that predicted by the Zimm model for a polymer in good solvent, 166 $\mu m^2/s$, calculated with persistence length and rise per base taken from laser tweezers experiments [118] and no adjustable parameters (see Section 3.4.7 and [119]).

The diffusion coefficients can be converted to hydrodynamic radii via the Stokes-Einstein relation. The ABEL trap data yielded a population-average radius for Alexa 647 of 6.76 ± 0.03 Å (s.e.m.) and for 30-mer ssDNA of 12.3 ± 0.2 Å. The diffusion coefficient of each single molecule was determined more precisely as trapping time increased (Figure 3-3 D); we calculate a precision of roughly 20 $\mu m^2/(s~\sqrt{Hz})$ in determining D. Thus a single molecule of Alexa 647, trapped for 1 s, yielded an estimate of its hydrodynamic

radius with a precision of 0.5 Å (s.d.). The ability to measure hydrodynamic radii of single molecules in free solution so precisely may be useful for observing subtle conformational shifts.

3.2.3 Detection of molecular interactions

Encouraged by our success in trapping and characterizing single fluorophores and small DNA molecules, we next studied the interaction of ssDNA with *E. coli* RecA, a protein known to form helical filaments on ssDNA in the presence of ATP [109]. The ssDNA sample was 60 nucleotides long, singly labeled at its 5' terminus with Alexa 647. In the absence of RecA, the ssDNA is expected to form a random coil with a contour length of 33.6 nm, a persistence length of 7.5 Å, and a radius of gyration of 27 Å [118]. This length of DNA is sufficient to nucleate a RecA filament containing up to 20 monomers of RecA [120], but vastly shorter than the ~900 nm persistence length of the RecA filament [113]. Binding of RecA is expected to convert the ssDNA from a random coil to a semi-rigid rod with a radius of roughly 4 nm and a rise of 5.1 Å per nucleotide [110], corresponding to a total length of 30.6 nm and a hydrodynamic radius of 10.5 nm (see Section 3.4.7).

Before studying the interaction of RecA with ssDNA in the ABEL trap, we first used conventional FCS to confirm binding of RecA to ssDNA and to study the ensemble-averaged effects of binding upon the diffusion coefficient and fluorescence brightness of the ssDNA. Addition of unlabeled RecA (1 µM) and ATP (1 mM) to a sample of ssDNA induced a 60% drop in the ensemble-averaged diffusion coefficient of the DNA (Figure 3-4 A), and a 40% increase in the average molecular brightness. The decrease in

diffusion coefficient was consistent with a change in geometry from a compact random coil to an extended rod. The increase in brightness upon binding of RecA to fluorescently labeled ssDNA likely reflects changes in the chemical environment of the fluorophore, and is consistent with a previous report in which a different fluorophore was used [121]. RecA in the absence of DNA had no detectable fluorescence. These FCS measurements provided no information on the underlying distributions of single-molecule brightness and diffusion coefficient, and provided no information about the ensemble-averaged or single-molecule values of the electrokinetic mobility.

We next trapped single molecules of the fluorescently labeled ssDNA, first in the absence, and then in the presence of RecA (1 μM) and ATP (1 mM). Each trapped molecule was characterized simultaneously for its brightness, diffusion coefficient, and electrokinetic mobility (Figure 3-4 B–E). These three parameters indicate different aspects of the molecular structure: brightness of the fluorophore is sensitive to the chemical environment at the 5' end of the ssDNA; diffusion coefficient is sensitive to hydrodynamic radius of the entire molecular complex; and electrokinetic mobility is sensitive to both charge and viscous drag. Thus each molecule was characterized with high precision in a multi-dimensional parameter space, allowing facile identification of heterogeneous sub-populations.

In the absence of RecA, we observed a homogeneous population of trapped molecules with diffusion coefficient $113 \pm 4 \ \mu m^2/s$ (s.e.m.), a mobility of $-6.3 \pm 0.1 \times 10^3 \ \mu m^2/(V \ s)$ and a mean molecular brightness of $32.0 \pm 0.2 \times 10^3$ photons/s, which we associate with bare ssDNA. Addition of RecA and ATP led to the

appearance of a second subpopulation with diffusion coefficient of $50 \pm 2\ \mu m^2/s$, mobility of $-3.65 \pm 0.07 \times 10^3\ \mu m^2/(V\ s)$ and a mean molecular brightness of $44.7 \pm 0.3 \times 10^3$ photons/s.
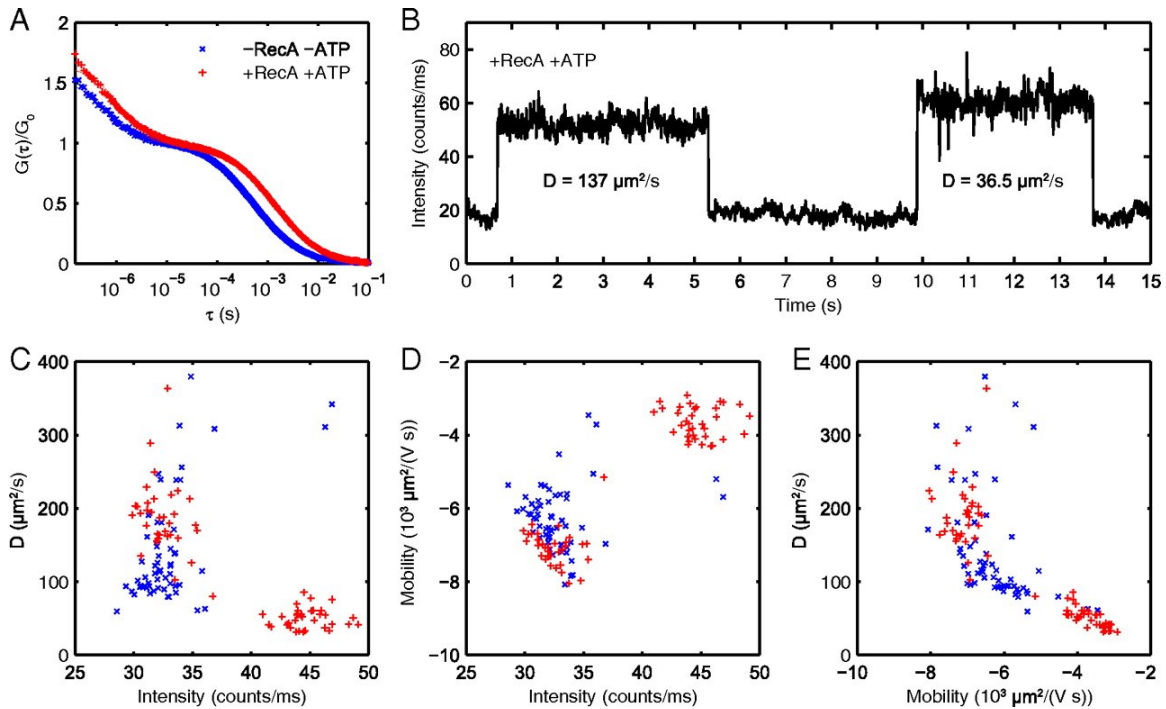
Figure 3-4 RecA binding to single-stranded DNA. (A) Raw FCS data (points) and least-squares fits (lines) for a sample of 60-mer ssDNA labeled with Alexa 647 in the presence or absence of 1 μM RecA and 1 mM ATP. Plots are normalized to the fit value of G_0, which neglects the triplet fraction (see Section 3.4.8 for fit function). The lowering of average diffusion coefficient upon binding of RecA is visible as a longer autocorrelation decay time. (B) Trapping 60-mer ssDNA molecules in the presence of RecA and ATP revealed two species, exemplified by this fluorescence timetrace. The first species, identified as bare ssDNA, was dimmer and had higher diffusion coefficient; the second, identified as RecA nucleoprotein filament, was brighter and diffused more slowly. (C–E), Three-parameter molecular profiling. (×) ssDNA without RecA, (+) ssDNA with RecA and ATP. Plotting the brightness, diffusion coefficient, and electrokinetic mobility of trapped ssDNA molecules reveals that binding of RecA induced changes in all three.

We compared the diffusion coefficients of the bare ssDNA and the nucleoprotein filament to theoretical predictions based on the expected geometries of these compounds. The measured diffusion coefficient of the ssDNA, $113 \pm 4\ \mu m^2/s$, is in good

agreement with the Zimm prediction of 124 μm^2/s for 60-mer ssDNA. The measured diffusion coefficient of the RecA-ssDNA nucleoprotein filaments, $50 \pm 2 \mu m^2$/s, is lower than that of the bare ssDNA, consistent with an increase in hydrodynamic radius upon RecA binding. However, the measured diffusion coefficient is significantly larger than expected from a rigid-rod model of the filament, 21 μm^2/s. Several modifications to the rigid-rod geometry may account for this discrepancy, including: bent or curved nucleoprotein structure (as seen in some electron microscope images [122]), incomplete coverage of the DNA by RecA, or multiple RecA domains separated by floppy dislocations. Distinguishing among these scenarios will require varying conditions such as the length of the DNA template and the RecA concentration. The discrepancy is unlikely to be due to transient dissociation of RecA monomers from the nucleoprotein filament, as transport coefficients were not affected by replacement of ATP with ATPγS, an analog known to reduce the rate of dissociation [123].

The decrease in absolute value mobility upon addition of RecA is consistent with a decrease in net charge or an increase in drag. The change in Stokes drag can be inferred from the change in diffusion coefficient, discussed above, but the relevance of Stokes drag to the electrophoretic mobility depends on the details of the ionic cloud around the complex. In the Hückel regime, in which the particle is much smaller than the Debye length of the buffer, the electrophoretic velocity is determined by a force balance between the Coulombic pull of the field and the Stokes drag on the moving particle. In the Smoluchowski regime, in which the particle is large compared to the Debye length, the electric and shear forces are both localized within the Debye layer

and both grow proportionally to the size of the particle [124]. Thus the electrophoretic mobility is independent of the size of the particle. In the case at hand, the size of the ssDNA-RecA complex is comparable to the Debye length of the buffer, estimated to be 1.5 nm. Thus, the molecule is between the Hückel and Smoluchowski regimes, where theoretical estimates of mobility are difficult. Free-solution electrophoretic mobilities of ssDNA [125] and DNA-protein complexes [126] have been measured and are similar to our single-molecule values, though the buffer composition in these experiments differed from ours, preventing quantitative comparison.

Despite the presence of RecA, many of the trapped molecules remained in the state associated with bare ssDNA. The presence of precisely two clearly resolved peaks in the multidimensional single-molecule distributions indicates highly cooperative binding of RecA to ssDNA, consistent with earlier measurements in which nucleoprotein filament formation was measured as a function of RecA concentration [127].

3.3 Discussion

The new ability to measure simultaneously the diffusion coefficient, electrokinetic mobility, and brightness of each trapped molecule, to high precision, allows species to be distinguished on the basis of size, charge, and photophysical properties, in free solution and in complex mixtures. Unlike fluctuation techniques such as FCS [128] and the photon-counting histogram (PCH) [24], the ABEL trap characterizes individual molecules in isolation, allowing compilation of the full distribution of each measured parameter and enabling multiple parameters to be correlated at the single-

76

molecule level. The long observation times per molecule in the ABEL trap provide significantly more precise information than is obtained from photon burst analysis [129, 130]. Furthermore, the tracking data enables unambiguous separation of transport and photophysical dynamics, which are otherwise conflated in single-point confocal techniques.

Finally, the ABEL trap opens the possibility of observing molecular transitions as they occur; such transitions cannot be resolved in observations of passively diffusing molecules unless they occur on a timescale faster than the diffusion time (~1-10 ms), but may be observed on timescales as long as seconds in the ABEL trap. In the present RecA data we observed occasional transitions indicative of RecA binding to an already trapped molecule of ssDNA; however, these transitions were too infrequent to merit detailed analysis.

In contrast to the ensemble-averaged FCS data, the ABEL trap data clearly discerned hidden heterogeneity in the sample of RecA-ssDNA. The multi-parameter molecule-by-molecule data enabled a quantitative comparison to models of the RecA nucleoprotein filament. These new capabilities are expected to be broadly useful in contexts beyond studying protein-DNA interactions.

Trapping small-molecule fluorophores in aqueous solution is the ultimate size limit of feedback trapping in solution. The median size of human proteins is 375 amino acids [131], corresponding to a diameter of ~4 nm [33]. With previous trapping technology, only the largest of proteins and complexes, with diameter > 15 nm, could be trapped. The present ABEL trap extends this range to include all soluble proteins.

3.4   Methods

3.4.1   Optics

Light from a 633 nm HeNe laser (Thorlabs HRP120) was expanded, passed through a linear polarizer, and guided through two electro-optic deflectors (EODs; ConOptics, Danbury CT). A half-wave Fresnel rhomb (Thorlabs FR600HM) rotated the polarization of the light by 90° between the EODs. A series of relay lenses (Thorlabs) imaged the center of the first EOD onto the second, and the center of the second EOD onto the back aperture of an objective in an inverted microscope (Olympus IX71 with a 60X PlanAPO NA 1.45 oil-immersion objective). Illumination power was set to 250–900 μW depending on the experiment, but was held constant at 430 μW for experiments involving RecA. Fluorescence was collected through the same objective and separated from back-scattered excitation light by a dichroic mirror and a high quality emission filter (Chroma 49006). A tube lens focused the light onto a pinhole with a diameter of 300 μm (corresponding to 5 μm in the sample plane; Edmund Optics NT56-285). The pinhole diameter set the size of the trapping region and was chosen to just encompass the laser scan pattern. The light was then imaged onto an avalanche photodiode single-photon counting module (Perkin Elmer SPCM-AQRH-14). The video of trapped molecules was taken by splitting half of the fluorescence onto an Andor iXon DU-897 back-illuminated EMCCD camera using a 50:50 beam splitter (Thorlabs CM1-BS013). For the FCS experiments, the laser was not scanned and the emission was passed through a 50 μm pinhole.

3.4.2 Device design and fabrication

The ABEL sample cell consisted of a shallow (~600 nm) central trapping region flanked by four deeper (~15 μm) channels etched within a 2.5 mm square piece of fused silica [1]. Fused silica was selected due to its lower autofluorescence relative to glass or PDMS. The dual depth design ensured that the electrical resistance was much larger within the shallow trapping region than elsewhere, focusing the electric field within the trapping region.

The fabrication scheme described here is similar to that of [46], in which the pattern was constructed in two steps of photolithography, corresponding to the deep and shallow channels of the devices, respectively. Modifications to the published protocol include changes to the mask design and use of a ~60 nm chromium etch mask instead of silicon. One hundred devices were fabricated in parallel on a single 4"-diameter, 500 μm-thick fused silica wafer. To enclose the channels, we irreversibly bonded each etched device to the center of a 1" square fused silica cover slip (Esco R425025) using sodium silicate, following a published protocol [76].

We used a cast piece of polydimethyl siloxane (PDMS) to contain excess fluid around the sides of the fused silica device and to hold the feedback electrodes in place. Fluid leakage around the corners of the device allowed pressure equilibration without significant voltage loss. Damp tissue paper placed in an enclosed space with the device alleviated sample evaporation. We used platinum electrodes (Alfa Aesar 45058) to minimize electrochemical products.

79

3.4.3 Electronics

A field-programmable gate array (FPGA; National Instruments PCI-7831R) relayed voltages to two high-voltage amplifiers (Model 7602, Krohn-Hite) to control the beam deflections of the EODs. Concurrently, the FPGA counted and recorded the photons that the APD detected, using their precise arrival times to determine the beam position at the time of emission. The FPGA used a Kalman filter (described below) to calculate feedback voltages, which were amplified by two additional Krohn-Hite high-voltage amplifiers and applied to the trap. The FPGA continually relayed information to a personal computer for storage; this same computer also allowed the operator to set the feedback parameters on the FPGA.

3.4.4 Sample preparation

Chemicals were purchased from VWR unless otherwise noted. 5' C6-linked amino modified 30 nt ssDNA oligonucleotides were custom ordered from IDT and labeled with Alexa 647 NHS-ester (Invitrogen A-20196) according to the manufacturer protocol. Free Alexa 647 NHS-ester was recovered during purification. Devices were cleaned with piranha solution (a highly corrosive 3:1 mixture of concentrated sulfuric acid and 30% hydrogen peroxide). Prior to trapping samples containing RecA, devices were functionalized with polyethylene glycol (Vectabond Reagent SP-1800, Vector Laboratories, and MPEG-SVA-5000, Laysan Bio Inc.), according to manufacturer instruction. All experiments were performed in 10 mM HEPES buffer, pH 7.4, with fluorophore concentrations of ~2 pM. Oxygen was removed from solution using the protocatechuate 3,4-dioxygenase (Sigma-Aldrich P8279) and protocatechuic acid

80

scavenging system as described [132]. Triplet state quenching was achieved using 1 mM

methyl viologen (Sigma-Aldrich 856177) and 1 mM ascorbic acid (Sigma-Aldrich A92902)

[133]. RecA and ATP were purchased (New England Biolabs M0355 and P0756) and

included in indicated samples at 1 μM and 1 mM, respectively. 1 mM MgCl$_2$ was also

included in the samples containing RecA.

3.4.5   Kalman filter feedback algorithm

The Kalman filter (see Section 2.4) is an algorithm that interprets the past record

of detected photons and applied voltages to construct a Gaussian likelihood distribution

for the location of the particle in the present. The estimate for the particle's position

during the ith time bin, given all of the information recorded up to and including the jth

time bin, is characterized by a mean $\hat{\mathbf{x}}_{i|j}$ and variance $\hat{p}_{i|j}$. The filter operates

recursively: to calculate a new estimate, the previous estimate is revised to account for

the most recent observations and the expected motion of the particle.

The number of photons, n_k, detected during the laser's residence at the kth scan

point are tallied and used to "update" the estimate according to

$$\hat{\mathbf{x}}_{k|k} = \frac{w^2 \hat{\mathbf{x}}_{k|k-1} + n_k \hat{p}_{k|k-1} \mathbf{c}_k}{w^2 + n_k \hat{p}_{k|k-1}}$$

$$\hat{p}_{k|k} = \frac{w^2 \hat{p}_{k|k-1}}{w^2 + n_k \hat{p}_{k|k-1}}$$

(3.1)

where $\mathbf{c}_k$ and w are the mean and standard deviation, respectively, of the laser spatial

intensity distribution during bin k. In this way, the new information from photon arrivals

is combined with the previous position estimate, with weighting coefficients determined

by the uncertainty in each. The beam profile and spot positions were measured prior to

trapping experiments by scanning a small bead immobilized on a coverslip through the

scan pattern using a piezo scanning stage (Thorlabs SCXYZ100).

When the laser's residence at the kth spot ends, a new estimate for the location

of the particle is constructed, with mean and variance "predicted" according to

$$\hat{\mathbf{x}}_{k+1|k} = \hat{\mathbf{x}}_{k|k} + \mu \Delta t \mathbf{E}_k$$

$$\hat{p}_{k+1|k} = \hat{p}_{k|k} + 2D\Delta t$$

(3.2)

where μ is the user-estimated electrokinetic mobility, $\mathbf{E}_k$ is the electric field applied

during bin k, D is the user-estimated diffusion constant, and Δt is the duration of the

bin. At the beginning of the experiment, the estimated location of the particle is

initialized at the trap center and the variance in this estimate is set to an arbitrary large

value. The influence of these initial conditions decays after a few tens of microseconds.

The Kalman filter is propagated each time the laser is moved to a new position (every

3.1 μs).

Feedback voltages are calculated according to the equation

$$\mathbf{E}_{k+3} = -\frac{\hat{\mathbf{x}}_{k+3|k}}{\mu \Delta t}$$

(3.3)

where

$$\hat{\mathbf{x}}_{k+3|k} = \hat{\mathbf{x}}_{k+1|k} + \mu \Delta t (\mathbf{E}_{k+1} + \mathbf{E}_{k+2})$$

(3.4)

This formula is used because the update step cannot be calculated immediately, so a

delay of two bin periods is necessary before the feedback is applied to the sample. The

voltage is capped at a maximum magnitude along each dimension (typically 30–50 V) to

avoid nonlinear effects, sample heating, and degradation of the solution.

3.4.6 ADF algorithm

The Kalman filter is an approximation to the optimal tracking strategy: it treats non-Gaussian probability distributions as Gaussian to allow calculations in real time. The ADF algorithm we developed for post-processing is a recursive Bayesian estimator, which correctly handles background photons and Poisson-distributed shot noise (see Section 2.3). An implementation in MATLAB is publicly available [116].

The ADF projects each (posterior) estimate distribution onto a Gaussian shape parameterized by two-dimensional mean $\hat{\mathbf{x}}$ and two-by-two covariance matrix $\hat{\boldsymbol{\Sigma}}$. The "update" equations become

$$\hat{\mathbf{x}}_{k|k} = L_k^{-1} \sum_{m=0}^{\infty} l_m \hat{\boldsymbol{\chi}}_m \tag{3.5}$$

$$\hat{\boldsymbol{\Sigma}}_{k|k} = \left(L_k^{-1} \sum_{m=0}^{\infty} l_m \left(\hat{\boldsymbol{\chi}}_m \hat{\boldsymbol{\chi}}_m^T + \hat{\boldsymbol{\Psi}}_m \right) \right) - \hat{\mathbf{x}}_{k|k} \hat{\mathbf{x}}_{k|k}^T \tag{3.6}$$

where

$$l_m \equiv e^{-B} \sum_{i=\max(n_k-m,0)}^{n_k} \frac{(-1)^{m+i-n_k} B^i S^m}{(n_k-i)!\, i!\, (m+i-n_k)!} \frac{\left| \hat{\boldsymbol{\Psi}}_m \right|^{1/2}}{\left| \hat{\boldsymbol{\chi}}_m \right|^{1/2}}$$

$$\times \exp \left(-\frac{m \left(\hat{\mathbf{x}}_{k|k-1} - \mathbf{c}_k \right)^T \left(m\hat{\boldsymbol{\Sigma}}_{k|k-1} + \mathbf{W} \right)^{-1} \left(\hat{\mathbf{x}}_{k|k-1} - \mathbf{c}_k \right)}{2} \right) \tag{3.7}$$

$$\hat{\boldsymbol{\chi}}_m \equiv \hat{\boldsymbol{\Psi}}_m \left(\hat{\boldsymbol{\Sigma}}_{k|k-1}^{-1} \hat{\mathbf{x}}_{k|k-1} + m\mathbf{W}^{-1} \mathbf{c}_k \right)$$

$$\hat{\boldsymbol{\Psi}}_m \equiv \left(\hat{\boldsymbol{\Sigma}}_{k|k-1}^{-1} + m\mathbf{W}^{-1} \right)^{-1}.$$

B is the average number of background photons detected per spot residence period, S is the expected number of photons detected from a fluorophore positioned at the center of the Gaussian laser spot for an entire spot residence period, $\mathbf{W}$ is the two-by-

two covariance matrix of a Gaussian approximation to the laser spot shape, and other

parameters are as defined previously. All vectors are treated as column vectors, with ^{T}

or $^{-1}$ indicating matrix transposition or inversion, respectively. The likelihood of each

data point is

$$L_k = \sum_{m=0}^{\infty} l_m.$$ (3.8)

The sums converge, and we truncate when the fractional changes due to additional

terms are $< 10^{-6}$.

The "prediction" equations are

$$\hat{\mathbf{x}}_{k+1|k} = \hat{\mathbf{x}}_{k|k} + \mu \Delta t \mathbf{E}_k$$

$$\hat{\mathbf{\Sigma}}_{k+1|k} = \hat{\mathbf{\Sigma}}_{k|k} + 2D\Delta t \mathbf{I} + \nu \mu^2 \Delta t^2 \mathbf{E}_k \mathbf{E}_k^T$$ (3.9)

where $\mathbf{I}$ is the two-by-two identity matrix, ν is the dimensionless ratio between the

variance and the mean square of the effective mobility, and the other parameters are as

defined previously. The effective mobility is treated as a Gaussian random variable to

reflect the observation that molecules do not always respond identically to an applied

voltage, perhaps due to spatial inhomogeneity of the field, or to unconstrained

fluctuations in the vertical position of the particle in the trap and consequent changes in

field strength and drag on the particle.

The overall log-likelihood of the entire data series is

$$\ln(\Lambda) = \sum_{k} \ln(L_k).$$ (3.10)

Maximum-likelihood parameter estimates are found by gradient ascent of this function.

We estimated the electric field strength as the applied voltage divided by the length of the trapping region (30 µm) in all cases.

3.4.7 Diffusion coefficient calculation

Theoretical diffusion coefficients were calculated using the Zimm model presented in [119], specifically equation (4.84)

$$D_G = 0.2030 \frac{k_B T}{\sqrt{6} \eta_s R_g}$$

(3.11)

where η_s is the solvent viscosity and R_g is the radius of gyration. We calculated R_g using $\sqrt{6} R_g = \sqrt{N} b = \sqrt{Lb}$, where b is the effective bond length (twice the persistence length), N is the number of effective bond segments, and L is the total contour length. For single-stranded DNA, we used an effective bond length of 1.5 nm and a contour length of 0.56 nm per nucleotide [118].

To calculate a theoretical diffusion coefficient of RecA bound to ssDNA, we applied the rigid rod model of [134]

$$D_G = k_B T \frac{\ln\left(\frac{L}{d} + \gamma\right)}{3 \pi \eta_s L}$$

(3.12)

where L and d are the rod length and diameter, respectively, and γ is an end-effect correction term. We used a rise per nucleotide of 0.51 nm and a nucleofilament diameter of 4 nm, based on the structure of [110], corresponding to $\gamma = 0.46$.

3.4.8 FCS fits

FCS traces were fit to a 2D diffusion model with triplet state, adapted from [135]

$$G(\tau) = G_0 \frac{1 - F + F \exp\left(-\frac{\tau}{\tau_F}\right)}{1 - F} \frac{1}{1 + \frac{\tau}{\tau_D}} + G_\infty. \qquad (3.13)$$

Nonlinear least-square five-parameter fits were performed using MATLAB.

4
Future directions
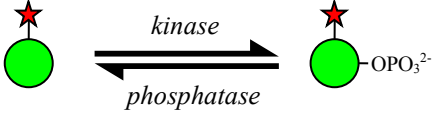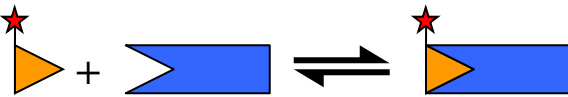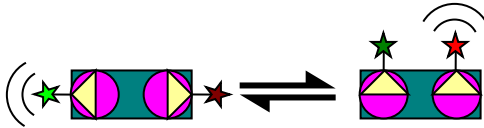
It has recently become possible to trap individual fluorescent biomolecules in aqueous solution by using real-time tracking and active feedback to suppress Brownian motion. Here, we propose areas of investigation in which ABEL trapping of single molecules is likely to lead to significant new insights into biomolecular dynamics. ABEL traps now operate near the information limits imposed by diffraction and shot noise: photons only reach the detector at a finite rate, and each photon carries imperfect information about the location of its source, due to diffractive blurring. The recent generation of traps build on the work of the Mabuchi lab [62] to apply sophisticated statistical filtering, implemented in real-time digital hardware, to squeeze maximal information from every detected photon. These traps act upon this information with negligible delay. Wang and Moerner [6] trapped short fluorescently labeled DNA oligonucelotides, and we recently trapped individual fluorophores (Chapter 3 and [3]). What now? How can we apply these traps to gain new insights into biomolecular dynamics and interactions? What additional improvements in instrumentation or conceptual advances are needed to enable new applications? Here, we present a vision for the future of single-molecule trapping in solution.

4.1   What can we learn from a trapped molecule?

The recent work by Wang and Moerner [6] gives a hint at how the ABEL trap can reveal previously hidden aspects of molecular dynamics. Their system uses the information encoded in the series of photon arrival times and feedback voltages to estimate, in real time, the diffusion coefficient, D, and electrokinetic mobility, μ, of the particle in the trap. The diffusion coefficient measures the strength of the random jiggling, and depends inversely on the hydrodynamic radius and the local viscosity. Time-dependent changes in D could arise from conformational transitions, binding and unbinding with other species in solution, or changes in local viscosity. The electrokinetic mobility reflects the hydrodynamic drag on the particle, but also its charge. Ionization events or covalent modifications might significantly alter μ. There is not currently any satisfactory method to measure changes in D or μ on timescales between milliseconds and minutes, and the new generation of ABEL traps opens this possibility.

A key advantage of the ABEL trap over surface-immobilization techniques is that the ABEL trap avoids possibly perturbative interactions with the surface. Thus, ABEL trapping is well suited to studying processes in which surface interactions may disrupt the dynamics. Processes associated with dynamic changes in transport coefficients are uniquely suited to study via the ABEL trap. We propose several such examples (Table 4:1).

Table 4:1 Free-solution processes amenable to study in the ABEL trap.

Reaction Type		Affected Observables
Protein Folding		E_{FRET}, D, μ, θ
Phosphorylation		μ
Binding		$D, \mu, \theta, I, \tau_{FL}$
Conformational Change		E_{FRET}, D

In each case, several spectroscopic techniques may be used to follow the dynamics. E_{FRET}: FRET efficiency, D: diffusion coefficient, μ: electrophoretic mobility, θ: polarization anisotropy, τ_{FL}: excited state fluorescence lifetime.

4.1.1 Protein folding

The folding process is exquisitely sensitive to weak intramolecular interactions, and unfolded proteins expose sticky hydrophobic residues. Studies of protein folding in molecules bound to a surface are fraught with confounding artifacts. To study protein folding in the ABEL trap, one needs a means to initiate the folding/unfolding transition reversibly. Photoinduced electron transfer [136] or temperature jump [137] experiments are one option, and photogenerated surfactants are another [138]. Alternatively, one could go to partially denaturing conditions, and study the equilibrium fluctuations between folded and unfolded states [139, 140].

One also needs a readout of the folding state of the protein. This readout could come from any combination of time-dependent changes in the transport coefficients (D and μ), or by more conventional single-molecule spectroscopies, such as fluorescence resonance energy transfer (FRET) or excited state lifetime analysis [141]. Ultimately, one would like to study protein folding in the context of chaperonins, to understand how the process functions in a cell. Significant progress toward that goal has already been made by the Moerner lab [69].

4.1.2 Phosphorylation

Addition and removal of phosphate groups from proteins plays a key role in intracellular signaling [142], and misregulation of phosphorylation is often associated with cancer. Due to its medical relevance, many techniques have been developed for measuring ensemble-averaged phosphorylation in cells and in purified proteins. Single-molecule measurements might provide deeper mechanistic understanding of how and when phosphorylation happens, yet there are currently no single-molecule techniques that are sensitive to this process. Ideally, one would like an assay capable of probing a wide range of kinases and substrates, including both wild-type isoforms and oncogenic mutants, in the presence or absence of known and putative kinase inhibitors.

The negative charge associated with a phosphate measurably alters the electrophoretic mobility of some protein targets of phosphorylation [143]. Trapping of fluorescently labeled protein in the presence of unlabeled kinases may reveal the dynamics of the elementary steps of kinase binding, reaction, and unbinding, through their effects on D and μ. To study these processes under quasi-static conditions, one

90

should include phosphatases in the solution to reverse the process. In a few cases, phosphorylation induces conformational changes in the substrate that are large enough to be detected by FRET, in which case that too could be used as a readout.

4.1.3 Transient binding

Many techniques have been developed to measure intermolecular interactions, including various pull-down assays, yeast two-hybrid screens, electrophoretic mobility shift, surface plasmon resonance, and optical techniques based on FRET or colocalization. However, there is a lack of techniques for quantifying weak and/or transient interactions.

Binding of a small fluorescently labeled molecule to a larger unlabeled molecule may measurably alter the mobility and diffusion coefficient of the labeled molecule. These changes are undetectable in surface-immobilized molecules. The ABEL trap is well suited to the study of binding of proteins to fluorescently labeled nucleic acids, for instance. We recently demonstrated this principle by studying the binding of RecA to DNA (Section 3.2.3 and [3]). Similar strategies could be used to study binding of an enzyme to a fluorescently labeled substrate, or weak protein–protein interactions.

4.1.4 Nanoscale physics

The ABEL trap is essentially an implementation of a Maxwell's Demon [144], in that its interaction with a molecule is conditional on the random thermal motion of that molecule. The connection between entropy and the information contained in position measurements is subtle and the subject of much study. Recent experiments with the ABEL trap have begun to probe these questions experimentally [77]. Other researchers

have used ABEL-like traps to study and to control inorganic nanoparticles. Demonstrations include placement of quantum dots for experiments in quantum optics [50, 51, 52], and measurements of the angle-dependent scattering spectrum of gold nanoparticles [92].

The ABEL trap may enable fundamental studies of electrokinetics in confined geometries, an important topic for future nanofluidic systems. For instance, one can ask: Is the mobility of a simple particle really constant, or does it fluctuate rapidly due to fluctuations in the ionic atmosphere around it or transient interactions with the surface? When an electric field is applied, does a particle respond instantaneously, or does the motion take some time to develop? How do mobility and diffusion coefficient depend on the depth of the sample cell, the details of the surface chemistry, and the ionic composition of the medium? While some of these questions could, in principle, be answered in bulk measurements, the ABEL trap enables highly precise measurements in the absence of broadening due to heterogeneity in particle size, shape, or composition.

4.2   Limitations of the ABEL trap

The ABEL trap is not a panacea for the challenges of single-molecule spectroscopy. Several factors constrain the choice of systems to study:

Low concentrations of the fluorescently labeled species, typically a few picomolar, are needed to avoid multiple molecules entering the trapping region simultaneously and confusing the tracking system. Thus the ABEL trap is not suited to studying intermolecular processes in which both species are fluorescent.

92

Low conductivity buffer is important when trapping very small objects (less than 10 nm hydrodynamic diameter). Small objects require large electrokinetic velocities, and hence large feedback voltages, to achieve stable confinement. These conditions lead to heating and deleterious electrochemical byproducts if the buffer is too conductive. Buffer conditions must be optimized for each system.

A bright, photostable fluorophore is essential to achieving high photon count rates and accurate feedback. The requirements on brightness and photostability become more stringent as the trapped particle gets smaller. Brief blinks may interrupt the feedback for enough time for the particle to exit the trap. Trapping of the smallest molecules has only been demonstrated with far-red fluorophores. Trapping using light in other parts of the spectrum, or GFP homologues, will require additional technical development.

Absence of sticking is a challenge in some ABEL trap experiments. Although the molecule is not bound to the surface, fused silica or glass walls constrain the molecule to a thin film, ~800 nm deep. The molecule collides with the confining surfaces hundreds of times per second; without proper consideration of surface chemistry, the molecule may stick.

4.3   How can the ABEL trap be improved?

The ABEL trap will be most useful when additional spectroscopic modalities are layered on top of the optics used for trapping. Then, one could apply the repertoire of

single-molecule spectroscopic techniques to the trapped molecule or complex. Here are some features we expect the next generation of ABEL traps to include.

4.3.1   FRET

Energy transfer provides a sensitive probe of separation between a donor and acceptor fluorophore. To implement FRET analysis, one would use two spectrally distinct detectors; photons from both would be used for tracking and feedback, while the two channels would be considered separately for measurements of time-dependent FRET. We expect FRET to be most useful for intramolecular distance measurements, e.g., of protein folding or conformational transitions, or of assembly and folding of DNA nanostructures.

4.3.2   Polarization and lifetime analysis

Photons carry information about their source in their polarization and precise arrival time at the detector. Polarization indicates the orientation of the transition dipole in the emitter at the moment of emission. For small objects, one may use polarization anisotropy to estimate the molecular tumbling time, which depends sensitively on the hydrodynamic radius ($t \propto r^3$), while for larger objects the polarization fluctuations directly yield this information. Excited-state lifetime may be probed by illumination with a high-repetition-rate pulsed laser. The lifetime provides information on the local rigidity of the environment around the chromophore, and on nonradiative decay pathways.

4.3.3 Rapid mixing and sample introduction

A key challenge in current implementations of the ABEL trap is the ~30 min required for sample introduction. This delay limits studies to quasi-static processes, or to processes that can be triggered by a laser flash. Ideally, one would like to change buffer conditions or to introduce additional components while maintaining a single molecule in the trap. One could then probe dynamic responses to changing conditions. One can also envision an ABEL trap as an analytical component on the end of a sample preparation and fractionation apparatus, just as ion traps are used in mass spectrometry. One might like to analyze molecules directly from a cell, or coming off a microfabricated capillary electrophoresis channel. These applications will require designs that integrate the ABEL trap sample cell with other micro- and nanofluidic components.

4.4 The future of single-molecule studies in nanostructures

The ABEL trap is just one of several technologies under development to facilitate studies on single molecules in free solution [145]. Significant information can be obtained by confining molecules between parallel walls [146], or in thin capillaries [147], lipid vesicles [148], nanofabricated zero-mode waveguides [149] and cavities [22], or water-in-oil hydrosomes [150]. These devices achieve confinement through purely mechanical means, with the attendant decrease in complexity relative to the ABEL trap, but also a loss of high-resolution electrokinetic data.

There are still many unexplored options at the nexus of nanofabrication and single-molecule biophysics that will enable increased insight into the dynamics and interactions of biological molecules. In his treatise on the *Theory of Heat*, Maxwell wrote, "If we conceive a being whose faculties are so sharpened that he can follow every molecule in its course, such a being… would be able to do what is at present impossible to us." [144] In the coming years, we expect many more reports of experiments Maxwell would have thought impossible.

Part II

Euler buckling and

nonlinear kinking of DNA

<div align="right">

5

</div>

Introduction and background

In isolation, double-stranded DNA is one of the stiffest biopolymers. Cells and viruses employ extensive protein machinery to overcome this stiffness and bend, twist, and loop DNA to accomplish tasks such as storage, recombination, and genetic regulation. The mechanical properties of DNA are of fundamental importance to the mechanism and thermodynamics of these processes. Numerous experiments have elucidated the properties of DNA molecules under tension, but the compressive force regime has proven harder to study experimentally, despite its direct relevance to DNA bending and looping. To tackle this challenge, I developed a new tool, a "molecular vise", to apply compressive forces to short (sub-persistence length) DNA strands. In this chapter, I review past work on DNA bending and elasticity.

5.1   Theoretical overview

5.1.1   The wormlike chain model

On long distance scales, duplex DNA is well described by the wormlike chain (WLC) model [151], in which the bending energy is proportional to the squared curvature,

$$U = \int_0^h \frac{1}{2} \kappa \left(\frac{\partial \theta}{\partial s} \right)^2 ds, \tag{5.1}$$

where U is the total energy, κ is the bending modulus, h is the total contour length, and θ is the angle of the polymer as a function of the distance s along it. The persistence length, P, is the characteristic length over which the polymer's angle is retained, and is related to the bending modulus by

$$P = \frac{\kappa}{k_b T}.$$ (5.2)

Values for the persistence length of duplex DNA under roughly physiological conditions range from 44–55 nm [152, 153].

5.1.2 Euler buckling

Euler buckling is the spontaneous bending of an elastic rod as a result of applied compressive stress. Though Euler buckling is typically used to describe failure modes of macroscopic rods, the WLC model suggests that the same phenomenon should occur when sufficient compression is applied to sub-persistence length polymers, including DNA. The critical force at which buckling occurs is

$$F_{buckle} \geq \frac{\pi^2 \kappa}{h^2}.$$ (5.3)

When the applied compressive force is less than this value, the rod can successfully support the load without bending. Greater force causes the rod to buckle spontaneously.

DNA held in a molecular vise (see Chapter 6) experiences approximately constant force, but may be of variable length. It is therefore convenient to consider the buckling length at constant force

$$h_{buckle} \geq \pi \sqrt{\frac{\kappa}{F}}.$$ (5.4)

Rods shorter than this length can support the compression; rods longer cannot and instead adopt bent conformations.

5.1.3 Beyond the wormlike chain

The harmonic, symmetric energy landscape of Equation (5.1), plotted in blue in Figure 5-1, is just one possible form for the Hamiltonian. An energy function with minimum at nonzero curvature, such as the one plotted in magenta, produces an intrinsically curved polymer. A polymer with the anharmonic energy curve shown in yellow behaves identically to the harmonic case for small average curvature, but for larger average curvature subdivides into regions of higher and lower curvature, represented by the two marked points, in order to minimize the total energy. The regions of high curvature are denoted "kinks", so the yellow energy landscape is described as "kinkable". More exotic energy landscapes might be characterized by both intrinsic curvature and asymmetric anharmonicity. In the case of DNA, these energy landscapes are also likely to depend on sequence.

It is important to differentiate between the kinking exhibited by the yellow energy landscape and the more common phenomenon of Euler buckling. Kinking involves the formation of distinct regions of qualitatively different curvature as a consequence of an anharmonic energy landscape. Buckling occurs even for a purely harmonic energy landscape and produces a more even distribution of curvature along the length of the rod.
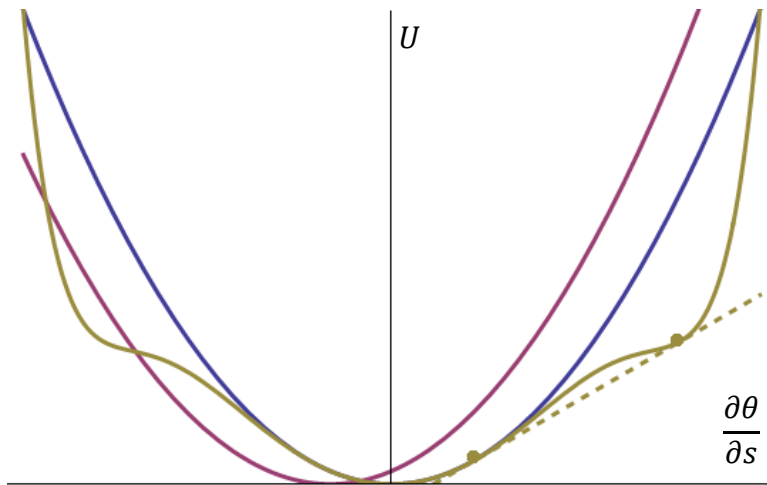
Figure 5-1 Energy landscapes, including harmonic/WLC (blue), intrinsically curved (magenta), and kinkable (yellow).

The common drinking straw provides a macroscopic illustration of both buckling and kinking. If one applies a steadily increasing compressive force to the two ends of the straw, the straw will start out rigidly straight until the force reaches a critical value, at which point it will buckle, bending slightly along its entire length. When the force increases past a second critical value (not much greater than the first for a typical drinking straw), a sharp kink will form at the center of the straw, with low curvature elsewhere. Sample conformations of buckled and kinked rods are shown in Figure 5-2.

In 1975, Francis Crick suggested a structural conformation that double-stranded DNA might adopt in order to form sharp kinks [154]. Others have suggested that DNA kinking might arise from local melting of the helical structure, producing single-stranded "bubbles" of increased flexibility [155]. Experimental data regarding these hypotheses have been sparse and inconsistent.

101
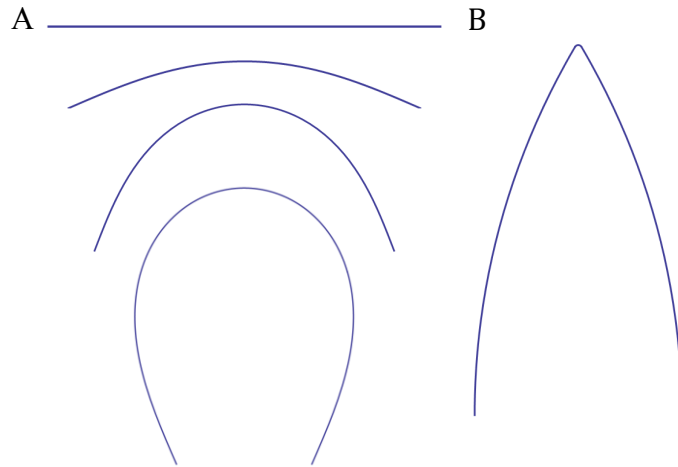
Figure 5-2 Conformations of buckled and kinked rods. (A) Euler buckling distributes curvature throughout the rod. (B) Kinking concentrates curvature in a small region.

5.2 Significance in biology and engineering

DNA flexibility is noteworthy not just as a test of the predictions of polymer physics, but principally because of its relevance to the performance of biological and engineered systems. Processes that depend critically on DNA flexibility include genome packaging, recombination, and gene expression. A deeper understanding of DNA's mechanical properties may also inform the design of functional DNA nanotechnology.

Cells and viruses must overpower the intrinsic stiffness of DNA to package their genomes efficiently. The longest human chromosome has contour length 8.4 cm, corresponding to an RMS end-to-end distance of 90 μm in free solution, but is confined to a cell nucleus ~6 μm in diameter. Eukaryotes compress their DNA by wrapping it around nucleosomes spaced every ~200 bp [156]. Within each nucleosome, 147 bp of DNA encircle a histone octomer 1.67 times, resulting in an average curvature of 4.5°/bp within the central region of the DNA [157]. The crystal structure is not uniformly bent,

but includes three distinct kinks in which the chain bends ~20° from one base pair to the next, in addition to moderate curvature elsewhere. The WLC model suggests that the presence of these kinks should significantly increase the overall DNA bending energy, even after accounting for the relaxation of the curvature in the rest of the sequence. A kinkable model of DNA bending, on the other hand, might assign a *lower* overall bending energy to the kinked structure relative to the evenly curved one (see Section 5.1.3). The detailed energetics of DNA bending therefore relate directly to our understanding of DNA packing.

Nucleosomes not only package DNA for storage, but also restrict its accessibility to transcription factors and other interaction partners [158]. Flexible DNA sequences favor nucleosome binding [159, 160], influencing the transcription of nearby regions. Similarly, epigenetic modulation of gene expression, such as that caused by cytosine methylation, may result from altered flexibility of modified regions [161].

Protein-bound DNA is bent in numerous crystal structures [162]. The structures portray a variety of bent DNA conformations, and in many cases the bending is intrinsic to the function of the complex. In some structures, such as that of the catabolite activator protein [163], the DNA is sharply kinked at specific loci, much as it is in the nucleosome. In other complexes, such as the MATa1/α2 homeodomain [164], the curvature is distributed evenly across the strand. Kinks are found more frequently at certain base-pair steps than others, generally favoring pyrimidine-purine steps. This preference likely contributes to sequence specificity; the restriction endonuclease *Eco*RV, for example, kinks its cognate DNA by 50° but does not deform non-cognate

sequences [165]. Though protein contacts undoubtedly strongly impact the conformation of bound DNA, it is also clear that the DNA itself specifies aspects of its own bending, and studies of the flexibility of isolated DNA help to distinguish those influences.

DNA looping occurs whenever multiple sites on the same strand of DNA are forced to be physically near each other. Unlike bent protein-bound DNA, DNA loops may form in the absence of intimate intermolecular contacts in the curved region and so are more likely to reflect the mechanical properties of isolated DNA. A common cause of DNA looping is the binding of a genetic regulatory element to multiple recognition sites, an occurrence that reduces transcriptional noise and facilitates cooperative gene regulation [166]. The propensity of the DNA between the sites to form a loop influences the binding of the regulatory factor and hence the level of gene expression, as has been demonstrated through experiments varying the length of DNA between *lac* repressor binding sites [167]. Similar considerations apply to DNA recombination when the two sites being exchanged are on the same strand [168, 169].

The 30-year-old field of DNA nanotechnology exploits the convenience and desirable engineering properties of DNA to construct human-designed structures [170]. New fabrication strategies such as modular three-dimensional designs facilitate the construction of increasingly sophisticated assemblies [171]. The ability to harness DNA hybridization to impart structural changes promises to bring these designs to life and power active nanomachinery [172]. Much as structural engineers must understand the

mechanical properties of their building materials, DNA nanotechnologists must consider the consequences of DNA's mechanical properties in their designs.

5.3 Experimental approaches

A wide variety of experimental techniques have been applied to characterize DNA flexibility. This section provides background and perspective on those techniques. Due to the enormous size of this literature, I have frequently elected to cite contemporary reviews; primary sources can be found referenced within them.

5.3.1 Early efforts

Among the earliest experiments performed to measure DNA flexibility were hydrodynamic experiments, including measurements of DNA's intrinsic viscosity or of its sedimentation coefficient, as well as light-scattering experiments. Interpretation of results was complicated by sample polydispersity, particularly for samples prepared by sonication, and by the unknown influence of excluded-volume effects. Despite these concerns, the persistence length in moderate salt (~0.2 M NaCl) was estimated to be 90 ± 20 nm and 60 ± 10 nm from light-scattering and hydrodynamic experiments, respectively [173].

One of the most powerful early techniques for probing DNA flexibility was transient electric birefringence (TEB), in which a pulsed electric field was applied to DNA molecules in solution. The partial alignment of the DNA with the applied field produced measurable optical birefringence, whose decay time following the cessation of the pulse was sensitive to molecular conformation. TEB experiments established a persistence

length of ~50 ± 5 nm for buffers containing at least 1 mM NaCl, with a similar value at MgCl$_2$ concentrations of at least 0.08 mM [174]. Experiments of this era overcame the prior issue of sample polydispersity by borrowing techniques from molecular biology, including preparation and purification of DNA plasmids, site-specific endonuclease cleavage, and sample validation by sequencing. The uncertain influence of excluded-volume interactions was minimized through the use of shorter sequences. Updated light-scattering experiments taking advantage of these insights found a persistence length of ~45 nm in 0.2 M NaCl [175].

5.3.2   Solution cyclization

One clever experiment to measure DNA's flexibility consisted of constructing linear DNA polymers of specific lengths with complementary sticky ends and comparing their rate of intramolecular cyclization to their rate of intermolecular linking following addition of ligase [176]. Reaction products were distinguished from each other and from starting materials through gel electrophoresis. In this way, the effective concentration of one end of the DNA polymer at the position of the other end, denoted the "j-factor", was measured. Decades of cyclization measurements for a wide range of DNA lengths almost unanimously agreed with the WLC model, with a consensus persistence length of ~46.5 nm [177].

Cyclization experiments test the predictions of the WLC model with great sensitivity because they probe extreme conformations. Consequently, the predicted value of the j-factor differs between kinkable and non-kinkable models of DNA elasticity, at least for short sequences [178]. Two papers by Cloutier and Widom measured

anomalously large j-factors for short DNA sequences, suggesting that kinking or other corrections to the WLC model might be required to explain the high apparent flexibility of short DNAs [179, 180]; however, a follow-up study concluded that their experimental protocol had violated a necessary assumption of their assay, and found near-perfect agreement with the WLC model when the condition was satisfied [181]. Another group explicitly validated the necessary assay conditions but still found anomalously high flexibility for one sequence at elevated temperature [182]. Their results were consistent with a model of increased flexibility due to local melting, and the authors used the fit to estimate the flexibility of the melted regions.

Solution cyclization was recently reconstituted at the single-molecule level [183]. Extended observation of individual strands was permitted by either surface tethering or vesicle encapsulation. The conformation of the strands was monitored by FRET between dyes appended to the sticky ends, avoiding the need for ligase. The authors found significantly enhanced flexibility among the short sequences they tested, relative to the WLC prediction. Additionally, the j-factors varied only weakly with length, but greatly with sequence. The authors did not offer a theoretical explanation for their results.

5.3.3 Force extension

Application of force to DNA enables direct control over its conformation, permitting examination of non-equilibrium states and potentially facilitating a more direct comparison with theory. In a typical experiment, a single DNA molecule is stretched between an anchor and a force sensor/applicator. Methods to apply and measure force include flow, optical or magnetic tweezers, and atomic force microscopy

107

(AFM). The force can be measured as a function of the extension ("position-clamp"), or vice versa ("force-clamp"). Double-stranded DNA force-extension curves measured in this way have agreed with the WLC model at forces up to 10 pN; higher forces stretched the DNA beyond its B-form contour length [184]. Even higher forces (150 pN) induced the DNA to melt. Results for single-stranded DNA were better fit by a freely jointed model.

Although the force-extension results generally support the WLC model for double-stranded DNA, it is important to remember that the DNA in the assay is under tension and hence has reduced curvature relative to the thermal distribution. Force stretching experiments are therefore most sensitive to the low-angle bending energy, and would not be expected to differ under typical models of kinkability [178].

5.3.4 Conformational imaging

An intuitive way to measure DNA bending is to image it directly. Traditional structural techniques such as X-ray crystallography or NMR are not well suited to measuring flexibility because they measure the average molecular conformation. A more appropriate technique is cryogenic electron microscopy (cryo-EM), in which samples are loaded on an EM grid, vitrified (cooled rapidly to avoid ice formation) through submergence in liquid ethane, and imaged on an electron microscope. 3D shapes can be reconstructed through alignment of images taken from different angles. Two cryo-EM experiments on DNA minicircles did not find evidence of kinking unless the circles included single-stranded gap regions [185, 186].

Other techniques image molecules immobilized by surface adhesion. In principle, the distribution of bending angles in the images directly corresponds to the bending energy function. The earliest studies of this type recorded electron micrographs from DNA bound to an EM grid, and found reasonable agreement with the WLC model [187]. Later studies used AFM to image DNA deposited on atomically flat mica and blown dry, again finding good agreement with the WLC [188] and further extracting sequence-dependent intrinsic curvature and flexibility from the results [189, 190]. A higher-resolution AFM study found higher flexibility of DNA at short length scales than the WLC prediction and invoked a new Hamiltonian, in which the energy varies with the absolute value of the bending angle (rather than its square), to explain the results [191]. Experiments on surface-adhered DNA depend critically on the assumption that the adhered DNA re-equilibrates on the surface, so that the 2D conformation reflects a thermal distribution and not a kinetically trapped projection of the free-solution thermal distribution. Other concerns specific to AFM include the impact of the drying process on the DNA conformation and the effect of the probe tip on the sample.

The ABEL trap (Part I) and other feedback traps provide an alternative strategy for imaging molecular conformation directly, in solution, at room temperature. In one experiment, individual molecules of λ-DNA were imaged for 9–18 s, facilitating a detailed analysis of their conformational fluctuations [7, 8]. An intercalating fluorescent dye permitted the DNA to be visualized, though it may have also perturbed the DNA's mechanical properties. Anti-Brownian trapping confers the advantage of visualizing not

only the static conformational distribution, but also the dynamics of conformational change.

5.3.5 Conformational inference

A number of techniques have been devised to infer the conformation of DNA while avoiding the artifacts and pitfalls associated with the direct conformational imaging methods. The early hydrodynamic, light-scattering, and electric birefringence techniques (Section 5.3.1) were of this type. A more recent technique exploited the conformational sensitivity of DNA mobility in native polyacrylamide gel electrophoresis (PAGE), and was particularly useful for identifying intrinsically curved sequences [192]. Electrophoretic mobility analyses and cyclization assays (Section 5.3.2) are each sensitive both to static curvature and to flexibility of the DNA sequence being examined, but cyclization is more sensitive to flexibility [193], and has the additional advantage of a well-established theoretical description. In contrast, the intricate interactions of DNA with the gel matrix that give rise to gel mobility shifts have eluded precise theoretical description.

Many conformational inference techniques take advantage of appended probes sensitive to some aspect of the DNA shape. Typically, the ends of a short piece of DNA are labeled with two probes, and the distance between the probes is measured spectroscopically. Specific techniques include electron paramagnetic resonance (EPR) between electron spin labels [194], FRET between fluorescent dyes [195, 196, 197], and small-angle X-ray scattering (SAXS) between gold nanoparticles [198, 199]. Results from these experiments have in some cases supported the WLC model [194, 199] and in

others found enhanced flexibility at short length scales [197, 198]. Caveats of these techniques include the uncertain influence of the probes on the DNA conformation (especially in SAXS experiments using gold nanoparticles), the contribution of the probe linkers to the measured flexibility, and theoretical uncertainty in the extraction of a physical distance from the raw spectroscopic measurement.

5.3.6 DNA-based technologies

Recently, DNA nanostructures sensitive to flexibility and bending have been synthesized. Typically, the structures physically constrain the available conformations such that bent conformations are energetically favored. The molecular vise (Chapter 6), which redirects base-pairing forces to promote bending, is a member of this experimental class. In an earlier experiment, the Liphardt lab hybridized a closed ring of single-stranded DNA with a shorter complementary sequence, producing a double-helix with a single-stranded region stretched between its ends [200]. The stretched single-stranded DNA imparted a compressive force on the duplex, possibly sufficient to induce Euler buckling. The conformation was inferred from FRET between two dyes within the single-stranded region. The Zocchi group used the same structure without FRET labels, instead deducing the bending energy from the melting temperature of the complexes [201].

In a separate experiment, the Zocchi group designed two DNA oligonucleotides, *A* and *B*, such that *A* was longer than *B*, and *B* was complementary to the two ends of *A* [202, 203]. Binding of a single *B* strand to the two ends of a single *A* strand produced a "monomer" consisting of a nicked double helix with a single-stranded region stretched

between the ends of the nicked strand. Alternatively, two *B* strands hybridizing across the ends of two *A* strands formed a four-strand "dimer" in which the nicked duplex regions did not experience significant compressive stress. Monomers and dimers were separated and quantified by electrophoresis (avoiding the need for appended fluorophores), and the equilibrium between them used to estimate the bending energy in the monomers. Unfortunately, this design unavoidably required the presence of a nick within the duplex, and so could not probe bending of intact double-stranded DNA.

6

Molecular vises for studies of DNA flexibility

The biological relevance and inconsistent experimental results of DNA bending on short length scales inspired us to envision new methods to study bending of small pieces of DNA. This capability would aid in the quantitative understanding of DNA bending, helping us understand the energetics of genome storage, genetic recombination, mismatch repair, and transcriptional regulation [169, 177, 204]. One would like to know how the bending energy depends on curvature under physiological conditions: at high curvature, does the DNA bend smoothly, or does it kink like a drinking straw?

Furthermore, when viewed up close, DNA is not a monolithic material. Intrinsic curvature [205] and linear [206] and nonlinear bending moduli depend on the underlying sequence, and are additionally affected by interactions with small molecules (e.g. ions and drugs) and by chemical modifications (e.g. mismatches, epigenetic marks, and damage). These aspects of DNA mechanics are likely to influence protein binding and DNA packaging, yet are only accessible in measurements on very short pieces of DNA. Here we present a simple molecular platform for studying these phenomena in a quantitative way. We identify an ionic strength-induced transition between linear elastic bending and nonlinear "kinking", and we study the effect of single-nucleotide

mismatches on DNA bending. Our data support a simple model of linear elastic bending, with kinking facilitated by local melting of the duplex.

6.1 Molecular vise design and predicted behavior

6.1.1 Assay design

Our "molecular vise" DNA nanostructures (Figure 6-1) used the free energy of hybridization, rather than thermal fluctuations, to drive bending of a distinct, short segment of DNA. The structures consisted of a hairpin with a loop of length 30–50 nt and a stem of length 49 bp. The loop sequences were designed to minimize secondary structure as predicted by M-fold [207]. In the stem the 39 bp adjacent to the loop were all A-T base pairs, to maintain an approximately constant unzipping force. A pair of fluorescent dyes, Cy3B and Alexa Fluor 647, were attached to the nucleotides at the junction of the loop and the stem. The efficiency of FRET between the dyes reported the degree of unzipping of the stem. Details on the synthesis of the assemblies are in Section 6.5.1; sequences are listed in Section 6.5.6.

The hairpins were divided into aliquots and hybridized with oligonucleotides of variable length, complementary to the apex of the loop. We called the resulting double-stranded segment of the loop the "target strand". All target strands contained entirely G-C nucleotides beyond the central 18 nt, to ensure robust hybridization of the target strand and to avoid fraying at its ends. We varied the loop length, L, and the target strand length, h, and we recorded the FRET efficiency, E_L^h, as a function of both parameters.
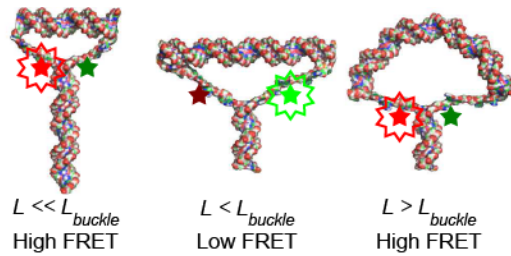
Figure 6-1 Possible conformations of a molecular vise. The base-pairing force in the hairpin stem (composed of all A-T base pairs) imparted a roughly constant compressive force on the ends of the target strand (top duplex). When the target strand was shorter than the buckling length (left and center images), it withstood the compressive force and remained rigid. The dye separation increased as the target strand grew longer, resulting in a decrease of FRET efficiency. Past the buckling transition (right image), the target strand bent under the compressive force and the FRET efficiency recovered. Molecular cartoons were generated using Nucleic Acid Builder [208] and PyMOL [209].

6.1.2 Continuum mechanics of molecular vises

Figure 6-1 illustrates plausible conformations of the molecular vise for varying target strand lengths at fixed loop length. Short target strands did not significantly stretch the loop: the stem remained fully zipped and the FRET was high. When the length of the target strand exceeded approximately half the contour length of the loop, the single-stranded regions became taut, the stem began to unzip, and the FRET decreased. The tension in the single-stranded regions led to a compressive force on the target strand. Due to the 100% A-T composition of the top of the stem, the compressive force was nearly constant, independent of the extent of unzipping. Laser tweezers experiments have measured the A-T unzipping force to be 9 pN [210].

When the target strand reached a critical length, it could no longer support the 9 pN compressive load. The target strand then became bent, a phenomenon called Euler buckling. Further increases in the contour length of the target strand led to a *decrease* in its end-to-end separation, and an *increase* in FRET. Thus we expected buckling of the

target strand to manifest as a minimum in the plot of FRET efficiency vs. length of the target strand.

We can use the results of Section 5.1.2 to predict the length of the target strand at the Euler buckling transition. Let us describe the target strand as a straight elastic rod. For this estimate we neglect thermal fluctuations because the target strand is much shorter than the persistence length. The Euler buckling force for a straight elastic rod of length h is

$$F_{buckle} = \frac{\pi^2 \kappa}{h^2},$$

(6.1)

where κ is the bending modulus (equal to $l_p k_B T$, where l_p is the persistence length, k_B is the Boltzmann constant, and T is the absolute temperature) [211]. In a molecular vise, the compressive force is fixed at the 9-pN base-pairing force, but the length of the target strand can vary. We therefore considered the buckling length at constant force,

$$h_{buckle} = \pi \sqrt{\frac{\kappa}{F}}.$$

(6.2)

Rods shorter than this length can support the compression; rods longer cannot and instead adopt bent conformations known as elastica (Figure 6-2). For a persistence length of 46.5 nm and a base-pairing force of 9 pN, Equation (6.2) predicts the buckling length to be 14.5 nm (42.5 bp). This estimate is based purely on continuum mechanics, and neglects thermal fluctuations as well as all molecular details. Next, we present a more detailed statistical mechanical model which incorporates some of these effects.
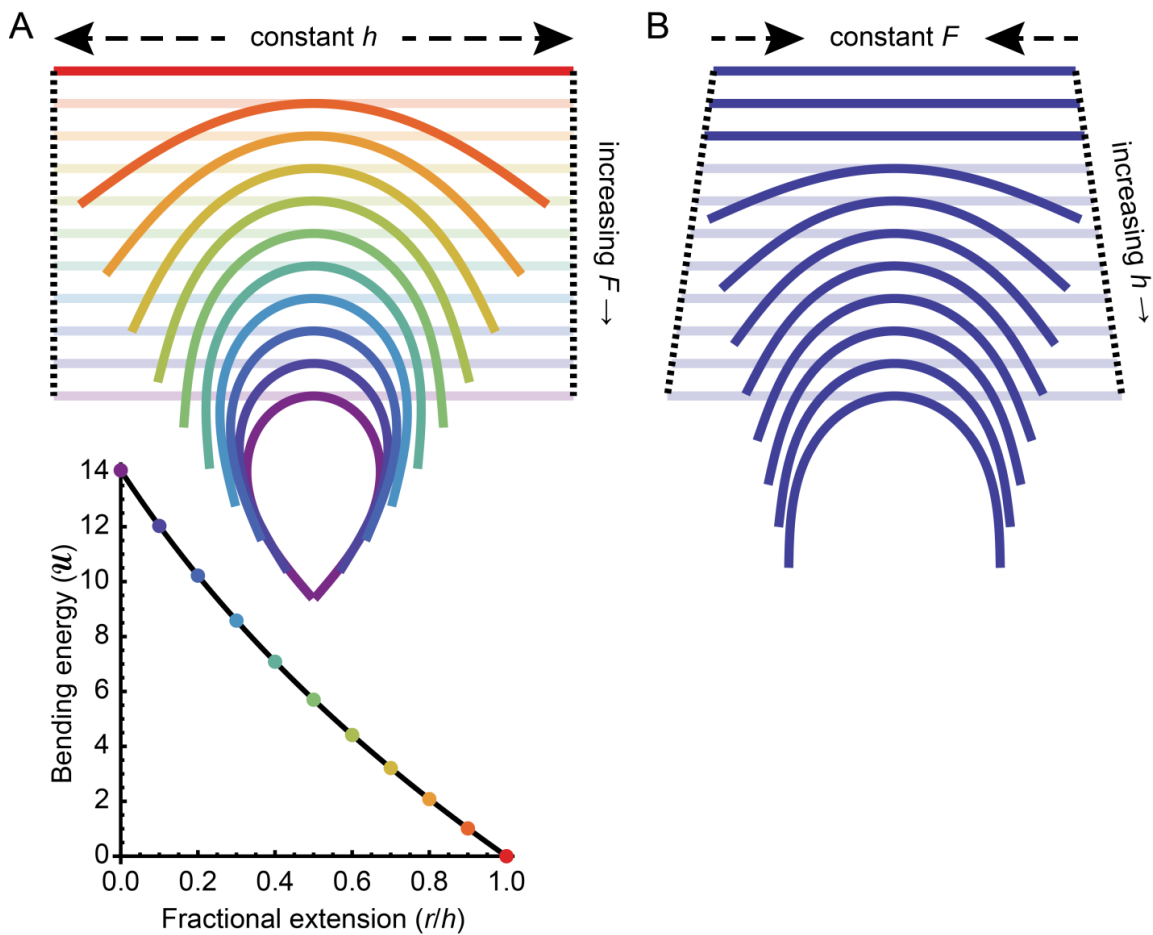
Figure 6-2 Classical mechanics of Euler buckling of rigid rods under compressive force ("elastica"). (A) Top: rods of constant length under increasing compressive force. Bottom, bending energy as a function of fractional end-to-end extension. Colored points correspond to the same-colored configurations above. Dimensionless bending energy is defined $\mathcal{U} \equiv U h/\kappa$, where h is the contour length and κ is the bending modulus. In these units the energy to bend a rod into a perfect circle is $\mathcal{U} = 2\pi^2$. (B) Conformations of rods of increasing length under constant compressive force. These shapes correspond to DNA of length 40–50 bp experiencing a compressive force of 9 pN, in the absence of thermal effects. The buckling transition occurs between 42 and 43 bp.

6.1.3 Statistical mechanics of molecular vises

We constructed a coarse-grained statistical mechanical model of the molecular vises to predict the shapes of the FRET curves. The model included three types of energy: the base-pairing energy within the stem and within the target strand (discretized at the single-bp level); the force-extension energy of the unhybridized

117

single-stranded DNA; and the bending energy of the double-stranded target strand. The treatment of the target strand in our model is equivalent to the WLC. We calculated the thermal equilibrium ensemble of molecular conformations, and from this, the ensemble-average FRET for each loop and complement combination.

The partition function we derived includes degrees of freedom corresponding to the extent of base-pairing in the stem and target strand, as well as the end-to-end distance (i.e. amount of bending) of the target strand:

$$Z = \sum_{n_{stem}=0}^{20} \sum_{n_A=\frac{n_L}{2}-\left|\frac{n_h}{2}\right|}^{n_L/2} \sum_{n_D=\frac{n_L}{2}-\left|\frac{n_h}{2}\right|}^{n_L/2} \int_{r_{min}}^{r_{max}} dr \, z[r, n_{stem}, n_A, n_D, n_L]$$

$$(6.3)$$

$$z[r, n_{stem}, n_A, n_D, n_L] = \exp\left[-\frac{1}{k_B T}\left(G_{bp}^{stem} + G_{bp}^{loop} + G_{ss} + G_{rod}\right)\right]$$

where n_{stem}, n_A, and n_D are the number of *unpaired* bases in the stem, the side of the loop closer to the acceptor dye (5′ side), and the side of the loop closer to the donor dye (3′ side), respectively; r is the end-to-end distance of the duplex target strand; r_{min} = 1.8 nm is the displacement between the two base-paired strands at the end of a DNA double helix; n_L is the number of nucleotides in the loop; and n_h is the number of nucleotides in the complement strand. We truncate the sum at n_{stem} = 20 because successive terms contribute negligibly. The base-pairing free energies G_{bp} are each calculated using sums of nearest-neighbors dinucleotide energies from laser tweezers unzipping experiments [212] and the relevant sequences (with loss of hybridization given by n_{stem} or n_A and n_D).

We modeled the single-stranded region as a freely jointed chain [213]; ignoring constant terms, we have

$$G_{ss} \approx \frac{L_{ss}}{b} \left(f_{ss} \mathcal{L}^{-1}(f_{ss}) - \ln \left(\frac{\sinh \mathcal{L}^{-1}(f_{ss})}{\mathcal{L}^{-1}(f_{ss})} \right) \right)$$

$$L_{ss} = l_{ss}(2n_{stem} + n_A + n_D)$$

$$f_{ss} \equiv \frac{r_{ss}}{L_{ss}} = \frac{r - r_{min}}{L_{ss}}$$

$$\mathcal{L}(y) \equiv \coth y - \frac{1}{y}$$

(6.4)

where L_{ss} is the contour length of the single-stranded portion of the loop, including unzipped bases from the stem. The parameters for this model are the Kuhn length (b) and the per-nucleotide contour length (l_{ss}) of single-stranded DNA. Salt-dependent values for both parameters are available from the same reference as the base-pairing energies [212]. To simplify integration, we approximate the inverse Langevin function as

$$\mathcal{L}^{-1}(f_{ss}) \approx \frac{f_{ss}(f_{ss}^2 - 3f_{ss} + 3)}{1 - f_{ss}}. \tag{6.5}$$

The equilibrium conformation of a rigid rod buckled by compressive force is given by a set of curves known as elastica; their associated bending energy is [211, 214]

$$G_{rod} = \frac{8\kappa K^2(m)}{L_{ds}} \left(\frac{f_{ds} - 1}{2} + m \right)$$

$$L_{ds} = l_{ds}(n_L - n_A - n_D)$$

(6.6)

where $K(m)$ is the complete elliptic integral of the first kind, L_{ds} is the contour length of the double-stranded portion of the loop, l_{ds} is the per-nucleotide contour length of double-stranded DNA, and the parameter $m \geq 0$ is the solution to

$$f_{ds} \equiv \frac{r}{L_{ds}} = 2\frac{E(m)}{K(m)} - 1 \qquad (6.7)$$

where $E(m)$ is the complete elliptic integral of the second kind. The value of m specifies the conformation of the rod. When m = 0, the rod is fully extended (f_{ds} = 1); as m increases, the rod becomes increasingly bent. We simplify the integration by approximating

$$m \approx (1 - f_{ds})(M + (4M^2 - 3M)f_{ds} + (1 + 2M - 4M^2)f_{ds}^2) \qquad (6.8)$$

where M = 0.8261... is the value of m at which the rod is maximally bent, such that its ends are touching (i.e., when f_{ds} = 0). We neglected fluctuations in degrees of freedom beyond the principal flexural mode. The energy and equilibrium conformation of a buckled rod (of constant contour length) is plotted as a function of end-to-end distance in Figure 6-2.

Observables are predicted using the appropriate partition sums and integrals. The ensemble average FRET efficiency is predicted by

$$E_{FRET}$$
$$= \frac{1}{Z} \sum_{n_{stem}=0}^{20} \sum_{n_A = \frac{n_L}{2} - \left|\frac{n_h}{2}\right|}^{n_L/2} \sum_{n_D = \frac{n_L}{2} - \left|\frac{n_h}{2}\right|}^{n_L/2} \int_{r_{min}}^{r_{max}} dr \frac{z[r, n_{stem}, n_A, n_D, n_L]}{1 + \left(\frac{r_{min} + f_{dye}(r - r_{min})}{R_0}\right)^6} \qquad (6.9)$$

where R_0 is the Förster radius of Cy3B and Alexa 647, and

$$f_{dye} \equiv \frac{1 + 2n_{stem}}{2n_{stem} + n_A + n_D} \qquad (6.10)$$

represents the ratio of the distance between the dyes to the distance between the ends of the target strand. Equation (6.10) models the dyes as separated by a fixed fractional distance of the total single-stranded DNA extension, neglecting any fluctuations other

than the end-to-end fluctuations of the entire chain. We used a range of values for R_0

(Table 6:1) within a previously estimated range for Cy3B and Cy5 [215] to account for

the uncertainty both in its value and in the other parameters and assumptions in the

model.

Table 6:1 Parameter values and sources used in the statistical mechanical model of
DNA buckling in molecular vises

Name	Symbol	Value	Source
dsDNA persistence length	l_p	46.5 nm	[177, 216]
dsDNA rise per base	l_{ds}	0.34 nm	[152, 216]
dsDNA width	r_{min}	1.8 nm	PDB structure 3BSE [217]
dsDNA base-pairing energies	G_{bp}	various (see ref)	[212] (values for 250 mM salt)
ssDNA Kuhn length	B	1.25 nm	[212]
ssDNA rise per base	l_{ss}	0.59 nm	[212]
Cy3B/Alexa647 Förster radius	R_0	5.7–6.7 nm	[215]

These parameters were used to fit all data. r_{min} and R_0 were assumed to be
independent of salt concentration; for the other parameters, the listed references
include salt dependences used in salt-dependent simulations.

The model allowed us to validate certain aspects of the vise design. We tested

computationally whether the ends of the target strand remained hybridized or whether

they unzipped under compressive load. When the target strand contained A-T base pairs

near its ends, the model predicted partial fraying of the ends. However, when the target

contained all G-C base pairs outside the central 18 (as was the case in our experiments),

then fraying was eliminated.

This statistical mechanical model focuses on the key mechanical aspects of the

molecular vise but ignores numerous other details, such as fluctuations in the buckled

rod or single-stranded DNA beyond the principal degree of freedom; torsional effects in

the target strand; the length and fluctuations of the dye linkers; the relative orientation of the dyes; the details of base-pairing beyond the nearest-neighbors model; sequence-specificity in dsDNA or ssDNA bending moduli; and electrostatic interactions between different parts of the construct and each other or surrounding ions. An atomistic model might better account for these effects, at the expense of significant mathematical and computational complexity.

6.2   Results

6.2.1   Euler buckling of DNA at low salt

We synthesized five molecular vises with loop sizes L = 30, 36, 40, 46, and 50 nt, all with the same stem, and mixed aliquots of each with a series of complementary strands of varying length h. Samples were analyzed by native polyacrylamide gel electrophoresis (PAGE) and imaged on a commercial fluorescence scanner (Figure 6-3 A and Section 6.5.2). PAGE was used to segregate the desired construct from molecular aggregates. Hybridization of the target was confirmed by a length-dependent decrease in mobility relative to the unhybridized hairpin. FRET efficiencies were extracted from gel images (Section 6.5.4) and plotted as a function of the length of the target strand (Figure 6-3 B).
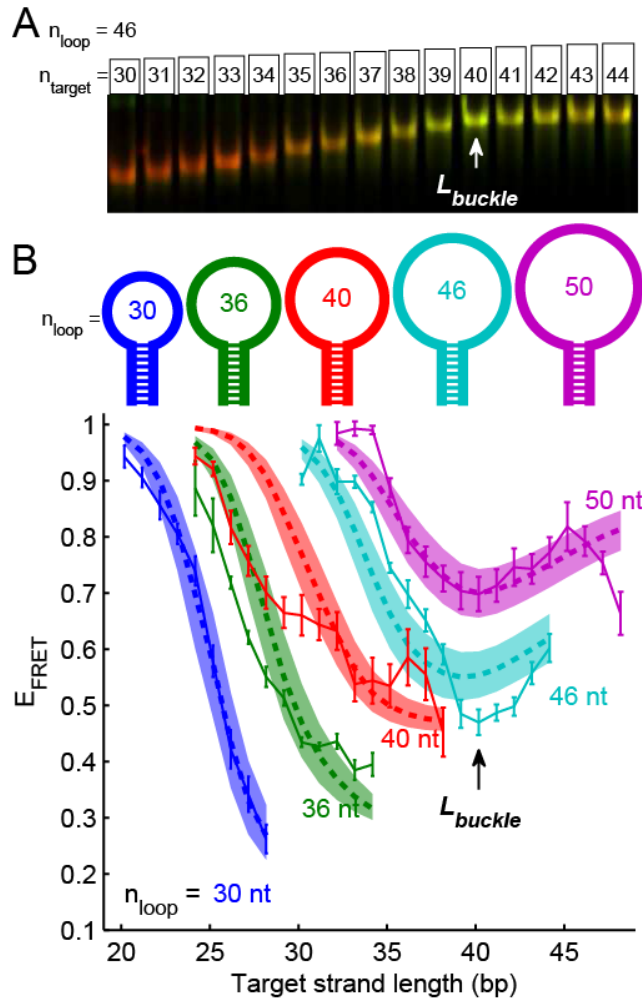
Figure 6-3 Combined measurements of electrophoretic mobility and FRET. (A) Molecular vises of five loop sizes (30, 36, 40, 46, and 50 nt) were each bound with varying-length target strands, analyzed by native polyacrylamide gel electrophoresis, and imaged on a commercial scanner. (B) FRET efficiency was quantified from gel images and plotted for each loop size as a function of the target strand length. The local minimum in FRET efficiency at a target strand length of 40 bp signified the buckling transition and was consistent with the predictions of a statistical mechanical model (shaded areas; see Section 6.1.3 for details). The buckling transition also manifested as a change in the dependence of electrophoretic mobility on target length (A; quantified in Figure 6-4). Error bars in B are SEM from four independent replicates.

In the three smaller loops (30, 36, and 40 nt) the target strand was always shorter than the predicted buckling length. The FRET efficiency decreased monotonically with increasing complement length, consistent with the target strand remaining straight and unzipping the stem. In the larger loops (46 and 50 nt), the FRET efficiency showed a

local minimum at a complement length of 40 or 41 bp. The complement length at which this transition occurred was in good agreement with the buckling length predicted by linear elasticity [Equation (6.2)]. The transition in FRET also coincided with a transition in electrophoretic mobility: for targets less than 40 bp, mobility and target length were inversely related, while for targets longer than 40 bp, mobility was nearly independent of target length, suggesting a more compact conformation for the assembly (Figure 6-4).
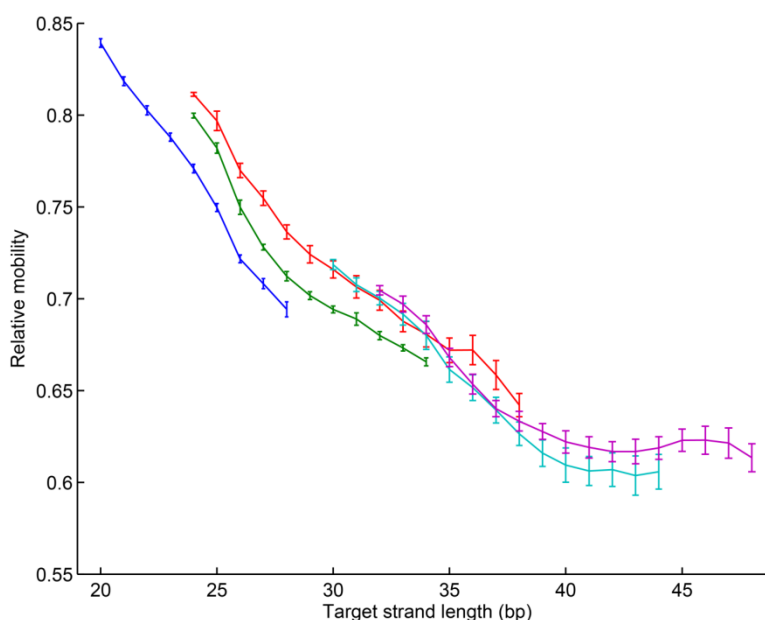
Figure 6-4 Relative electrophoretic mobility of five loop sizes of molecular vises as a function of target strand length (colors as in Figure 6-3 B). Relative mobility was defined as the distance traveled by the complex divided by the distance traveled by the molecular vise in the absence of a complementary strand (i.e., the hairpin only). Below the buckling transition ($h = 40$), the relative mobility decreased with increasing target strand length; beyond the buckling transition, increasing target strand length did not significantly affect the relative mobility, suggesting that the complex adopted an increasingly compact structure.

The predictions of our statistical mechanical model (Section 6.1.3) reproduced the essential features of the experimental data (Figure 6-3 B), including the monotonic loss of FRET with increasing complement length in the three shorter hairpins, and the local minimum in FRET at the buckling transition length of 40 bp (thermal fluctuations

shortened the buckling length slightly relative to the purely mechanical estimate). The shaded regions depict the uncertainty in the model due to uncertainty in literature values of physical parameters (see Section 6.5.5 for fitting procedure). The overall agreement between the predicted and measured FRET curves, despite the simplifications in the model, provides strong support for the WLC picture of DNA bending. Our data thus verify the WLC at curvatures up to 7°/bp (Figure 6-5), significantly beyond the highest curvature probed by bulk cyclization experiments (3.4°/bp [181]) or by recent single-molecule cyclization experiments (5.4°/bp [183]). Deviations from the WLC, particularly a softening at high curvature, would manifest as a bending transition at a shorter target strand length than we observed.

In some regions the FRET curves deviated from the model. The slight discrepancy between predicted and measured FRET for short targets in the small loops is likely due to steric clash between the double-stranded target region and the inward-pulling single stranded parts of the loop, an effect not included in the model. The loss of FRET for the longest complement lengths (46–48 bp) in the 50 nt loop was not predicted by our simple model. The concomitant decrease in electrophoretic mobility (Figure 6-4) suggested a structural rather than photophysical basis for the effect; we hypothesize that this deviation may be due to electrostatic repulsion between the ends of the buckled target strand, inhibiting them from nearing each other.
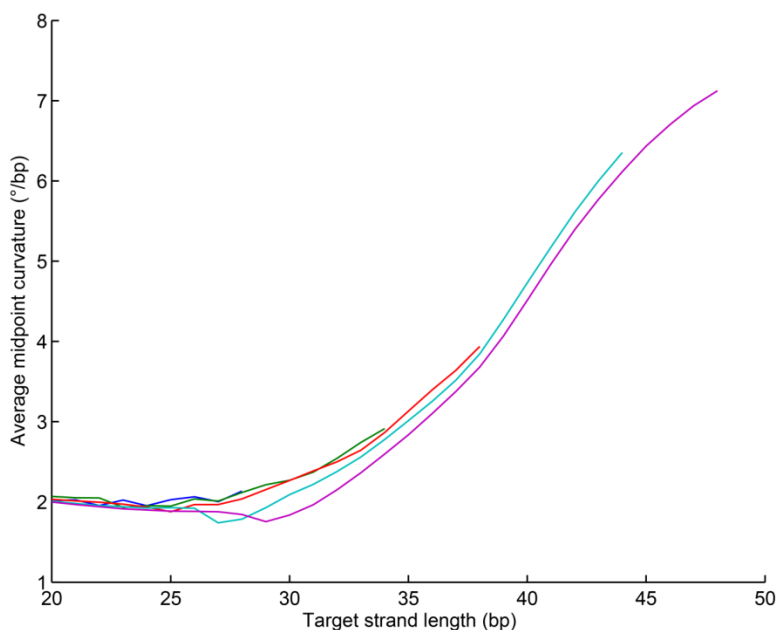
Figure 6-5 Predicted ensemble average curvature at the apex of molecular vises (the midpoint of the target strand) of five loop sizes (colors as in Figure 6-3 B). In the absence of thermal effects, the curvature would be zero when the target strand is shorter than the buckling length (40 bp), but would rise sharply at longer lengths (Figure 6-2 B). According to our statistical mechanical model, thermal fluctuations smooth out the buckling transition so that the angle increases gradually. We also predict that thermal fluctuations produce a baseline average curvature of 2°/bp for short target strands. The maximum average curvature that our model predicts for any of our constructs is 7°/bp.

6.2.2 Salt-induced nonlinear kinks

Under the ionic conditions of our experiments, the double stranded persistence length is expected to be largely independent of the concentration of sodium or magnesium [152, 216]. However, the persistence length only reflects the low-curvature bending modulus; the effects of ionic strength on DNA bending at high curvature have not been explored. Recent measurements reporting enhanced flexibility of DNA at short length scales were conducted in unphysiologically high sodium or magnesium, raising the question of whether these results apply under physiological conditions [183].
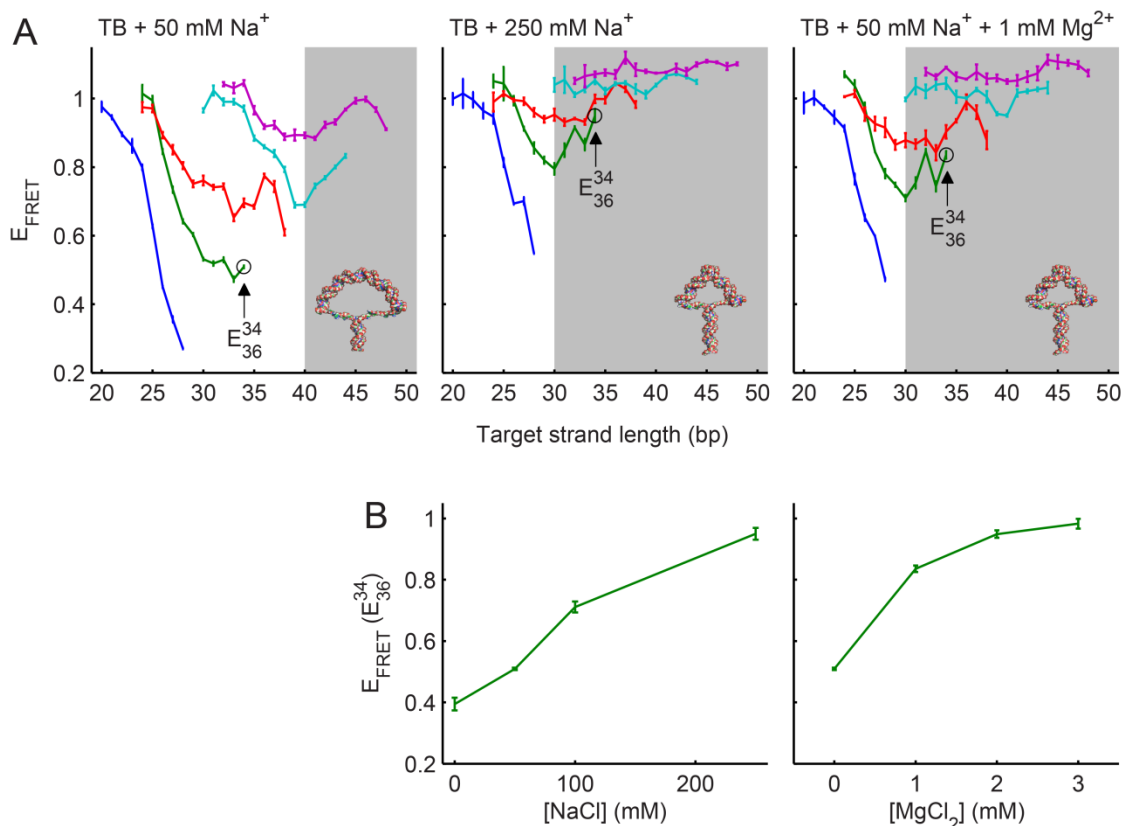
Figure 6-6 Effect of ionic strength on duplex DNA bending in molecular vises. (A) FRET efficiency as a function of target strand length for five loop sizes (colors as in Figure 6-3 B). Addition of 50 mM NaCl did not shift the buckling transition from its original position at 40 bp (left). The presence of 250 mM NaCl (center) or of 50 mM NaCl and 1 mM MgCl$_2$ (right) led to a new bending transition at a target strand length of 30 bp and a loss of contrast in the original buckling transition at 40 bp. The transition at 30 bp is inconsistent with Euler buckling and represents a physically distinct bending mode, which we term "kinking". (B) The transition of the dominant bending mode from Euler buckling to kinking was quantified by E_{36}^{34} (as indicated in A). In a background of 89 mM tris/borate, the transition occurred between 50 and 100 mM NaCl (left). In 89 mM tris/borate and 50 mM NaCl, the transition occurred upon addition of 1 mM MgCl$_2$ (right), indicating that Mg^{2+} stabilized the kinked structure significantly more efficiently than did Na$^+$. Full FRET curves for all ionic conditions are in Figure 6-7. Error bars are SEM from at least three independent replicates.

We used molecular vises to measure the effect of sodium or magnesium (in a background of 89 mM tris/borate) on the bending rigidity of intact duplex DNA (Figure 6-6 and Figure 6-7). At 50 mM Na$^+$ the buckling transition at 40 bp was preserved; but at 250 mM Na$^+$ or 1 mM Mg^{2+} the FRET curve was dramatically different, with a new

127

bending transition at a target strand length of 30 bp. As the ionic strength increased, the

depth of the FRET minimum at 30 bp grew and that at 40 bp shrank, suggesting the

existence of two distinct modes of bending. We quantified the transition between the

two modes by the FRET efficiency of a complex (E_{36}^{34}) which showed low FRET in low salt

and high FRET in high salt. The transition (Figure 6-6 B) occurred between 50 and

100 mM NaCl (in 89 mM tris/borate) or at approximately 0.5 mM MgCl$_2$ (in 89 mM

tris/borate and 50 mM NaCl).
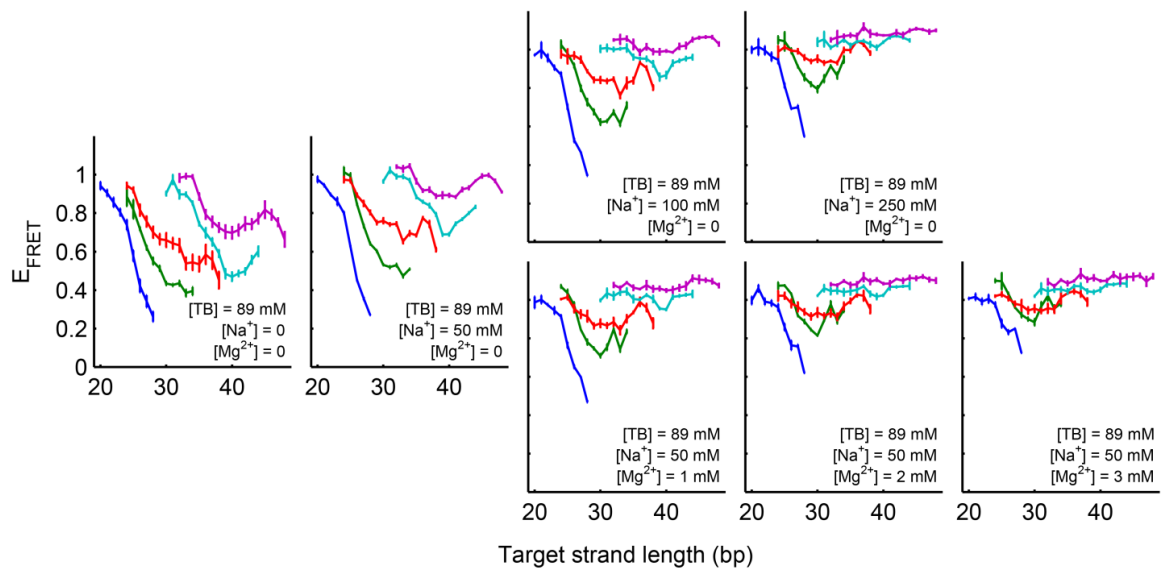
Figure 6-7 Effect of ionic strength on duplex DNA bending in molecular vises: full results. Shown here are the FRET efficiencies of the five molecular vises (colors as in Figure 6-3 B) at all target strand lengths at all tested salt mixtures, extending the plots shown in Figure 6-6. Inscriptions list all buffer components other than deionized water; "TB" means equimolar tris/borate. The coexistence of the two bending transitions, buckling (40 bp) and kinking (30–33 bp), was most evident at [Na+] = 100 mM (center, top) or at [Na+] = 50 mM, [Mg2+] = 1 mM (center, bottom). Buckling was dominant at lower ionic strength, but was replaced by kinking at higher ionic strength.

We asked whether the influence of salt could be accounted for by tuning

parameters of our WLC-based statistical mechanical model. We simulated the effects of

increased salt on base-pairing force, single-stranded persistence length, and double-

stranded persistence length using the known salt-dependence of these parameters [212]. The simulations did not match the observed FRET behavior (Figure 6-8 A). Indeed, to achieve a buckling length of 30 bp would require a decrease in persistence length of the target to 25 nm, well below all literature values (Figure 6-8 B). Thus at high ionic strength the dsDNA bent more than predicted by the WLC model.
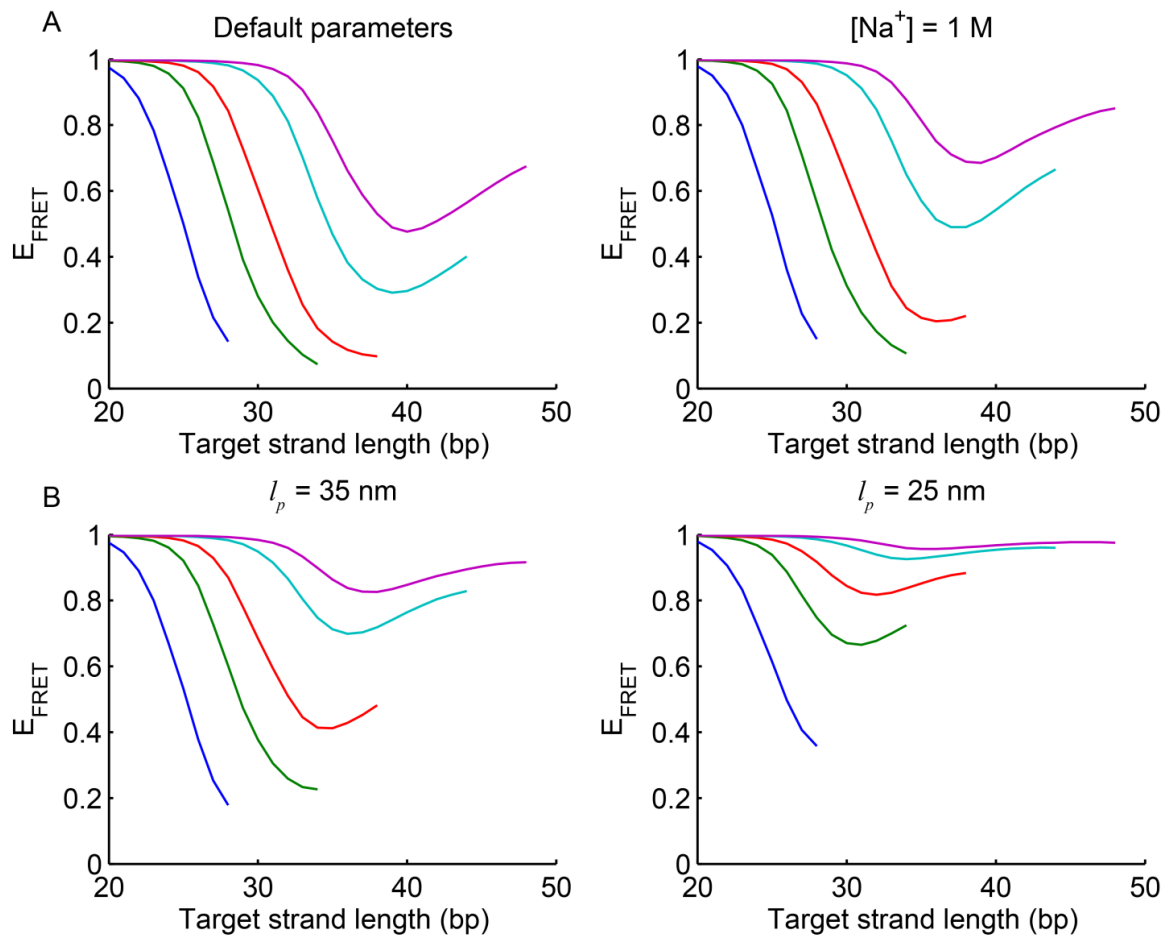
Figure 6-8 Effects of model parameters on predicted FRET curves. (A) Increasing the base-pairing energies and the flexibility of single-stranded DNA to the values at 1 M monovalent salt [212] only slightly shifted the expected buckling length and did not explain the appearance of a bending transition at 30 bp at high ionic strength (Figure 6-6 and Figure 6-7). (B) To achieve a buckling transition at 30 bp, the double-stranded DNA persistence length had to decrease from 46.5 nm to 25 nm, a physically implausible value. The model predicted the shift from buckling at 40 bp to buckling at 30 bp to be gradual: intermediate conditions yielded intermediate transition lengths. Experimentally, we observed the coexistence of two distinct bending transitions without intermediate buckling lengths (Figure 6-7), in contradiction to the predictions of the WLC model. Colors are as in Figure 6-3 B.

We thus hypothesized that high ionic strength stabilized a kinked state of DNA which did not manifest under thermally accessible curvatures. Localized curvature-induced melting has been proposed as a molecular mechanism for nonlinear kinking in dsDNA [155, 218]. In this "meltable WLC" (MWLC) model, the dsDNA forms a short bubble of two ssDNA strands with a correspondingly shorter persistence length. The MWLC model preserves the bulk persistence length because thermally induced bubbles form at negligible density in unstrained DNA.

The free energy to form a kink has two components:

$$\Delta G_{kink} = \Delta G_{bubble} + \Delta G_{collapse} , \qquad (6.11)$$

where ΔG_{bubble} is the free energy cost (positive) to form a sharply bent region of locally melted DNA, and $\Delta G_{collapse}$ is the free energy gain (negative) by conformational relaxation in the rest of the molecular vise. ΔG_{bubble} has three contributions: (1) loss of base pairing energies within the bubble; (2) a correction for the pinned ends of the bubble (called the "cooperativity factor" [219, 220] and "loop factor" [221]); and (3) bending of the locally melted region [182]. $\Delta G_{collapse}$ also has three components: (1) relaxation of the curvature in the double-stranded regions of the target; (2) relaxation of the stretch of the single-stranded tethers; and (3) zipping of the stem. We applied our statistical mechanical model (Section 6.1.3) to estimate $\Delta G_{bubble} \approx -\Delta G_{collapse} \approx 15 - 20 \ k_B T$. While the parameters used in the calculation are uncertain, the fortuitous similarity in magnitude of ΔG_{bubble} and $\Delta G_{collapse}$ likely accounts for the sensitive salt-dependent equilibrium between buckling and kinking. The dominant effect of salt is to

favor the kinked state through an increase in the free energy gains from zipping the stem and relaxing the single-stranded tethers.

6.2.3 Flexibility of mismatched DNA

We next applied molecular vises to study the flexibility of DNA containing single base-pairing mismatches. These experiments served two functions. First, they tested the MWLC model, which predicts that the more unstable the mismatch, the less the additional cost to nucleate a bubble, and the greater the propensity to kink. Second, these experiments tested whether mismatch flexibility is correlated with efficiency of mismatch recognition and repair *in vivo* [222, 223]. This second question connects the underlying biophysics of mismatched DNA to an important process for cell survival and, ultimately, evolution.

Single mismatches are insufficient to alter the equilibrium conformation of bare DNA significantly from the standard B-form [222, 223]. Solution NMR has found varying levels of increased conformational heterogeneity at mismatch sites [222]; however, these experiments only probed thermally accessible conformations, and spectra could not be related directly to curvature of the DNA backbone. Others have inferred mismatch flexibility from sensitivity to T4 endonuclease VII cleavage [224], but this assay may depend on the specifics of the nuclease-DNA interaction rather than on the intrinsic properties of the DNA. Under native conditions, mismatched DNA shows similar electrophoretic mobility to intact DNA, but under slightly denaturing conditions mismatches decrease the electrophoretic mobility, suggesting a mismatch-induced conformational change [225].

To investigate the flexibility of mismatched DNA in the absence of protein binding or denaturants, we introduced each of the eight possible single mismatches at positions located within one nucleotide of the apex of the target strand (sequences are listed in Section 6.5.6). In all cases the presence of the target strand shifted the electrophoretic mobility of the vise, confirming that the target hybridized to the loop. We measured the FRET efficiency as a function of target strand length and loop length (Figure 6-9 A), under ionic conditions where perfectly complementary targets showed WLC behavior. We used E_{30}^{28} as a qualitative measure of flexibility, with greater FRET indicating greater flexibility.
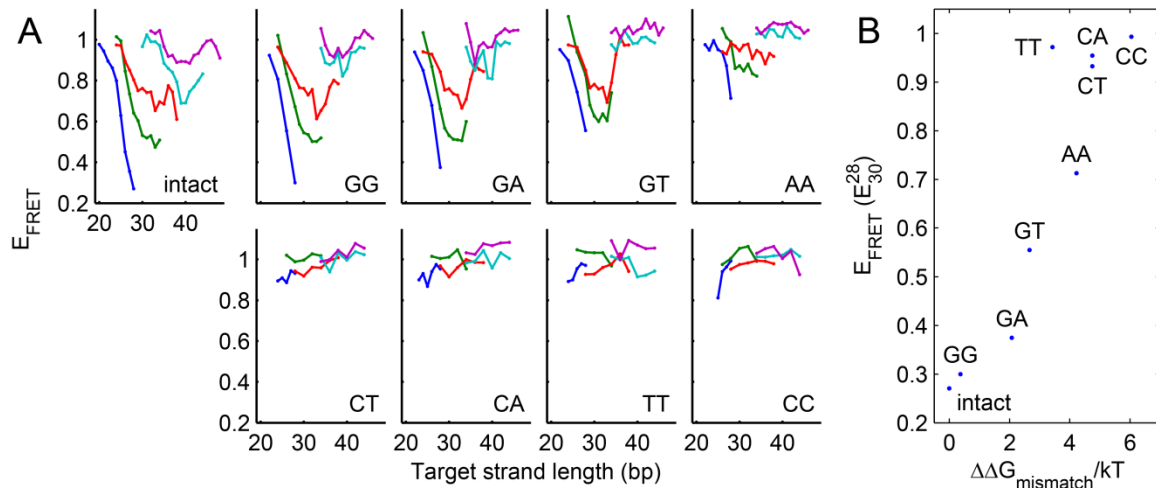
Figure 6-9 Relative flexibility of base-pairing mismatches. (A) FRET efficiency as a function of target strand length for target strands containing each of the eight possible single base-pairing mismatches. Each mismatch was probed in molecular vises with five loop sizes (colors as in Figure 6-3 B). The bending rigidity ranked: {intact, GG, GA} > {GT, AA} > {CT, CA, TT, CC}. (B) Flexibility of the mismatches, as quantified by E_{30}^{28}, correlated significantly with the free energy penalty of the mismatch [226] (Spearman's $\rho = 0.90$; P = 2.2 × 10^{-3}).

Four mismatches (T-T, C-T, C-A, and C-C) showed little FRET contrast at any loop or complement length, suggesting that under a compression of 9 pN they kinked at a contour length < 15 bp. The G-T and A-A mismatches demonstrated intermediate FRET

132

contrast, suggesting that they retained some bending rigidity, though less than fully complementary DNA. Remarkably, the remaining mismatches (G-G and G-A) displayed FRET contrast similar to that of fully complementary DNA, indicating that these mismatches were not appreciably more flexible than fully complementary DNA. The FRET data were also broadly consistent with the trends in electrophoretic mobility, confirming that the effects were structural and not photophysical.

The MWLC model predicts that thermodynamically less stable mismatches should kink more easily. Alternate models, in which kinking arises through a structural deformation other than local melting, do not require such a correlation. Flexibility was significantly correlated with the literature values for the thermodynamic penalty of the mismatches [226] (Spearman's $\rho = 0.90$; P = 2.2×10^{-3}; Figure 6-9 B). This observation strongly supports the MWLC model of kinking.

The relative propensity of the different mismatches to kink also correlated with their biological activity. T4 endonuclease VII, thought to cut at "kinkable" sites, was reported to show low activity on all G-mismatches, intermediate activity on A-A, C-A, C-T, and T-T mismatches, and highest activity on C-C mismatches, in direct correspondence with the flexibilities we measured [224]. The most flexible mismatch in our assay, C-C, is also the least efficiently repaired by the *E. coli* mismatch repair system [204]. Thus the nonlinear mechanical properties of mismatched DNA play an important role in its interaction with DNA-processing enzymes.

6.2.4   Biochemical probes of kinked DNA

The MWLC model predicts that kinking of DNA involves melting of the base pairs at the site of the kink. To test this prediction, we probed for disruption of base pairing in kinked DNA, examining putative kinks in fully complementary DNA as well as kinks in DNA containing single base-pair mismatches. The single-strand-specific S1 endonuclease is reported to cleave dsDNA in regions where the base-paired double-helical structure has been disrupted [227, 228]. We added S1 endonuclease to molecular vises with a loop of length 36 and a range of fully complementary and mismatched target lengths, under ionic conditions that favored kinking (Section 6.5.3). Cleavage products were resolved by denaturing polyacrylamide gel electrophoresis (Figure 6-10). S1 readily cleaved molecular vises in the single-stranded regions of the loop flanking the target strand. Under kinking-induced local melting, S1 also cleaved the dsDNA at the location of the kink.

Under high salt conditions, S1 cleaved the perfectly complementary target of length 34 bp, but not shorter targets. These results confirm disruption of base-pairing in the strongly kinked state. We infer that for shorter targets, kinking was insufficient to sensitize cleavage to S1 nuclease, either because the melting in the kinked state was incomplete or transient, or because our assay was not sensitive enough to detect a low level of cleavage. Inclusion of a single G-G or C-C base-pairing mismatch sensitized target strands of length 30 bp or higher to S1 cleavage, indicating disruption of base pairing under high curvature of mismatched DNA. Cleavage rates were much greater for

the mismatched DNA than for the intact kinked DNA, suggesting a greater extent of structural disruption in the mismatches, consistent with the MWLC model.
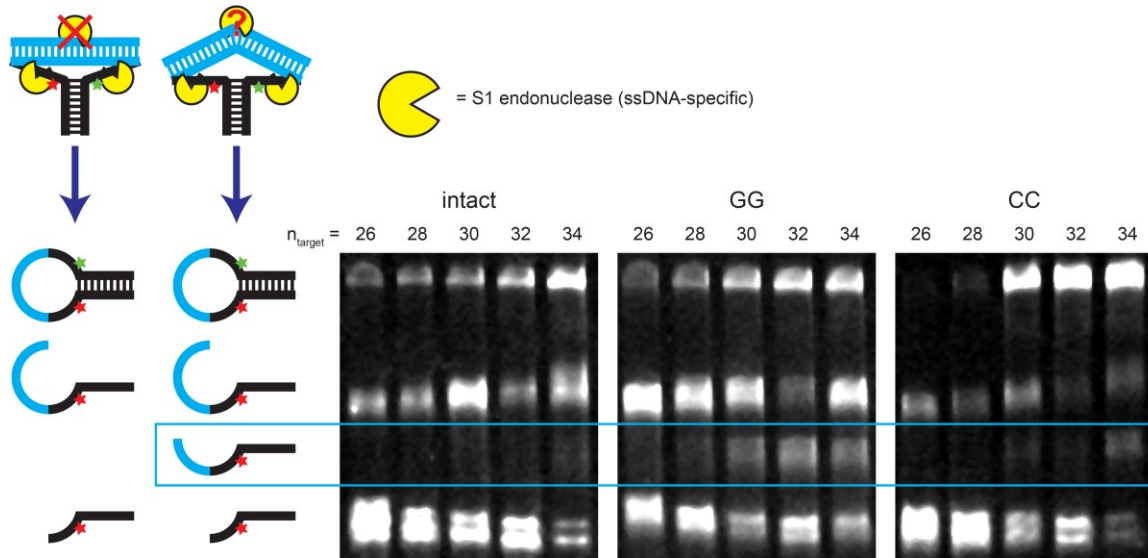
Figure 6-10 Cleavage of kinked target strands in a molecular vise by S1 endonuclease at high ionic strength. Molecular vises with a 36-nt loop and varying length target strands were treated with the single-stranded-DNA-specific S1 nuclease in a high-ionic-strength buffer and analyzed by denaturing PAGE. The target strands were either fully complementary (left image) or contained a single GG (center image) or CC (right image) mismatch. The different complexes reacted at different rates; the cleavage reactions were quenched at 135 minutes (intact, left), 15 minutes (GG, center), or 45 minutes (CC, right). Cartoons on the left depict cleavage products and reactants. The longest band (top) was the undigested hairpin. Of the cleavage products, the longest resulted from cleavage of the loop at its 3' end; the shortest resulted from cleavage of the loop at its 5' end; and the middle band, when present, resulted from cleavage within the target strand. This band appeared weakly in the intact target strand of length 34 bp, and prominently in the mismatched target strands of length greater than 30 bp. Cleavage within the target strand indicated kinking-induced disruption of base pairing.

6.3 Discussion

The energy to distort a strand of dsDNA $f(c,\tau)$ is a function of local curvature, c, and torsion, τ. This function can have a complicated shape, and in general depends on the temperature, chemical environment, and underlying DNA sequence. The WLC model amounts to approximating $f(c,\tau)$ by a paraboloid. This approximation must be valid for

sufficiently small curvatures, and must break down at sufficiently high curvatures. Kinking is a signature of breakdown in the parabolic approximation; it implies that the mean curvature has reached a value where $f(c,\tau)$ is concave. In such a region, the total energy is lower when the molecule separates into regions of high curvature and low curvature, rather than maintaining the mean curvature throughout. Figure 6-11 illustrates how a concave region of $f(c,\tau)$ arises naturally in the MWLC model. At low curvatures, the fully base-paired DNA is more stable; at high curvatures, the energetic cost of melting is compensated the decreased energetic cost of bending locally melted DNA.
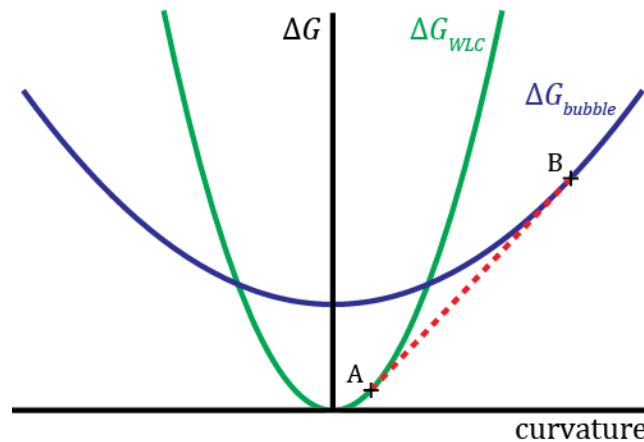
Figure 6-11 Energy landscape of the MWLC model. The WLC model (green) approximates the bending energy as a quadratic function of the curvature. In the MWLC model, bubbles of locally melted DNA can form. The bending energy of a bubble (blue) is also modeled as a parabola, offset from the WLC curve by the amount of energy required to form the bubble and with shallower slope due to the increased flexibility of the melted region. If the average curvature of the entire strand is constrained to be between the points labeled A and B in the plot, then it is energetically favorable for the strand to kink, with a fraction of the sequence melted and of curvature B, and the remainder intact and of curvature A. The dashed red line, which is tangent to both of the curves, corresponds to the bending energy of a kinked strand as a function of its average curvature.

136

Thermal fluctuations can only generate small deviations from equilibrium curvature; far larger deviations are attained in many actively produced DNA conformations in the cell. Hybridization of short oligonucleotides to a small ring of DNA has previously been used to probe DNA bending at high curvature [200, 201], but in these experiments the nonlinear elastic properties of the single-stranded region of the ring complicated interpretation of the results. The key merit of the molecular vise geometry is that it generates high curvatures under well-defined forces, with an unambiguous fluorescence readout of molecular conformation.

Our results provide insight into the controversies and apparent discrepancies among previous measurements of DNA bending. All reported bulk-scale solution cyclization experiments have been consistent with the WLC model [177], with two exceptions. The validity of the first [179] has been questioned [181] due to its use of possibly saturating ligase concentrations. The results of the second [182] were consistent with a MWLC model.

The recent single-molecule cyclization results of Vafabakhsh and Ha [183] suggested that short, unconstrained DNA strands are significantly more flexible than the WLC prediction. These experiments were performed in buffers containing 10 mM magnesium or > 500 mM sodium and probed rare thermal excursions to regions of high curvature. Our results suggest that this observed increase in DNA flexibility at high curvature may be due to the high ionic strength, which may facilitate local melting. Two other studies observed kinking of short pieces of DNA in minicircles in buffers containing magnesium or other divalent cations [201, 228]. A computational model of counterion

condensation predicted that kinked structures would be better stabilized in high ionic strength solution, particularly when the cation was Mg^{2+} [229].

6.4 Conclusion and future directions

Molecular vises, in combination with our simple statistical mechanical model, are a powerful platform for studying DNA bending mechanics. While we have focused on intact DNA and single-nucleotide mismatches, one could use the same approach to study the effects of many other perturbations. For instance, mechanical changes may arise from variations in the target sequence (e.g. inclusion of A-tracts [230]), epigenetic modifications (e.g. methylation of cytosine [231] or adenine [232]), damage (e.g. thymine dimers [233] or 8-oxoguanine), DNA modifying drugs (e.g. cisplatin [234] or doxorubicin [235]), or hybridization with RNA.

Molecular vises might also be used to investigate the role of DNA mechanics in protein-DNA interactions. Two classes of effects may be investigated. First, pre-bending of DNA may affect its interactions with proteins, particularly when the bound state or a reaction intermediate involves bending the DNA. For instance, recognition of mismatches by the MutS protein is thought to depend on the equilibrium between bent and unbent states of the protein-DNA complex [222, 236]. Using a molecular vise to bias mismatched DNA towards the bent state might modulate binding and recognition.

Second, molecular vises could report on the conformational changes induced in DNA by protein binding. Numerous proteins, such as transcription factors and architectural modulators, bend the DNA they bind [162, 177, 237] and therefore might

directly alter the FRET efficiency of a molecular vise. Additionally, the compressive force applied by the molecular vise "pre-stresses" the binding site so that even a small increase in flexibility upon protein binding might be amplified into a large change in FRET.

A particularly useful feature of molecular vises and other FRET-based probes of protein binding [238, 239] is that the protein itself does not need to be labeled. For sequence-specific DNA-binding proteins, one could design a molecular vise containing the binding site in the target strand. Protein binding would lead to a change in FRET. This concept is similar to the idea underlying molecular beacons for detecting unlabeled short oligonucleotides. Finally, we note that the molecular vise structure and the FRET-based readout are amenable to single-molecule studies which may probe transient DNA-protein interactions or sparsely populated states.

6.5   Materials and Methods

6.5.1   Synthesis

All DNA oligonucleotides were purchased from Integrated DNA Technologies Inc. Each hairpin was purchased in three pieces: the two complementary halves of the stem, and the loop. A 5' terminal phosphate was included on the appropriate strands to enable ligation. Each stem strand included an amine-modified C6 deoxythymidine residue at the end next to the ligation site (these become the two outermost bases of the loop). Strands were separately labeled with Cy3B (GE Healthcare PA63101) or Alexa Fluor 647 (Invitrogen A20006) succinimidyl esters according to manufacturer protocols.

We selected Cy3B as the donor dye in place of the more popular Cy3 to avoid variations in quantum yield due to sequence- and hybridization-dependent photoisomerization [240]. Labeled strands were purified from unlabeled strands by reverse-phase HPLC. Two splint strands, each complementary to the entirety of one of the stem strands and the neighboring ten bases of the loop strand, were separately mixed with their complementary stem strands in ligase buffer. These stem solutions were then combined with each other, the loop strand, and T4 DNA ligase (New England Biolabs M0202S). Following reaction overnight at 16°C, double ligation products were purified by denaturing (7 M urea) PAGE and extracted using the crush-and-soak method. Sequences are listed in Section 6.5.6.

6.5.2   Data acquisition

Hairpins were diluted to a final concentration of 1.5 nM and mixed with an excess (circa 100 nM) of the appropriate target strand in PAGE loading buffer containing 10% glycerol (by volume), 89 mM tris/borate (pH 8.3), and 1 µM of a non-complementary oligonucleotide (to block non-specific interactions). Samples were annealed by heating to 95°C for at least five minutes, followed by cooling to 25°C at a rate of 1°C/45 sec. The native running buffer consisted of 89 mM tris/borate. Native PAGE gels (7.5%) were cast in-house in native running buffer. The samples were loaded and run for 1 hour at 150 V. To test the effects of ionic strength on conformation, gels were soaked in a series of buffers containing 89 mM tris/borate and varying concentrations of sodium chloride and/or magnesium chloride. Following each 20-minute soak, gels were imaged on a Typhoon Trio (GE Healthcare), with excess buffer

included to avoid changes in ionic strength due to evaporation during the scan. We simultaneously collected two fluorescence images using 532 nm excitation, A_{GG} representing green emission (565–595 nm) and A_{GR} representing red emission (655–685 nm). We then took a third image under 633 nm excitation using the red emission filter, A_{RR}. All images were taken at 100 μm pixel spacing using a PMT gain of 750 V. FRET values were extracted from images as described in Section 6.5.4.

6.5.3 S1 nuclease digestion

Aliquots of the 36-nt loop hairpin were diluted to a concentration of 1 nM with an excess (circa 1 mM) of the appropriate target strand in 10 μL reaction buffer (100 mM NaCl, 3 mM MgCl$_2$, 1 mM ZnCl$_2$, and 89 mM tris/borate; pH 8.3). We note that Zn^{2+} has been found to facilitate kinking in AFM experiments [241], but include it to facilitate S1 nuclease reactivity [242]. Samples were annealed by heating to 95°C for five minutes, followed by cooling to 25°C at a rate of 1°C/45 sec. Reactions were initiated by addition of 356 units S1 nuclease (Promega M5761) in 10 μL of identical buffer. High S1 concentration was required because the buffer differed from the standard S1 reaction buffer, resulting in a loss of activity. Four 5-μL portions of each reaction mixture were terminated at set time points (5, 15, 45, or 135 min) by dilution into 10 μL denaturing buffer (8 M urea, 80 mM EDTA, and 0.002% bromophenol blue) and immediate heat denaturation (20 min at 95°C). Samples were analyzed by denaturing (7 M urea) 9% PAGE imaged on a Typhoon Trio imager as above.

6.5.4 FRET data analysis

All image analysis and computations were performed using MATLAB R2012a (The MathWorks, Inc.). We wrote custom software to extract FRET efficiencies from gel images with high precision. Bands were selected manually from gel images. A 5 pixel × 5 pixel median filter was applied to each image to remove speckle. For each band, we plotted pixel-by-pixel A_{GR} and A_{GG} as a function of A_{RR}. Using the MATLAB "robustfit" function with default parameters we determined the slopes of these lines: I_G for green emission, and I_R for red emission. This regression procedure suppressed the influence of local background compared to simple integration of the intensities of each channel, resulting in an improved signal-to-noise ratio. FRET efficiencies were calculated using the slopes, corrected for experimentally measured dye crosstalk and relative dye brightness according to

$$E_{FRET} = \frac{I_R - X_{AR} - I_G X_{DR}}{I_R - X_{AR} - I_G X_{DR} + \rho I_G}, \tag{6.12}$$

where X_{AR} is the ratio of the emission of the acceptor (Alexa 647) in the red detection channel under green versus red excitation, X_{DR} is the ratio of the emission of the donor (Cy3B) into the red versus green detection channel, and ρ is the ratio of the emission of the acceptor dye into the red channel to that of the donor dye into the green channel. Emission of the acceptor dye in the green detection channel and excitation of the donor dye by the red laser were both determined experimentally to be negligible. Note that these parameters depend not only on the properties of the dyes themselves, but also on the instrument used to perform the spectroscopy. X_{AR} and X_{DR} were measured using singly labeled molecules, and ρ was inferred from the hairpin data themselves via a

142

Deming regression of I_R against I_G, the slope of which was taken to be $X_{DR} - \rho$. FRET efficiencies were further corrected for incomplete acceptor-dye labeling by dividing by the value measured in the absence of a complementary strand, which would be expected to display 100% FRET efficiency. This correction was applied for each hairpin type separately to account for variations in labeling or purification efficiency.

6.5.5 Simulations and fitting

Partition integrals were calculated numerically using the MATLAB "quad" function with default settings, on an Intel Core i7 notebook computer running 64-bit Windows 7. Partition terms were evaluated for each hairpin for each degree of base pairing in the stem and loop, and appropriate terms were summed for each target strand length [Equation (6.3)]. The parameters of the model were set to plausible values based on literature sources (Table 6:1). A range of FRET values were calculated using the range of R_0 values in Table 6:1, and the results for R_0 = 6.2 were fit to experimental data for each hairpin individually using a one-parameter least-squares regression, in which the offset was fixed such that the value E_{FRET} = 1 remained unchanged. This scaling was then applied to the range of FRET results and plotted as the shaded areas in Figure 6-3 B.

6.5.6 Sequences

All are written 5' to 3'

Loop sequences (30, 36, 40, 46, and 50 nt):

```
        TCGCCCACCGATAAGCTTGGTCATGCCCGT
       TGCCCGCCCACCGATAAGCTTGGTCATGCCCGCCGT
      TCCGCCCGCCCACCGATAAGCTTGGTCATGCCCGCCGCCT
     TCCGCCGCCCGCCCACCGATAAGCTTGGTCATGCCCGCCGCCGCCT
    TGCCCGCCGCCCGCCCACCGATAAGCTTGGTCATGCCCGCCGCCGCCCGT
```

The outermost thymine nucleotides were amine-modified and linked to Alexa647 (5′ side, red) or Cy3B (3′ side, green). Complementary strands did not include base-pairing partners for the dye-conjugated nucleotides. Site specific mismatches were placed at the center of the target strand, opposite the positions marked in blue.

Stem sequence:

```
GCCCGGCGGCTTATAAAATTTATTAATTATATATTTTATTTAATATAAT-Loop
```

Complementary sequences (20–48 nt):

```
CATGACCAAGCTTATCGGTG
GCATGACCAAGCTTATCGGTG
GCATGACCAAGCTTATCGGTGG
GGCATGACCAAGCTTATCGGTGG
…
CGGGCGGCGGCGGGCATGACCAAGCTTATCGGTGGGCGGGCGGCGGGC
```

Mismatched target strands contained single base substitutions at one of the nucleotides marked in blue (the T was replaced with A for the A-A mismatches, the A was replaced with T for the T-T mismatches, and the central nucleotides were replaced as appropriate to generate the other six mismatches).

References

[1]   Fields AP, Cohen AE (2010) Anti-Brownian traps for studies on single molecules. *Meth Enzymol* 475:149-174.

[2]   Fields AP, Cohen AE (2012) Optimal tracking of a Brownian particle. *Opt Express* 20:22585-22601.

[3]   Fields AP, Cohen AE (2011) Electrokinetic trapping at the one nanometer limit. *Proc Natl Acad Sci USA* 108:8937-8942.

[4]   Cohen AE, Fields AP (2011) The cat that caught the canary: what to do with single-molecule trapping. *ACS Nano* 5:5296-5299.

[5]   Einstein A (1905) On the movement of small particles suspended in stationary liquids required by the molecular-kinetic theory of heat. *Annalen Der Physik* 17:549-560.

[6]   Wang Q, Moerner WE (2011) An adaptive Anti-Brownian ELectrokinetic (ABEL) trap with real-time information on single-molecule diffusivity and mobility. *ACS Nano* 5:5792-5799.

[7]   Cohen AE, Moerner WE (2007) Internal mechanical response of a polymer in solution. *Phys Rev Lett* 98:116001.

[8]   Cohen AE, Moerner WE (2007) Principal-components analysis of shape fluctuations of single DNA molecules. *Proc Natl Acad Sci USA* 104:12622-12627.

[9]   Cang H, Wong CM, Xu CS, Rizvi AH, Yang H (2006) Confocal three dimensional tracking of a single nanoparticle with concurrent spectroscopic readouts. *Appl Phys Lett* 88:223901.

[10]   Ha T, *et al.* (1999) Ligand-induced conformational changes observed in single RNA molecules. *Proc Natl Acad Sci USA* 96:9077-9082.

[11]   Abbondanzieri EA, *et al.* (2008) Dynamic binding orientations direct activity of HIV reverse transcriptase. *Nature* 453:184-189.

[12]   Ha T, *et al.* (1999) Single-molecule fluorescence spectroscopy of enzyme conformational dynamics and cleavage mechanism. *Proc Natl Acad Sci USA* 96:893-898.

[13]   Lipman EA, Schuler B, Bakajin O, Eaton WA (2003) Single-molecule measurement of protein folding kinetics. *Science* 301:1233-1235.

[14]   Cai L, Friedman N, Xie XS (2006) Stochastic protein expression in individual cells at the single molecule level. *Nature* 440:358-362.

[15]   Kim SY, Gitai Z, Kinkhabwala A, Shapiro L, Moerner WE (2006) Single molecules of the bacterial actin MreB undergo directed treadmilling motion in *Caulobacter crescentus. Proc Natl Acad Sci USA* 103:10929-10934.

[16]   Ha T (2001) Single-molecule fluorescence methods for the study of nucleic acids. *Curr Opin Struct Biol* 11:287-292.

[17]   Dickson RM, Norris DJ, Moerner WE (1998) Simultaneous imaging of individual molecules aligned both parallel and perpendicular to the optic axis. *Phys Rev Lett* 81:5322-5325.

[18]   Lu HP, Xun L, Xie XS (1998) Single-molecule enzymatic dynamics. *Science* 282:1877-1882.

[19]   Boukobza E, Sonnenfeld A, Haran G (2001) Immobilization in surface-tethered lipid vesicles as a new tool for single biomolecule spectroscopy. *J Phys Chem B* 105:12165-12170.

[20]   Cisse I, Okumus B, Joo C, Ha T (2007) Fueling protein DNA interactions inside porous nanocontainers. *Proc Natl Acad Sci USA* 104:12646-12650.

[21]   Katsura S*, et al.* (2001) Indirect micromanipulation of single molecules in water-in-oil emulsion. *Electrophoresis* 22:289-293.

[22]   Shon MJ, Cohen AE (2012) Mass action at the single-molecule level. *J Am Chem Soc* 134:14618-14623.

[23]   Meseth U, Wohland T, Rigler R, Vogel H (1999) Resolution of fluorescence correlation measurements. *Biophys J* 76:1619-1631.

[24]   Chen Y, Müller JD, So PTC, Gratton E (1999) The photon counting histogram in fluorescence fluctuation spectroscopy. *Biophys J* 77:553-567.

[25]   Kim SY*, et al.* (2005) Probing the sequence of conformationally induced polarity changes in the molecular chaperonin GroEL with fluorescence spectroscopy. *J Phys Chem B* 109:24517-24525.

[26]   Bustamante C, Bryant Z, Smith SB (2003) Ten years of tension: single-molecule DNA mechanics. *Nature* 421:423-427.

[27]   Gosse C, Croquette V (2002) Magnetic tweezers: micromanipulation and force measurement at the molecular level. *Biophys J* 82:3314-3329.

[28] Voldman J, Braff RA, Toner M, Gray ML, Schmidt MA (2001) Holding forces of single-particle dielectrophoretic traps. *Biophys J* 80:531-541.

[29] Toussaint KC*, et al.* (2007) Plasmon resonance-based optical trapping of single and multiple Au nanoparticles. *Opt Express* 15:12017-12029.

[30] Arnold S, Hessel N (1985) Photoemission from single electrodynamically levitated microparticles. *Rev Sci Instrum* 56:2066-2069.

[31] Berg HC (1993) *Random walks in biology* (Princeton University Press, Princeton, New Jersey).

[32] Mills R (1973) Self-diffusion in normal and heavy water in the range 1–45°. *J Phys Chem* 77:685-688.

[33] Tyn MT, Gusek TW (1990) Prediction of diffusion coefficients of proteins. *Biotechnol Bioeng* 35:327-338.

[34] Brune D, Kim S (1993) Predicting protein diffusion coefficients. *Proc Natl Acad Sci USA* 90:3835-3839.

[35] Plenert ML, Shear JB (2003) Microsecond electrophoresis. *Proc Natl Acad Sci USA* 100:3853-3857.

[36] Cang H, Xu CS, Yang H (2008) Progress in single-molecule tracking spectroscopy. *Chem Phys Lett* 457:285-291.

[37] Juette MF, Bewersdorf J (2010) Three-dimensional tracking of single fluorescent particles with submillisecond temporal resolution. *Nano Lett* 10:4657-4663.

[38] Lu PJ, Sims PA, Oki H, Macarthur JB, Weitz DA (2007) Target-locking acquisition with real-time confocal (TARC) microscopy. *Opt Express* 15:8702-8712.

[39] Cohen AE, Moerner WE (2005) Method for trapping and manipulating nanoscale objects in solution. *Appl Phys Lett* 86:093109.

[40] Cohen AE, Moerner WE (2006) Suppressing Brownian motion of individual biomolecules in solution. *Proc Natl Acad Sci USA* 103:4362-4365.

[41] Han JJ, Kiss C, Bradbury AR, Werner JH (2012) Time-resolved, confocal single-molecule tracking of individual organic dyes and fluorescent proteins in three dimensions. *ACS Nano* 6:8922-8932.

[42] Xu CS, Cang H, Montiel D, Yang H (2007) Rapid and quantitative sizing of nanoparticles using three-dimensional single-particle tracking. *J Phys Chem C* 111:32-35.

[43]   Levi V, Ruan Q, Gratton E (2005) 3-D particle tracking in a two-photon microscope: application to the study of molecular dynamics in cells. *Biophys J* 88:2919-2928.

[44]   Berglund AJ, Mabuchi H (2005) Tracking-FCS: fluorescence correlation spectroscopy of individual particles. *Opt Express* 13:8069-8082.

[45]   McHale K, Berglund AJ, Mabuchi H (2007) Quantum dot photon statistics measured by three-dimensional particle tracking. *Nano Lett* 7:3535-3539.

[46]   Cohen AE, Moerner WE (2008) Controlling Brownian motion of single protein molecules and single fluorophores in aqueous buffer. *Opt Express* 16:6941-6956.

[47]   Davis L, *et al.* (2008) Maximum-likelihood position sensing and actively controlled electrokinetic transport for single-molecule trapping. *Proc SPIE* 6862:68620.

[48]   Armani M, Chaudhary S, Probst R, Walker S, Shapiro B (2005) Control of microfluidic systems: two examples, results, and challenges. *Int J Robust Nonlinear Control* 15:785.

[49]   Cohen AE, Moerner WE (2005) The anti-Brownian electrophoretic trap (ABEL trap): fabrication and software. *Proc SPIE* 5699:296.

[50]   Ropp C, *et al.* (2010) Manipulating quantum dots to nanometer precision by control of flow. *Nano Lett* 10:2525-2530.

[51]   Ropp C, *et al.* (2010) Positioning and immobilization of individual quantum dots with nanoscale precision. *Nano Lett* 10:4673-4679.

[52]   Ropp C, *et al.* (2013) Nanoscale imaging and spontaneous emission control with a single nano-positioned quantum dot. *Nature Commun* 4:1447.

[53]   Katayama Y, *et al.* (2009) Real-time nanomicroscopy via three-dimensional single-particle tracking. *Chemphyschem* 10:2458-2464.

[54]   Berg HC (1971) How to track bacteria. *Rev Sci Instrum* 42:868-871.

[55]   Cang H, Xu CS, Montiel D, Yang H (2007) Guiding a confocal microscope by single fluorescent nanoparticles. *Opt Lett* 32:2729-2731.

[56]   Lessard GA, Goodwin PM, Werner JH (2007) Three-dimensional tracking of individual quantum dots. *Appl Phys Lett* 91:224106.

[57]   Enderlein J (2000) Tracking of fluorescent molecules diffusing within membranes. *Appl Phys B* 71:773-777.

[58]   Valentine MT*, et al.* (2008) Precision steering of an optical trap by electro-optic deflection*. Opt Lett* 33:599-601.

[59]   Levi V, Ruan Q, Kis-Petikova K, Gratton E (2003) Scanning FCS, a novel method for three-dimensional particle tracking*. Biochem Soc Trans* 31:997-1000.

[60]   Berglund AJ, Mabuchi H (2004) Feedback controller design for tracking a single fluorescent molecule*. Appl Phys B* 78:653-659.

[61]   Berglund AJ, Mabuchi H (2006) Performance bounds on single-particle tracking by fluorescence modulation*. Appl Phys B* 83:127-133.

[62]   Berglund AJ, McHale K, Mabuchi H (2007) Feedback localization of freely diffusing fluorescent particles near the optical shot-noise limit*. Opt Lett* 32:145-147.

[63]   McHale K, Mabuchi H (2009) Precise Characterization of the Conformation Fluctuations of Freely Diffusing DNA: Beyond Rouse and Zimm*. J Am Chem Soc* 131:17901-17907.

[64]   McHale K, Mabuchi H (2010) Intramolecular fluorescence correlation spectroscopy in a feedback tracking microscope*. Biophys J* 99:313-322.

[65]   Jiang Y*, et al.* (2008) Hardware-based anti-Brownian electrokinetic trap (ABEL trap) for single molecules: control loop simulations and application to ATP binding stoichiometry in multi-subunit enzymes*. Proc SPIE* 7038:1-12.

[66]   Cohen AE (2005) Control of nanoparticles with arbitrary two-dimensional force fields*. Phys Rev Lett* 94:118102.

[67]   Cohen AE, Moerner WE (2005) An all-glass microfluidic cell for the ABEL trap: fabrication and modeling*. Proc SPIE* 5930:191-198.

[68]   Goldsmith RH, Moerner WE (2010) Watching conformational- and photodynamics of single fluorescent proteins in solution*. Nature Chem* 2:179-186.

[69]   Jiang Y*, et al.* (2011) Sensing cooperativity in ATP hydrolysis for single multisubunit enzymes in solution*. Proc Natl Acad Sci USA* 108:16962-16967.

[70]   Goldsmith RH*, et al.* (2011) Redox cycling and kinetic analysis of single molecules of solution-phase nitrite reductase*. Proc Natl Acad Sci USA* 108:17269-17274.

[71]   Bockenhauer S, Fürstenberg A, Yao XJ, Kobilka BK, Moerner W (2011) Conformational dynamics of single G protein-coupled receptors in solution*. J Phys Chem B* 115:13328-13338.

[72]   Chaudhary S, Shapiro B (2006) Arbitrary steering of multiple particles independently in an electro-osmotically driven microfluidic system. *IEEE Trans Control Syst Technol* 14:669-680.

[73]   Li X, Hofmeister W, Shen G, Davis L, Daniel C (2008) in *Medical Device Materials IV (Proceedings of the Materials and Processes for Medical Devices Conference 2007),* ed Gilbert J (ASM International, Materials Park, Ohio), pp 145-150.

[74]   Hamilton JD (1994) *Time Series Analysis* (Princeton University Press, Princeton, New Jersey).

[75]   Dertinger T*, et al.* (2007) Two-focus fluorescence correlation spectroscopy: A new tool for accurate and absolute diffusion measurements. *ChemPhysChem* 8:433-443.

[76]   Wang HY, Foote RS, Jacobson SC, Schneibel JH, Ramsey JM (1997) Low temperature bonding for microfabrication of chemical analysis devices. *Sens Actuators B* 45:199-207.

[77]   Jun Y, Bechhoefer J (2011) Experimental study of memory erasure in a double-well potential. *Bull Amer Phys Soc* 56:D13.00010.

[78]   Jun Y, Bechhoefer J (2012) Virtual potentials for feedback traps. *Phys Rev E Stat Nonlin Soft Matter Phys* 86:061106.

[79]   Armani M, Chaudhary S, Probst R, Shapiro B (2006) Using feedback control of microflows to independently steer multiple particles. *J Microelectromech Sys* 15:945-956.

[80]   Börsch M (2011) Single-molecule fluorescence resonance energy transfer techniques on rotary ATP synthases. *Biol Chem* 392:135-142.

[81]   Börsch M (2013) Microscopy of single FoF1-ATP synthases—the unraveling of motors, gears, and controls. *IUBMB Life* 65:227-237.

[82]   Sielaff H, Börsch M (2013) Twisting and subunit rotation in single F_OF_1-ATP synthase. *Philos Trans R Soc Lond B Biol Sci* 368:20120024.

[83]   Levi V, Gratton E (2008) Chromatin dynamics during interphase explored by single-particle tracking. *Chromosome Res* 16:439-449.

[84]   Cardarelli F, Lanzano L, Gratton E (2012) Capturing directed molecular motion in the nuclear pore complex of live cells. *Proc Natl Acad Sci USA* 109:9863-9868.

[85]   Adu-Gyamfi E, Digman MA, Gratton E, Stahelin RV (2012) Single-particle tracking demonstrates that actin coordinates the movement of the Ebola virus matrix protein. *Biophys J* 103:L41-L43.

[86]   Wells NP*, et al.* (2010) Time-resolved three-dimensional molecular tracking in live cells. *Nano Lett* 10:4732-4737.

[87]   Saxton MJ, Jacobson K (1997) Single-particle tracking: applications to membrane dynamics. *Annu Rev Biophys Biomol Struct* 26:373-399.

[88]   Douglass AD, Vale RD (2005) Single-molecule microscopy reveals plasma membrane microdomains created by protein-protein networks that exclude or trap signaling molecules in T cells. *Cell* 121:937-950.

[89]   Chung I*, et al.* (2010) Spatial control of EGF receptor activation by reversible dimerization on living cells. *Nature* 464:783-787.

[90]   Yildiz A*, et al.* (2003) Myosin V walks hand-over-hand: single fluorophore imaging with 1.5-nm localization. *Science* 300:2061-2065.

[91]   Thompson MA, Casolari JM, Badieirostami M, Brown PO, Moerner WE (2010) Three-dimensional tracking of single mRNA particles in *Saccharomyces cerevisiae* using a double-helix point spread function. *Proc Natl Acad Sci USA* 107:17864-17871.

[92]   Cang H, Montiel D, Xu CS, Yang H (2008) Observation of spectral anisotropy of gold nanoparticles. *J Chem Phys* 129:044503.

[93]   Jazwinski AH (1970) *Stochastic processes and filtering theory* (Academic Press, New York).

[94]   McHale K, Berglund AJ, Mabuchi H (2004) Bayesian estimation for species identification in single-molecule fluorescence microscopy. *Biophys J* 86:3409-3422.

[95]   Berglund AJ, McHale K, Mabuchi H (2007) Fluctuations in closed-loop fluorescent particle tracking. *Opt Express* 15:7752-7773.

[96]   Mortensen KI, Churchman LS, Spudich JA, Flyvbjerg H (2010) Optimized localization analysis for single-molecule tracking and super-resolution microscopy. *Nat Methods* 7:377-381.

[97]   Zhang B, Zerubia J, Olivo-Marin JC (2007) Gaussian approximations of fluorescence microscope point-spread function models. *Appl Opt* 46:1819-1829.

[98] Arulampalam MS, Maskell S, Gordon N, Clapp T (2002) A tutorial on particle filters for online nonlinear/non-Gaussian Bayesian tracking. *IEEE Trans Signal Process* 50:174-188.

[99] Minka TP (2001) *A family of algorithms for approximate Bayesian inference.* Ph.D. thesis (Massachusetts Institute of Technology, Cambridge, MA).

[100] Maybeck PS (1979) *Stochastic models, estimation and control* (Academic press, New York, NY).

[101] Sorenson HW, Alspach DL (1971) Recursive Bayesian estimation using Gaussian sums. *Automatica* 7:465-479.

[102] Kalman RE (1960) A new approach to linear filtering and prediction problems. *J Basic Eng Trans ASME* 82:35-45.

[103] Welch G & Bishop G (2006) An introduction to the Kalman filter. *Technical Report* (University of North Carolina, Chapel Hill, NC), TR 95-041.

[104] Brinkmeier M, Dorre K, Stephan J, Eigen M (1999) Two-beam cross-correlation: a method to characterize transport phenomena in micrometer-sized structures. *Anal Chem* 71:609-616.

[105] Kapusta P (2010) Absolute diffusion coefficients: compilation of reference data for FCS calibration. *Application Note* (PicoQuant GmbH, Berlin), http://www.picoquant.com/technotes/appnote_diffusion_coefficients.pdf.

[106] Hansen PM, Bhatia VK, Harrit N, Oddershede L (2005) Expanding the optical trapping range of gold nanoparticles. *Nano Lett* 5:1937-1942.

[107] Kubanek A, *et al.* (2009) Photon-by-photon feedback control of a single-atom trajectory. *Nature* 462:898-901.

[108] Greenleaf WJ, Woodside MT, Abbondanzieri EA, Block SM (2005) Passive all-optical force clamp for high-resolution laser trapping. *Phys Rev Lett* 95:208102.

[109] Lusetti SL, Cox MM (2002) The bacterial RecA protein and the recombinational DNA repair of stalled replication forks. *Annu Rev Biochem* 71:71-100.

[110] Chen Z, Yang H, Pavletich NP (2008) Mechanism of homologous recombination from the RecA–ssDNA/dsDNA structures. *Nature* 453:489-494.

[111] Joo C, *et al.* (2006) Real-time observation of RecA filament dynamics with single monomer resolution. *Cell* 126:515-527.

[112] Galletto R, Amitani I, Baskin RJ, Kowalczykowski SC (2006) Direct observation of individual RecA filaments assembling on single DNA molecules. *Nature* 443:875-878.

[113] Hegner M, Smith SB, Bustamante C (1999) Polymerization and mechanical properties of single RecA–DNA filaments. *Proc Natl Acad Sci USA* 96:10109-10114.

[114] King JK (2009) *Microfluidic device for the electrokinetic manipulation of single molecules.* M.S. thesis (University of Tennessee, Knoxville, TN).

[115] Wang Q, Moerner WE (2010) Optimal strategy for trapping single fluorescent molecules in solution using the ABEL trap. *Appl Phys B* 99:23-30.

[116] ABEL trap code repository, https://www2.lsdiv.harvard.edu/labs/cohen/Research/TrapSingMol/Code/Code.htm.

[117] Leung W, Cheung C & Yue S (2007) Modified carbocyanine dyes and their conjugates. *US Patent* 7,671,214.

[118] Smith SB, Cui Y, Bustamante C (1996) Overstretching B-DNA: the elastic response of individual double-stranded and single-stranded DNA molecules. *Science* 271:795-799.

[119] Doi M & Edwards SF (1988) *The theory of polymer dynamics* (Oxford University Press, New York).

[120] Brenner SL*, et al.* (1987) RecA protein-promoted ATP hydrolysis occurs throughout RecA nucleoprotein filaments. *J Biol Chem* 262:4011-4016.

[121] Silver MS, Fersht AR (1982) Direct observation of complexes formed between recA protein and a fluorescent single-stranded deoxyribonucleic acid derivative. *Biochemistry* 21:6066-6072.

[122] Heuser J, Griffith J (1989) Visualization of RecA protein and its complexes with DNA by quick-freeze/deep-etch electron microscopy. *J Mol Biol* 210:473-484.

[123] McEntee K, Weinstock GM, Lehman IR (1981) Binding of the recA protein of Escherichia coli to single-and double-stranded DNA. *J Biol Chem* 256:8835-8844.

[124] Henry DC (1931) The cataphoresis of suspended particles. Part I. The equation of cataphoresis. *Proc R Soc Lond A Math Phys Sci* 133:106-129.

[125]   Stellwagen E, Stellwagen NC (2002) Determining the electrophoretic mobility and translational diffusion coefficients of DNA molecules in free solution. *Electrophoresis* 23:2794-2803.

[126]   Foulds GJ, Etzkorn FA (1998) A capillary electrophoresis mobility shift assay for protein-DNA binding affinities free in solution. *Nucleic Acids Res* 26:4304-4305.

[127]   Menetski JP, Kowalczykowski SC (1985) Interaction of recA protein with single-stranded DNA: Quantitative aspects of binding affinity modulation by nucleotide cofactors. *J Mol Biol* 181:281-295.

[128]   Magde D, Elson E, Webb WW (1972) Thermodynamic fluctuations in a reacting system–measurement by fluorescence correlation spectroscopy. *Phys Rev Lett* 29:705-708.

[129]   Shera EB, Seitzinger NK, Davis LM, Keller RA, Soper SA (1990) Detection of single fluorescent molecules. *Chem Phys Lett* 174:553-557.

[130]   Deniz AA*, et al.* (1999) Single-pair fluorescence resonance energy transfer on freely diffusing molecules: observation of Förster distance dependence and subpopulations. *Proc Natl Acad Sci USA* 96:3670-3675.

[131]   Brocchieri L, Karlin S (2005) Protein length in eukaryotic and prokaryotic proteomes. *Nucleic Acids Res* 33:3390-3400.

[132]   Aitken CE, Marshall RA, Puglisi JD (2008) An oxygen scavenging system for improvement of dye stability in single-molecule fluorescence experiments. *Biophys J* 94:1826-1835.

[133]   Vogelsang J*, et al.* (2008) A reducing and oxidizing system minimizes photobleaching and blinking of fluorescent dyes. *Angew Chem Int Ed* 47:5465-5469.

[134]   Tirado MM, de La Torre JG (1979) Translational friction coefficients of rigid, symmetric top macromolecules. Application to circular cylinders. *J Chem Phys* 71:2581-2587.

[135]   Lakowicz JR (2006) *Principles of fluorescence spectroscopy* (Springer, New York).

[136]   Pascher T, Chesick JP, Winkler JR, Gray HB (1996) Protein folding triggered by electron transfer. *Science* 271:1558-1560.

[137]   Gruebele M, Sabelko J, Ballew R, Ervin J (1998) Laser temperature jump induced protein refolding. *Acc Chem Res* 31:699-707.

[138] Lee Jr CT, Smith KA, Hatton TA (2005) Photocontrol of protein folding: the interaction of photosensitive surfactants with bovine serum albumin. *Biochemistry* 44:524-536.

[139] Junker JP, Ziegler F, Rief M (2009) Ligand-dependent equilibrium fluctuations of single calmodulin molecules. *Science* 323:633-637.

[140] Michalet X, Weiss S, Jäger M (2006) Single-molecule fluorescence studies of protein folding and conformational dynamics. *Chem Rev* 106:1785-1813.

[141] Schuler B, Eaton WA (2008) Protein folding studied by single-molecule FRET. *Curr Opin Struct Biol* 18:16-26.

[142] Olive DM (2004) Quantitative methods for the analysis of protein phosphorylation in drug development. *Expert Rev Proteomics* 1:327-341.

[143] Cohen CB, Chin-Dixon E, Jeong S, Nikiforov TT (1999) A microchip-based enzyme assay for protein kinase A. *Anal Biochem* 273:89-97.

[144] Maxwell JC (1872) *Theory of heat* (Longmans Green and Co., New York).

[145] Cohen AE, Fields AP, Hou JH, Leslie SR, Shon MJ (2009) In honor of W.E. Moerner: confining molecules for single-molecule spectroscopy. *Isr J Chem* 49:275-282.

[146] Leslie SR, Fields AP, Cohen AE (2010) Convex lens-induced confinement for imaging single molecules. *Anal Chem* 82:6224-6229.

[147] Kinoshita M, *et al.* (2007) Development of a technique for the investigation of folding dynamics of single proteins for extended time periods. *Proc Natl Acad Sci USA* 104:10453-10458.

[148] Okumus B, Arslan S, Fengler SM, Myong S, Ha T (2009) Single molecule nanocontainers made porous using a bacterial toxin. *J Am Chem Soc* 131:14844-14849.

[149] Levene MJ, *et al.* (2003) Zero-mode waveguides for single-molecule analysis at high concentrations. *Science* 299:682-686.

[150] Chiu DT, Lorenz RM, Jeffries GDM (2009) Droplets for ultrasmall-volume analysis. *Anal Chem* 81:5111-5118.

[151] Kratky O, Porod G (1949) Röntgenuntersuchung gelöster fadenmoleküle. *Recueil Des Travaux Chimiques Des Pays-Bas* 68:1106-1123.

[152]   Hagerman PJ (1988) Flexibility of DNA. *Annu Rev Biophys Biophys Chem* 17:265-286.

[153]   Lu Y, Weers B, Stellwagen NC (2002) DNA persistence length revisited. *Biopolymers* 61:261-275.

[154]   Crick FH, Klug A (1975) Kinky helix. *Nature* 255:530-533.

[155]   Yan J, Marko JF (2004) Localized single-stranded bubble mechanism for cyclization of short double helix DNA. *Phys Rev Lett* 93:108108.

[156]   McGhee J, Felsenfeld G (1980) Nucleosome structure. *Annu Rev Biochem* 49:1115-1156.

[157]   Richmond TJ, Davey CA (2003) The structure of DNA in the nucleosome core. *Nature* 423:145-150.

[158]   Sekinger EA, Moqtaderi Z, Struhl K (2005) Intrinsic histone-DNA interactions and low nucleosome density are important for preferential accessibility of promoter regions in yeast. *Mol Cell* 18:735-748.

[159]   Shrader TE, Crothers DM (1990) Effects of DNA sequence and histone-histone interactions on nucleosome placement. *J Mol Biol* 216:69-84.

[160]   Morozov AV, *et al.* (2009) Using DNA mechanics to predict in vitro nucleosome positions and formation energies. *Nucleic Acids Res* 37:4707-4722.

[161]   Pérez A, *et al.* (2012) Impact of methylation on the physical properties of DNA. *Biophys J* 102:2140-2148.

[162]   Dickerson RE (1998) DNA bending: the prevalence of kinkiness and the virtues of normality. *Nucleic Acids Res* 26:1906-1926.

[163]   Schultz SC, Shields GC, Steitz TA (1991) Crystal structure of a CAP-DNA complex: the DNA is bent by 90 degrees. *Science* 253:1001-1007.

[164]   Li T, Stark MR, Johnson AD, Wolberger C (1995) Crystal structure of the MATa1/MATα2 homeodomain heterodimer bound to DNA. *Science* 270:262-269.

[165]   Winkler FK, *et al.* (1993) The crystal structure of EcoRV endonuclease and of its complexes with cognate and non-cognate DNA fragments. *EMBO J* 12:1781-1795.

[166]   Vilar JM, Saiz L (2005) DNA looping in gene regulation: from the assembly of macromolecular complexes to the control of transcriptional noise. *Curr Opin Genet Dev* 15:136-144.

[167] Muller J, Oehler S, Muller-Hill B (1996) Repression of lac promoter as a function of distance, phase and quality of an auxiliary lac operator. *J Mol Biol* 257:21-29.

[168] Paull TT, Haykinson MJ, Johnson RC (1993) The nonspecific DNA-binding and-bending proteins HMG1 and HMG2 promote the assembly of complex nucleoprotein structures. *Genes Dev* 7:1521-1534.

[169] Schleif R (1992) DNA looping. *Annu Rev Biochem* 61:199-223.

[170] Seeman NC (2010) Nanomaterials based on DNA. *Annu Rev Biochem* 79:65-87.

[171] Ke Y, Ong LL, Shih WM, Yin P (2012) Three-dimensional structures self-assembled from DNA bricks. *Science* 338:1177-1183.

[172] Yurke B, Turberfield AJ, Mills AP, Simmel FC, Neumann JL (2000) A DNA-fuelled molecular machine made of DNA. *Nature* 406:605-608.

[173] Hays JB, Magar ME, Zimm BH (1969) Persistence length of DNA. *Biopolymers* 8:531-536.

[174] Hagerman PJ (1981) Investigation of the flexibility of DNA using transient electric birefringence. *Biopolymers* 20:1503-1535.

[175] Eisenberg H (1987) DNA flexing, folding, and function. *Acc Chem Res* 20:276-282.

[176] Shore D, Langowski J, Baldwin RL (1981) DNA flexibility studied by covalent closure of short fragments into circles. *Proc Natl Acad Sci USA* 78:4833-4837.

[177] Peters JP, Maher LJ (2010) DNA curvature and flexibility *in vitro* and *in vivo*. *Q Rev Biophys* 43:23-63.

[178] Wiggins PA, Phillips R, Nelson PC (2005) Exact theory of kinkable elastic polymers. *Phys Rev E Stat Nonlin Soft Matter Phys* 71:021909.

[179] Cloutier TE, Widom J (2004) Spontaneous sharp bending of double-stranded DNA. *Mol Cell* 14:355-362.

[180] Cloutier TE, Widom J (2005) DNA twisting flexibility and the formation of sharply looped protein-DNA complexes. *Proc Natl Acad Sci USA* 102:3645-3650.

[181] Du Q, Smith C, Shiffeldrim N, Vologodskaia M, Vologodskii A (2005) Cyclization of short DNA fragments and bending fluctuations of the double helix. *Proc Natl Acad Sci USA* 102:5397-5402.

[182] Forties RA, Bundschuh R, Poirier MG (2009) The flexibility of locally melted DNA. *Nucleic Acids Res* 37:4580-4586.

[183]   Vafabakhsh R, Ha T (2012) Extreme bendability of DNA less than 100 base pairs long revealed by single-molecule cyclization. *Science* 337:1097-1101.

[184]   Bustamante C, Smith SB, Liphardt J, Smith D (2000) Single-molecule studies of DNA mechanics. *Curr Opin Struct Biol* 10:279-285.

[185]   Amzallag A*, et al.* (2006) 3D reconstruction and comparison of shapes of DNA minicircles observed by cryo-electron microscopy. *Nucleic Acids Res* 34:e125-e125.

[186]   Demurtas D*, et al.* (2009) Bending modes of DNA directly addressed by cryo-electron microscopy of DNA minicircles. *Nucleic Acids Res* 37:2882-2893.

[187]   Frontali C*, et al.* (1979) An absolute method for the determination of the persistence length of native DNA from electron micrographs. *Biopolymers* 18:1353-1373.

[188]   Rivetti C, Guthold M, Bustamante C (1996) Scanning force microscopy of DNA deposited onto mica: equilibration *versus* kinetic trapping studied by statistical polymer chain analysis. *J Mol Biol* 264:919-932.

[189]   Rivetti C, Walker C, Bustamante C (1998) Polymer chain statistics and conformational analysis of DNA molecules with bends or sections of different flexibility. *J Mol Biol* 280:41-59.

[190]   Scipioni A, Anselmi C, Zuccheri G, Samori B, De Santis P (2002) Sequence-dependent DNA curvature and flexibility from scanning force microscopy images. *Biophys J* 83:2408-2418.

[191]   Wiggins PA*, et al.* (2006) High flexibility of DNA on short length scales probed by atomic force microscopy. *Nat Nanotechnol* 1:137-141.

[192]   Harrington RE (1993) Studies of DNA bending and flexibility using gel electrophoresis. *Electrophoresis* 14:732-746.

[193]   Kahn JD, Yun E, Crothers DM (1994) Detection of localized DNA flexibility. *Nature* 368:163-166.

[194]   Okonogi T, Reese A, Alley S, Hopkins P, Robinson B (1999) Flexibility of duplex DNA on the submicrosecond timescale. *Biophys J* 77:3256-3276.

[195]   Parkhurst LJ, Parkhurst KM, Powell R, Wu J, Williams S (2002) Time-resolved fluorescence resonance energy transfer studies of DNA bending in double-stranded oligonucleotides and in DNA–protein complexes. *Biopolymers* 61:180-200.

[196] Yuan C, Rhoades E, Lou XW, Archer LA (2006) Spontaneous sharp bending of DNA: role of melting bubbles. *Nucleic Acids Res* 34:4554-4560.

[197] Yuan C, Chen H, Lou XW, Archer LA (2008) DNA bending stiffness on small length scales. *Phys Rev Lett* 100:18102.

[198] Mathew-Fenn RS, Das R, Harbury PAB (2008) Remeasuring the double helix. *Science* 322:446-449.

[199] Mastroianni AJ, Sivak DA, Geissler PL, Alivisatos AP (2009) Probing the conformational distributions of subpersistence length DNA. *Biophys J* 97:1408-1417.

[200] Shroff H*, et al.* (2008) Optical measurement of mechanical forces inside short DNA loops. *Biophys J* 94:2179-2186.

[201] Qu H, Wang Y, Tseng CY, Zocchi G (2011) Critical torque for kink formation in double-stranded DNA. *Phys Rev X* 1:021008.

[202] Qu H, Tseng C, Wang Y, Levine AJ, Zocchi G (2010) The elastic energy of sharply bent nicked DNA. *Europhys Lett* 90:18003.

[203] Qu H, Zocchi G (2011) The complete bending energy function for nicked DNA. *Europhys Lett* 94:18003.

[204] Iyer RR, Pluciennik A, Burdett V, Modrich PL (2006) DNA mismatch repair: functions and mechanisms. *Chem Rev* 106:302-323.

[205] Hagerman PJ (1990) Sequence-directed curvature of DNA. *Annu Rev Biochem* 59:755-781.

[206] Geggier S, Vologodskii A (2010) Sequence dependence of DNA bending rigidity. *Proc Natl Acad Sci USA* 107:15421-15426.

[207] Zuker M (2003) Mfold web server for nucleic acid folding and hybridization prediction. *Nucleic Acids Res* 31:3406-3415.

[208] Macke TJ, Case DA (1998) in *Molecular Modeling of Nucleic Acids,* eds Leontes NB, SantaLucia J, Jr (American Chemical Society, Washington, DC), pp 379-393.

[209] DeLano WL (2002) *The PyMOL molecular graphics system* (DeLano Scientific, San Carlos, CA).

[210] Woodside MT*, et al.* (2006) Nanomechanical measurements of the sequence-dependent folding landscapes of single nucleic acid hairpins. *Proc Natl Acad Sci USA* 103:6190-6195.

[211] Landau LD & Lifshitz EM (1986) *Theory of Elasticity* (Elsevier, New York).

[212] Huguet JM*, et al.* (2010) Single-molecule derivation of salt dependent base-pair free energies in DNA*. Proc Natl Acad Sci USA* 107:15431-15436.

[213] Wang MC, Guth E (1952) Statistical theory of networks of non-gaussian flexible chains*. J Chem Phys* 20:1144-1157.

[214] Emanuel M, Mohrbach H, Sayar M, Schiessel H, Kulic IM (2007) Buckling of stiff polymers: influence of thermal fluctuations*. Phys Rev E Stat Nonlin Soft Matter Phys* 76:061907.

[215] Uphoff S*, et al.* (2010) Monitoring multiple distances within a single molecule using switchable FRET*. Nat Methods* 7:831-836.

[216] Wenner JR, Williams MC, Rouzina I, Bloomfield VA (2002) Salt dependence of the elasticity and overstretching transition of single DNA molecules. *Biophys J* 82:3160-3169.

[217] Narayana N, Weiss MA (2009) Crystallographic analysis of a sex-specific enhancer element: sequence-dependent DNA structure, hydration, and dynamics*. J Mol Biol* 385:469-490.

[218] Sivak DA, Geissler PL (2012) Consequences of local inter-strand dehybridization for large-amplitude bending fluctuations of double-stranded DNA*. J Chem Phys* 136:045102.

[219] Amirikyan B, Vologodskii A, Lyubchenko YL (1981) Determination of DNA cooperativity factor. *Nucleic Acids Res* 9:5469-5482.

[220] Blake R, Delcourt SG (1998) Thermal stability of DNA*. Nucleic Acids Res* 26:3323-3332.

[221] Fisher ME (1966) Effect of excluded volume on phase transitions in biopolymers. *J Chem Phys* 45:1469-1473.

[222] Isaacs RJ, Spielmann HP (2004) A model for initial DNA lesion recognition by NER and MMR based on local conformational flexibility*. DNA Repair* 3:455-464.

[223] Wang H*, et al.* (2003) DNA bending and unbending by MutS govern mismatch recognition and specificity*. Proc Natl Acad Sci USA* 100:14822-14827.

[224] Solaro PC, Birkenkamp K, Pfeiffer P, Kemper B (1993) Endonuclease VII of phage T4 triggers mismatch correction *in vitro. J Mol Biol* 230:868-877.

[225] Ganguly A, Rock MJ, Prockop DJ (1993) Conformation-sensitive gel electrophoresis for rapid detection of single-base differences in double-stranded PCR products and DNA fragments: evidence for solvent-induced bends in DNA heteroduplexes. *Proc Natl Acad Sci USA* 90:10325-10329.

[226] SantaLucia J, Jr, Hicks D (2004) The thermodynamics of DNA structural motifs. *Annu Rev Biophys Biomol Struct* 33:415-440.

[227] Beard P, Morrow JF, Berg P (1973) Cleavage of circular, superhelical simian virus 40 DNA to a linear duplex by S1 nuclease. *J Virol* 12:1303-1313.

[228] Du Q, Kotlyar A, Vologodskii A (2008) Kinking the double helix by bending deformation. *Nucleic Acids Res* 36:1120-1128.

[229] Fenley MO, Manning GS, Marky NL, Olson WK (1998) Excess counterion binding and ionic stability of kinked and branched DNA. *Biophys Chem* 74:135-152.

[230] Koo HS, Wu HM, Crothers DM (1986) DNA bending at adenine-thymine tracts. *Nature* 320:501-506.

[231] Nathan D, Crothers DM (2002) Bending and flexibility of methylated and unmethylated *Eco*RI DNA. *J Mol Biol* 316:7-17.

[232] Kimura T, Asai T, Imai M, Takanami M (1989) Methylation strongly enhances DNA bending in the replication origin region of the *Escherichia coli* chromosome. *Mol Gen Genet* 219:69-74.

[233] Husain I, Griffith J, Sancar A (1988) Thymine dimers bend DNA. *Proc Natl Acad Sci USA* 85:2558-2562.

[234] Jamieson ER, Lippard SJ (1999) Structure, recognition, and processing of cisplatin-DNA adducts. *Chem Rev* 99:2467-2498.

[235] Reinert K (1983) Anthracycline-binding induced DNA stiffening, bending and elongation; stereochemical implications from viscometric investigations. *Nucleic Acids Res* 11:3411-3430.

[236] Kunkel TA, Erie DA (2005) DNA mismatch repair. *Annu Rev Biochem* 74:681-710.

[237] Privalov PL, Dragan AI, Crane-Robinson C (2009) The cost of DNA bending. *Trends Biochem Sci* 34:464-470.

[238] Crawford R, Kelly DJ, Kapanidis AN (2012) A protein biosensor that relies on bending of single DNA molecules. *ChemPhysChem* 13:918-922.

[239]   Gu H, Yang W, Seeman NC (2010) DNA scissors device used to measure MutS binding to DNA mis-pairs. *J Am Chem Soc* 132:4352-4357.

[240]   Harvey BJ, Perez C, Levitus M (2009) DNA sequence-dependent enhancement of Cy3 fluorescence. *Photochem Photobiol Sci* 8:1105-1110.

[241]   Han W, Dlakic M, Zhu YJ, Lindsay S, Harrington RE (1997) Strained DNA is kinked by low concentrations of Zn^{2+}. *Proc Natl Acad Sci USA* 94:10565-10570.

[242]   Vogt VM (1973) Purification and further properties of single-strand-specific nuclease from Aspergillus oryzae. *European Journal of Biochemistry* 33:192-200.